



**Utrecht
University**

**Initial erosion-deposition patterns in a
sheltered coastal environment: the role of
wind, waves, tides and graded sediment**

Roel Hoegen

July 4, 2022





**Utrecht
University**

Initial erosion-deposition patterns in a sheltered coastal environment: the role of wind, waves, tides and graded sediment

Roel Hoegen

July 4, 2022

Master Thesis for a combined degree in

Marine Sciences
Department of Physical
Geography
Faculty of Geosciences

Climate Physics
Institute for Marine and
Atmospheric research Utrecht
Graduate School of Natural
Science

First supervisor: Dr. Timothy Price

Second supervisor: Prof. dr. Huib de Swart

Expert: Dr. Maarten van der Vegt

Abstract

Nature-based sandy coastal protection measures are becoming increasingly more important as a sustainable alternative for hard engineering protection works (e.g. dikes, sea walls and breakwaters). Currently, most sandy coastal interventions are sited at open-ocean coastal systems and consist of a uniform sediment mixture (e.g. 'Sand engine' at the Holland coast). However, there is also a need for sustainable coastal protection measures in more sheltered coastal environments such as estuaries, deltas and bay-side beaches. In addition, natural coastal systems often consist of a wide range of sediment sizes which can substantially alter the morphodynamic processes. Therefore, it is essential to understand the hydrodynamic and morphodynamic processes to predict the evolution of sheltered coastal interventions with non-uniform sediments.

This study applies the widely used morphodynamic Delft3D model to study the sediment transport dynamics of such a system. The 'Prins Hendrikzanddijk' (PHZD), situated on the bay side of the Texel barrier island in the Dutch Wadden Sea, is used as a prototype system for a sheltered coastal intervention with non-uniform sediments. A Delft3D model is set up for the PHZD and the hydrodynamics are extensively calibrated with wave height and velocity data from a 6-week field campaign. The design of the model experiments is twofold: 1) the environmental boundary conditions are systematically varied to identify the role of different drivers (waves, tides, winds) on sediment transport, 2) the number of sediment sizes and initial bed composition is varied to determine the role of graded sediments and the bed composition on sediment transport. In order to model the bed composition changes, a multi-layer bed stratigraphy module is applied.

The results show that the sediment transport is a function of the wind velocity, wind direction and the geometry of the basin. During moderate energetic conditions, the orbital wave motion dominates the bed-shear stress. However, for more extreme storm conditions, the wind- and wave-driven currents become increasingly more important. With increasing number of sediment fractions, the total sediment transport converges towards a larger suspended transport and a smaller bed-load transport compared to a single fraction. Furthermore, the process of preferential transport, hiding and exposure effect and bed armoring are modelled by the multi-layer bed stratigraphy. Nevertheless, the hydrodynamic conditions are of greater importance for the bed evolution than the bed composition as there is little difference in bed level changes for an initial fine or a coarse bed composition. In addition, it is shown that the initial vertical bed composition is crucial for bed composition changes. However, the multi-layer bed stratigraphy model treats the sediment transport as diffusive fluxes while the observations show deposition of discrete layers. Therefore, the model is not able to reproduce the observed vertical sorting.

Contents

1. Introduction	1
1.1. Research motivation	1
1.2. Objectives	5
1.3. Methodology	5
2. Theoretical background	6
2.1. Sediment properties	6
2.2. Initiation of motion	7
2.2.1. Forces on a resting particle	7
2.2.2. Shields parameter	7
2.2.3. Hiding and exposure	10
2.2.4. Bed-shear stress	11
2.3. Modes of sediment transport	13
2.4. Sediment transport mechanisms	16
2.4.1. Tides	16
2.4.2. Waves	18
2.4.3. Wind	21
3. Materials and methods	23
3.1. Observations	23
3.1.1. SEDMEX field campaign	23
3.1.2. Wind forcing and hydrodynamic conditions	23
3.1.3. Sediment size fractions	25
3.1.4. Bed composition change and morphological change	25
3.2. The Delft3D model set-up	27
3.3. Model calibration	31
3.3.1. Flow calibration	31
3.3.2. Wave calibration method	33
3.4. Experimental design	34
4. Model results	37
4.1. Drivers	38
4.1.1. The relative importance of wind, waves and tides on uniform sediment transport	38

4.1.2. Sediment transport under varying wind velocity and direction	43
4.2. Graded sediment	46
4.2.1. The effect of graded sediment on sediment transport	46
4.2.2. Importance of initial bed composition on initial erosion/deposition patterns	49
4.2.3. Sensitivity analysis	55
5. Discussion	57
5.1. The role of wind, waves and tides	57
5.1.1. PHZD	57
5.1.2. Implications for sediment transport in sheltered coastal systems	59
5.2. Graded sediments and bed composition	60
5.2.1. Graded sediment	60
5.2.2. Bed composition	61
5.3. Limitations and future recommendations	63
6. Conclusions	65
Acknowledgements	67
A. Supplementary figure	69
A.1. Drivers	70
B. Background information PHZD	82
B.0.1. Marsdiep basin	82
B.0.2. Schanserwaard inter-tidal flat	83
B.0.3. Prins Hendrikzandddijk	84
C. Calibration details	85
C.1. Calibration details	85
C.2. Model calibration and sensitivity analysis	85
C.2.1. Flow calibration results	85
C.2.2. Wave calibration results	87
References	90

1. Introduction

1.1. Research motivation

The majority of coastal ecosystems and settlements are threatened by erosion and flooding due to sea level rise (Cooley et al., 2022). In addition, hard engineering protection works (e.g. dikes, sea walls and breakwaters) are becoming economically and ecologically unsustainable under accelerating sea level rise (Morris et al., 2018). Therefore, sustainable nature-based solutions as alternative coastal protection measures are becoming increasingly more important. These nature-based solutions use the ecosystem's own flood defence mechanism (e.g. wave dampening by mangroves or self-repair of sandy coasts) as starting point and aim to restore or enhance these functions (Gittman et al., 2014). At sandy coastal environments, these nature-based solutions are most often in the form of a sand nourishment or dune. Such a sandy coastal protection measure either seeks to slowly transport its sand to the surrounding coasts or to strengthen the coast locally in a natural manner. As open, sandy coastal environments make up 40% of the world's coast and are often densely populated (Bird, 1996), it is of importance to understand the sediment transport dynamics at such coastal protection measures. The term nourishment will be used as encompassing term for sandy coastal protection measures.

In order to understand and predict the behaviour of sandy coastal interventions, it is necessary to understand the interaction between hydrodynamics, sediment transport and morphodynamics. Currently, most nourishments are situated at ocean-exposed coasts, e.g. 'sand engine' south of the Hague at the Holland coast (Stive et al., 2013), as these are most prone to erosion and flooding during extreme weather events (Netherlands, Brand et al. (2022); Australia, Cooke et al. (2012), among others). These coastal systems can often be classified as mixed-energy wave-dominated systems (according to Davis Jr and Hayes (1984)) as large swell waves dominate the morphological processes. However, the last decade nourishments have also been constructed in semi-enclosed seas (Mediterranean: Bitan and Zviely (2020), Hanson et al. (2002) and Baltic Sea: Hanson et al. (2002)) and fresh water lakes ('Houtribdijk': Steetzel et al., 2017). Here, the sediment transport dynamics are dependent on the local wind-driven current and fetch-limited wind waves. Furthermore, tidal channel wall nourishments are used since the beginning of the century in the Netherlands (Brand et al., 2022). At these sites, the sediment transport is a result of the wind and tidal driven currents in the tidal channel.

However, little is known about the sediment transport dynamics of nourishments in a sheltered coastal environment. As these sites are sheltered, swell waves dissipate most of their energy and

as a result, tidal currents, wind-driven currents and wind waves are of greater importance. These environments can be found at delta's (Zhu et al., 2014), estuaries (Franz et al., 2017; Mulder & Udink, 1991; Santoro et al., 2017), tidal inlets (De Swart & Zimmerman, 2009; Herrling & Winter, 2014) and back-barrier or bayside beaches (Sorourian et al., 2020; Travers et al., 2010). The sediment transport dynamics at these locations are subjected to the complex interaction between waves, the wind-driven current and wind waves. Under accelerating sea level rise, these sheltered coastal systems are also increasingly threatened by erosion and flooding. Therefore, it is of importance to examine the role of different drivers (waves, tides and wind) characterized by different environmental conditions (spring-neap tides, fair weather, storms) on the sediment transport dynamics for a sheltered coastal system.

Furthermore, nourishments are often constructed with a uniform sediment composition, even though the majority of coastal environments around the world exhibit sediment heterogeneity of an order that can substantially alter sediment-related processes (Holland & Elmore, 2008). For instance, in tidal basins and estuaries, the bed composition between the shoals and the channels often varies substantially. However, spatial heterogeneity of bed sediment composition is often not considered in morphological studies (Huisman et al., 2016). Even though, several studies (Dastgheib, 2012; Huisman et al., 2018; van der Wegen et al., 2011) have already demonstrated the importance of accounting for different sediment fractions in simulating morphological development in coastal systems. Furthermore, the sediment sampling data is often not sufficient to account for the spatial and temporal variations in bed composition (Holland & Elmore, 2008; van der Wegen et al., 2011). As a result, it is difficult to define the initial bed composition so that it correctly represents the system. Therefore, it is essential to examine the influence of graded sediment and initial bed composition on sediment transport.

In order to study the effect of graded sediment and different drivers on sediment transport in a sheltered coastal system, this study aims to model the sediment transport and erosion/deposition patterns at a large-scale coastal intervention, the Prins Hendrikzanddijk (PHZD). The PHZD is a back-barrier beach located on the southeast side of the Dutch barrier island Texel in the Marsdiep basin (figure 1.1). The Marsdiep basin is the largest and westernmost basin of the Dutch Wadden Sea, reaching from the Texel inlet in the west to the Eierland and Vlie basin to the east. Similar to the rest of the Wadden Sea, the Marsdiep basin is a mixed-energy environment with a mean tidal range of 1.4m, mean significant wave height of 1.3m and extreme wave height of over 6m (Elias et al., 2012). Furthermore, the western Wadden Sea can be classified as a multiple tidal inlet systems, and thus, the tides, wind and freshwater discharge can result in a residual flow through the system (Buijsman & Ridderinkhof, 2007).

Prior to the construction of the PHZD, an intertidal flat was located at the study area that eroded as a result of the landward movement of the 'Texelstroom' tidal channel (figure 1.1; Witteveen+Bos (2011)). The PHZD itself consists of a safety dune consisting of relatively fine sand and an erosional wear layer of coarse sediment (figure B.3). Furthermore, the dune consists of a beach area sheltered by the NIOZ harbour (L6 to L4) and a spit area located on the northwestern side of the dune (L4 to L1). Finally, the beach face of the PHZD is steep, increasing in slope from the sheltered beach (average slope $L5 = 1/15.4$) towards the spit (average slope $L2 = 1/12.4$; figure 1.1).

Numerical modelling of graded sediment and bed composition is common for river systems (Klein-hans & van Rijn, 2002; Ribberink, 1987; Sloff & Mosselman, 2012), but limited research has been done in coastal environments. Ribberink (1987) and Sloff and Mosselman (2012) both use a similar model approach to simulate graded sediment transport and bed composition changes in river environments. Both studies, indicate the importance of accounting for multiple sediment fractions and bed composition, but also note difficulties in the proper implementation of both the initial conditions and physical processes. In coastal settings, Van Rijn (1997) showed the capability of a numerical model to reproduce the cross-shore sediment sorting at open ocean, wave-dominated coasts. Furthermore, Huisman et al. (2018) modelled graded sediment transport and bed composition changes for a large-scale sand nourishment in a wave-dominated setting. Huisman et al. (2018) showed that the initial bed composition did not influence the ability of the model to reproduce the observed changes in bed composition, indicating the relative importance of hydrodynamic conditions over the initial bed composition. However, it was also noted that this may be of relevance when the sediment size of the applied sand of the nourishment differs significantly from the natural composition. Furthermore, the application of numerical modelling of graded sediment and bed composition changes for a large-scale, sandy coastal intervention in a sheltered coastal environment is still missing.

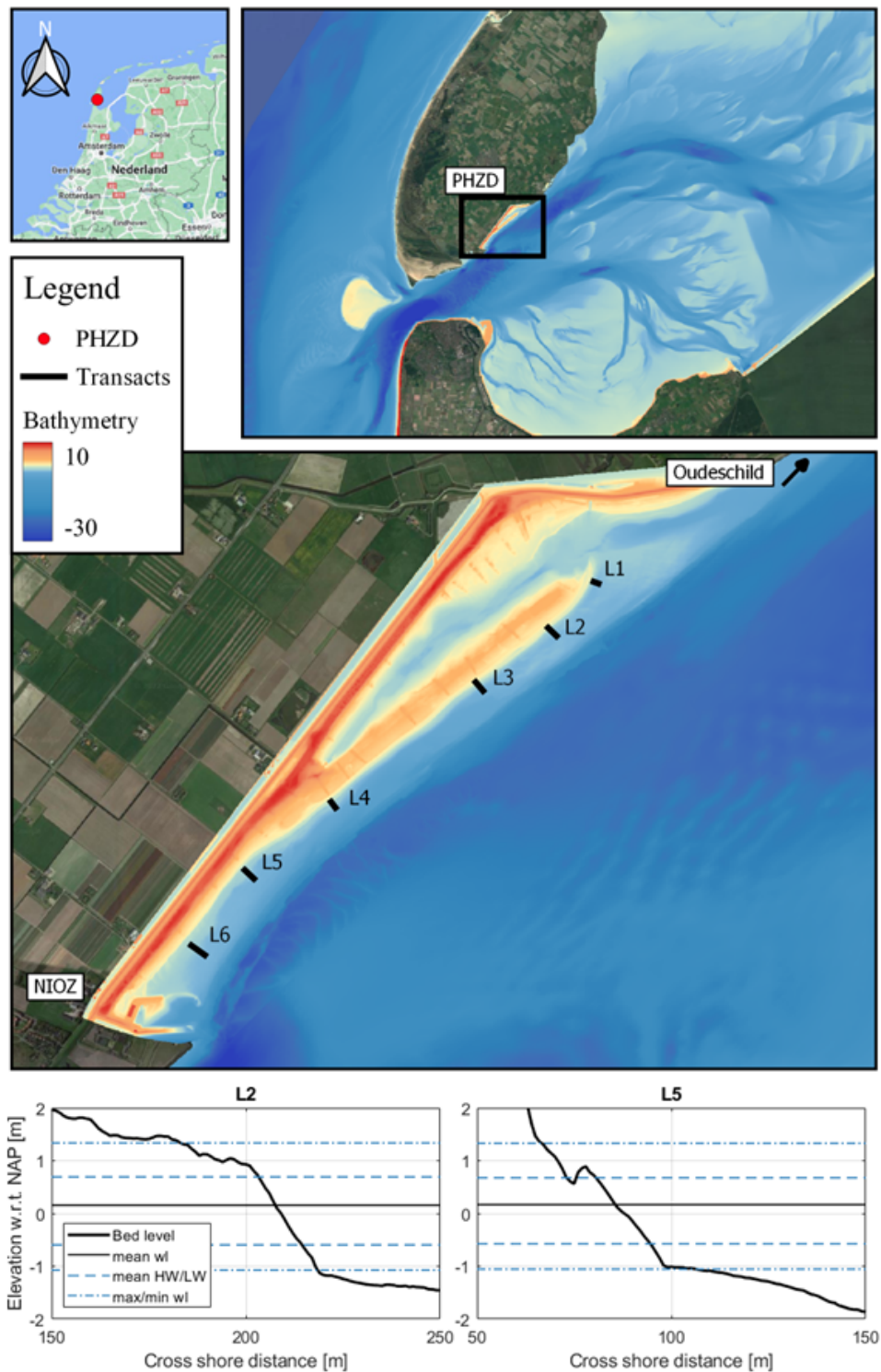


Figure 1.1.: The location of the study site and the surrounding environments. The upper left figure shows the position of the PHZD in the Netherlands. The right upper figure shows the bathymetry of the Marsdiep basin of the western Dutch Wadden Sea. Finally, the lower panel shows the PHZD area with the instrument cross sections.

1.2. Objectives

The objective of this thesis is to assess graded sediment transport and bed composition changes for a large-scale nourishment in a sheltered coastal environment. In order to achieve this objective, two research questions are formulated:

RQ1: *What is the relative importance of different drivers on the transport of sediment with a uniform grain size and the related erosion/deposition patterns in a sheltered coastal environment, during...*

a) *...calm weather conditions?*

b) *...storm conditions?*

RQ2: *What is the effect of graded sediment and initial bed composition on sediment transport and the related erosion/deposition patterns in a sheltered coastal environment, during...*

a) *...calm weather conditions?*

b) *...storm conditions?*

1.3. Methodology

To answer the research questions, a model study was carried out with the hydro- and morphodynamic numerical model Delft3D (Lesser et al., 2004). In this model study, the PHZD is taken as a prototype coastal intervention with graded sandy sediments in a sheltered coastal environment. The Delft3D model consists of several domains covering the Dutch western Wadden Sea and part of the North Sea. Water levels from an operational continental shelf model and observed wave heights from wave buoy observations are forced on the open boundaries. In addition, the observed wind velocity and direction of a nearby weather station are forced spatially uniform to the model. Furthermore, the model is calibrated by systematically varying key parameters in order to fit the model outcome (water level, current velocities and wave parameters) to observational data. The data for the calibration is obtained from the 6-week field campaign at the PHZD and nearby tidal gauges and wave buoys. Subsequently, the calibrated model is used to answer the research questions by systematically varying the boundary conditions and processes included.

2. Theoretical background

The interaction between hydrodynamics and sediment transport is considered a very complex and poorly understood process (Bosboom & Stive, 2021). Especially, in the case of mixed-energy environments consisting of graded sediments. Considering the complexity of the problem, the subsequent section originates from the idealized theory of the physical processes concerning sediment transport. In addition, empirical relations are common in sediment transport and thus these will complement the idealized theory.

2.1. Sediment properties

Several types of sediments (quartz, carbonates and clay minerals) are found in coastal environments and their properties have a profound influence on their entertainment, transport and deposition. Two of the most fundamental properties of sediments are the grain sizes and their distribution. The grain size is the diameter of individual grains and sediments have a certain distribution of grain sizes referred to as the grading or sorting of sediments. Sediments are classified based on the median grain size (D_{50}), distinguishing clay (2 m), silt ($2\text{-}63\ \mu\text{m}$), sand ($63\text{-}2000\ \mu\text{m}$), gravel ($2\text{-}64\ \text{mm}$) and cobbles ($<64\ \text{mm}$; Blott and Pye (2012)). In the definition of grain size, the subscript x in D_x denotes the diameter of a sediment mixture for which the weight is finer by $x\%$. Smaller grains (silt and clay) show cohesive properties (sticking together of particles) while larger particles (sand, gravel and boulders) do not (Van Rijn, 2007b). This study examines the sediment transport of coarse sediment (sand and gravel), therefore only non-cohesive sediment dynamics are discussed. Furthermore, the grading of sediments (D_{90}/D_{10}) can be well sorted (small range of sizes, $D_{90}/D_{10} < 1.5$) or poorly sorted (large range of sizes, $D_{90}/D_{10} > 3$; Bosboom and Stive (2021)).

In addition to grain size and sorting, the density and shape are important grain properties that influence sediment transport (Winkelmolen, 1971). However, for the sake of simplicity, the density of quartz (2650kgm^3) is often taken as constant density as this is the most occurring mineral in coastal sediments. Nevertheless, denser minerals and less dense carbonate sediment are present. For the same reasoning, the shape of the grains is approximated by a perfect sphere. However, the drag forces acting on a grain that is irregular are different from a spherical grain (Hottovy & Sylvester, 1979; Jain et al., 2020).

2.2. Initiation of motion

2.2.1. Forces on a resting particle

The transport of sediment only occurs if the fluid force (drag and lift force) exceeds the resisting force of the grain (gravity force; figure 2.1). For the drag force, the skin friction results from viscous shear between the water and the particle (Van Rijn, 2007a). Furthermore, the flow separation at the downstream end of the particle results in a pressure difference between the up- and downstream side of the grain (Bosboom & Stive, 2021). As a result, there is an additional force in the direction of the current (upper panel in figure 2.1). The lift force results from the flow separation in combination with flow contraction above the grain. The local flow velocity above the grain is higher leading to lower pressure (Bernoulli law) and thus results in an upward force. Both the drag and lift force are proportional to the square of the velocity (u^2), the particle's surface area (D^2) and the water density (ρ_w) (Bosboom & Stive, 2021), thus

$$F_{driving} = F_D + F_L \propto \rho_w u^2 D^2 \quad (2.1)$$

The resisting force consists of the gravity force and is proportional to $(\rho_s - \rho_w)gD^3$ and thus the equilibrium of forces is of the following form:

$$(\rho_s - \rho_w)gD^3 \propto \rho_w u^2 D^2 \quad (2.2)$$

where g is the gravitational acceleration, ρ_s the sediment density and D the particle diameter. The driving drag and lift forces are often reformulated into a time-averaged bed-shear stress per unit surface area (τ ; Van Rijn (2007a)).

2.2.2. Shields parameter

The initiation of motion occurs when the instantaneous bed-shear stress (τ) exceeds a threshold value, defined as the critical bed-shear stress (τ_{cr}). One of the most widely used criteria for the initiation of motion is the dimensionless Shields parameter ($\theta > \theta_{cr}$; (Shields, 1936)). The Shields parameter is the ratio of the driving force (bed-shear stress) over the resisting force (gravity) and is given by

$$\theta = \frac{\tau}{(\rho_s - \rho_w)gD_{50}} \quad (2.3)$$

The Shield parameter depends thus on the hydraulic condition near the bed and properties of the sediment. The critical Shields parameter can be found by replacing the bed-shear stress with the critical bed-shear stress in equation 2.3. Shields (1936) represented the hydraulic condition by

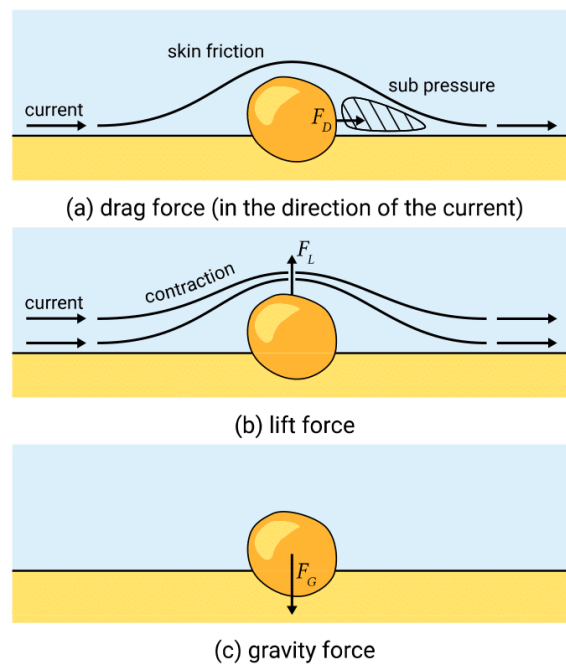


Figure 2.1.: The forces acting on a resting particle (Bosboom & Stive, 2021)

the grain Reynolds number and found an empirical relation with the critical Shields parameter for uniform flow on a flat bed (figure 2.2). Figure 2.2 illustrates the varying behaviour of different grain sizes under the same hydraulic conditions. For instance, the line of $u_* = 0.05 \text{ ms}^{-1}$ intersects the line of $D = 2\text{mm}$ above the threshold of incipient motion, while it intersects the line of $D = 4\text{mm}$ below. Therefore, similar hydrodynamic conditions can lead to preferential entrainment of finer sediment fractions (Komar, 1987). The preferential transport leads to coarsening of the top layer of the bed, known as bed armouring, limiting the transport of additional fine sediment from below (Wiberg et al., 1994). During sufficient energetic conditions, the armour layer may be mixed with the underlying sediment, as all sediment fractions will be mobilized and redistributed. Furthermore, if a particle is situated on a sloping bed, the critical bed-shear stress increases for upslope movement and decreases for downslope movement due to an additional driving gravity force in the downslope direction (Bosboom & Stive, 2021). Bagnold (1966) (longitudinal slope) and Van Rijn et al. (1993) (transverse slope) presented a correction of the transport vectors based on a user-defined parameter, bed slope and the near bed-fluid velocity. Furthermore, Van Rijn et al. (1993) represented the hydraulic condition with dimensionless grain size and empirically determined

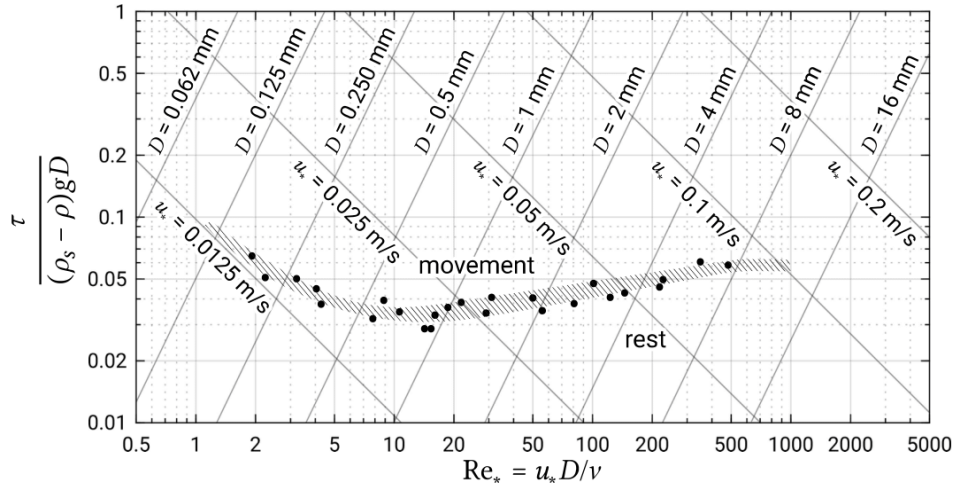


Figure 2.2.: The Shields curve showing the grain Reynolds number on the x-axis and the Shields parameter on the y-axis. The diagonal lines indicate the grain diameter and the critical velocity under constant density $\rho_s=2650 \text{ kg m}^{-3}$ and kinematic viscosity $\nu=1.25 \times 10^{-6} \text{ m}^2 \text{ s}^{-1}$ (from Bosboom and Stive (2021) adjusted from Shields (1936))

the relation with the critical Shields parameter:

$$\theta_{cr} = \begin{cases} 0.24 D_*^{-1} & 1 < D_* \leq 4 \\ 0.14 D_*^{-0.64} & 4 < D_* \leq 10 \\ 0.04 D_*^{-0.1} & 10 < D_* \leq 20 \\ 0.013 D_*^{0.29} & 20 < D_* \leq 150 \\ 0.055 & 150 < D_* \end{cases} \quad (2.4)$$

with the dimensionless grain size

$$D_* = d_{50} \left(\frac{(s-1)g}{\nu^2} \right)^{\frac{1}{3}} \quad (2.5)$$

where s is the ratio between the density of water and sediment and ν is the kinematic viscosity of water.

Finally, after a particle is entrained, the particle motion is the result of a balance between an upward-directed drag force (F_D) and the combined action of gravity and buoyancy (F_G). The combined buoyancy and gravity force for a perfect sphere can be found by subtracting the weight

of the displaced volume of water from the weight of the particle

$$F_G = (\rho_s - \rho) g \left(\frac{\pi}{6} D^3 \right) \quad (2.6)$$

The upward directed drag forces according to Fredsøe (1984) is given by

$$F_D = \frac{1}{2} C_D \rho w_s^2 \left(\frac{\pi}{4} D^2 \right) \quad (2.7)$$

where C_D is the drag coefficient and w_s is the particle fall velocity. In equilibrium, these forces balance each other and the fall velocity is given by

$$w_s = \sqrt{\frac{4(s-1)D}{3C_D}} \quad (2.8)$$

where the fall velocity of a particle depends on the size (D), the density ($s = \frac{\rho_s}{\rho_w}$) and the drag coefficient (C_D). The larger the particle, the higher the fall velocity and thus the faster it settles. As a result, the difference in settling velocity can lead to suspension sorting, as sediment fractions are suspended for different time periods (Inman, 1949).

2.2.3. Hiding and exposure

In the previous section, the forces acting on a solitary particle are discussed. However, a particle is not alone and in a sediment mixture, the surrounding particles have a substantial effect on the initiation of motion. If a bed is poorly sorted ($D_{90}/D_{10} > 3$), the larger grains are more exposed when surrounded by smaller grains while the smaller grains hide in the voids between the larger grains (schematic in the figure 2.3). Egiazaroff (1965) proposed to modify the critical bed-shear stress (θ_{cr}) by a correction factor as a function of the ratio of an individual grain size over the median grain size (second equation in eq. 2.9). As a result, the critical bed shear stress increases (decreases) for small (large) grains (figure 2.3). Ashida and Michiue (1972) adjusted the formulation by Egiazaroff (1965) in order to minimize the effect of hiding on the critical bed shear stress for the smallest particles (Fig. 2.3;eq. 2.9).

$$\xi = \begin{cases} 0.8429 \frac{D_m}{D_i} & \text{if } D_i/D_m < 0.38889 \\ \left(\frac{\log 1019}{\log 1019 + \log 10(D_i/D_m)} \right) & \text{otherwise} \end{cases} \quad (2.9)$$

Furthermore, Parker et al. (1982) formulated the hiding and exposure parameter based on the ratio of the particle size over the median particle size, but with a user-defined parameter ($\xi = \left(\frac{D_i}{D_m} \right)^\alpha$; Fig.

2.3). The alpha parameter allows the user to adjust the effect of hiding and exposure from no correction to the correction of Egiazaroff (1965).

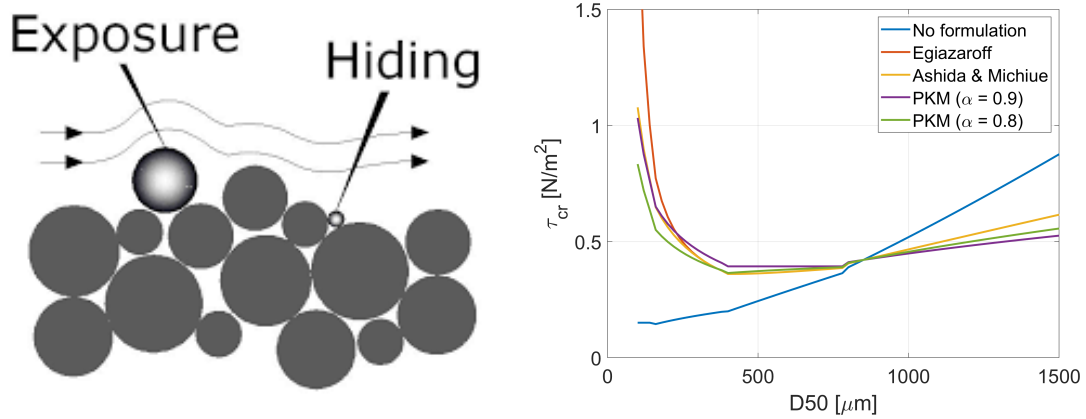


Figure 2.3.: The hiding and exposure visualized, on the left a schematic of the hiding and exposure effect and on the right the effect of different hiding and exposure formulations on the critical bed shear stress (τ_{cr})

2.2.4. Bed-shear stress

The instantaneous bed-shear stress is a function of the driving force (waves or currents) and the friction between the bed and the flowing water. In the case of a flat bed, the friction is only determined by the individual grains (skin friction; upper panel in figure 2.1). However, the bed in coastal environments often consists of bedforms, such as ripples and dunes, which cause additional friction known as bedform-related roughness (Brakenhoff et al., 2020). The bed-shear stress is determined separately for the current- and wave-related component. Several empirical formulations exist for the representation of bottom friction, one of the most commonly used for the current-related bed-shear stress is the Chézy coefficient (Brakenhoff et al., 2020; Dastgheib, 2012; Iglesias et al., 2019; Lenstra et al., 2019). The bed-shear stress due to currents is a function of the Chézy coefficient (friction force) and the current (drag and lift force):

$$\tau_c = \frac{\rho_w g \vec{U} |\vec{U}|}{C^2} \quad (2.10)$$

where \vec{U} is the depth-averaged velocity and the Chézy coefficient is given by

$$C = 18 \log \left(\frac{12h}{k_s} \right) \quad (2.11)$$

2.2. INITIATION OF MOTION

where h is the water depth and k_s is the total bed roughness (both due to skin friction and bedforms). The total bed roughness is a measure representative of bed roughness height and is given in meters.

Furthermore, surface waves cause an orbital motion below the surface that exerts a shear stress on the bed. Therefore, the wave-related bed-shear stress is a function of the peak near-bed orbital velocity (U_δ ; drag and lift force) and the wave friction factor (f_w ; friction force):

$$\tau_w = \frac{1}{4} \rho_w f_w (\hat{U}_\delta)^2 \quad (2.12)$$

where \hat{U}_δ is the peak near-bed orbital velocity and the wave friction factor according to Swart (1974):

$$f_w = 0.00251 * \exp[5.21 * (\frac{A}{k_s})^{-0.19}] \quad (2.13)$$

where k_s is again the measure for the bed roughness and A the orbital excursion length based on linear theory according to

$$A_\delta = \frac{H_{m0}}{2 \sinh(kh)} \quad (2.14)$$

where H_{m0} is the zero-order moment spectral wave height ($\approx H_{1/3}$) and k the wave number.

Furthermore, the steady tidal flow interacts non-linearly with the thin wave boundary layer generated by the oscillatory wave motion (Fredsoe, 1984). The flow and oscillatory motion are dominated by turbulent shear-stresses and thus proportional to the square of velocities (equations 2.10 & 2.12). As a result, the waves affect the currents and vice versa, leading to the enhancement of both the mean and maximum bed-shear stresses (Figure 2.4; Soulsby et al. (1993)). However, as the motion due to waves is oscillatory, the orbital wave motion does not contribute to the mean bed-shear stresses but does lead to occasional high bed-shear stresses. Furthermore, the threshold for the initiation of motion is determined by the maximum bed-shear stress (τ_{max}) while diffusion of suspended sediment and the current velocity are determined by the time-mean bed-shear stress (τ_m) (Figure 2.4; Soulsby et al. (1993)). Therefore, the oscillatory wave motion often stirs sediment while the mean current leads to sediment transport (Fredsoe, 1984; Soulsby et al., 1993).

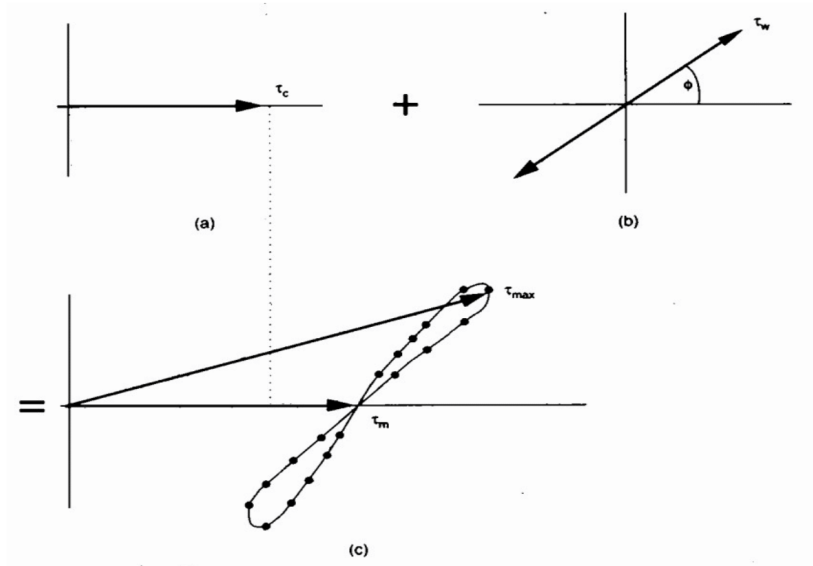


Figure 2.4.: Schematic view of the current-wave interacting bed shear-stresses: a) current related bed shear-stress (τ_c), b) wave related bed shear-stress (τ_w) and c) the combined bed shear stress (τ_{cw}). Furthermore, the time-mean bed shear-stress (τ_m) and the maximum bed shear-stress (τ_{max}) are indicated (from Soulsby et al. (1993)).

2.3. Modes of sediment transport

In order to determine the volumes of erosion and sedimentation, it is important to quantify the sediment transport rates. The mass balance for each sediment size fraction i (Sloff & Mosselman, 2012) is given by:

$$\rho_s(1 - \epsilon) \left(\frac{\partial(p_{i,a})\delta_a}{\partial t} + p_i(z_u) \frac{\partial z_u}{\partial t} \right) + \frac{\partial q_{sqi}}{\partial t} + \frac{\partial q_{syi}}{\partial t} = 0 \quad (2.15)$$

with

$$z_b = z_u + \delta_a \quad (2.16)$$

where ϵ is the porosity of the bed ($\epsilon = 0.4$; Sloff and Mosselman (2012)), $p_{i,a}$ is the proportion of sediment size fraction in the active layer, δ_a is the thickness of the active layer (Fig. 3.8), $p_i(z_u)$ is equal to $p_{i,a}$ during sedimentation while during erosion $p_i(z_u)$ is equal to $p_{i,0}$ (Fig. 3.8), q_{sqi} and q_{syi} are the mass sediment transport components per unit width in the x and y direction per sediment fraction i and $z_b(x, y, t)$ is the change in bed level. Furthermore, the sum of the fractions of the sediment sizes should be 1.

$$\sum_{i=1}^N p_i = 1 \quad (2.17)$$

2.3. MODES OF SEDIMENT TRANSPORT

The mass balance equation shows that when the sum of the sediment transport rates is positive (negative), the bed level increases (decreases). Commonly, sediment transport is separated into bed-load, suspended load and wash load. The wash load consists of fine particles (silts and clay) that are continuously suspended and thus not present in the bed (Fredsoe & Deigaard, 1992). Therefore, the wash load does not contribute to the transport of bed material and thus the sediment transport rate is the sum of the bed-load and suspended sediment transport.

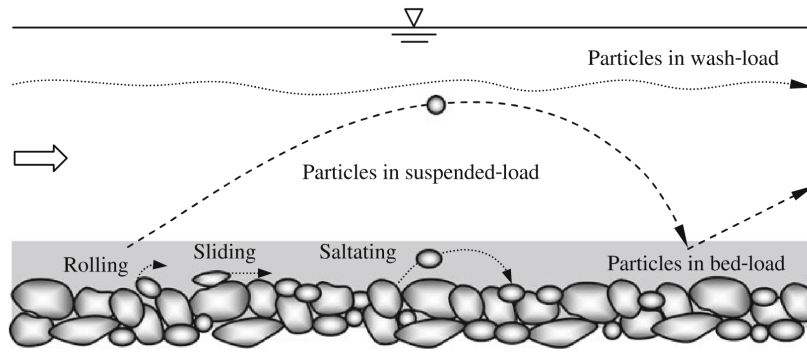


Figure 2.5.: The different modes of sediment transport: wash load, suspended load and bed-load (figure from Dey (2014)).

The bed-load transport of sediment occurs in a thin layer ($z = \delta \approx 1 - 10\text{cm}$) close to the bed by rolling, sliding and saltating (grey shaded area in figure 2.5; Dey (2014)). Therefore, the bed-shear stress at the top of this layer is a key parameter to determine bed-load transport. In the previous section, the bed-shear stress due to currents (eq. 2.10) and waves (eq. 2.12) alone are discussed. However, for sediment transport calculations it is necessary to obtain a bed-shear stress under the combined motion of waves and currents. Van Rijn (2007a) uses a quadratic function of the combined wave-current velocity similar to the suggestion of Grant and Madsen (1979), the combined bed-shear stress for the bed-load is given by

$$\tau'_{cw} = \frac{1}{2} \rho_w f'_{cw} (U_{\delta,cw})^2 \quad (2.18)$$

where $U_{a,t}(t)$ is the total velocity due to waves and currents at the top of the bed-load layer δ and f'_{cw} is the grain friction coefficient due to both currents and waves given by

$$f'_{cw} = \alpha \beta f_c + (1 - \alpha) f_w \quad (2.19)$$

where α is a coefficient related to the relative strength of the wave and current motion, β is a coefficient related to the vertical structure of the current, f_w is the wave friction factor (eq. 2.13) and f_c is the friction factor due to currents ($f_c = \frac{8g}{C}$ with C from eq. 2.11). Subsequently, the

2.3. MODES OF SEDIMENT TRANSPORT

instantaneous bed-shear stress needs to be evaluated with respect to the critical bed-shear stress according to Shields. This is done through the excess shear parameter given by

$$T = \left(\frac{\tau'_{cw} - \tau_{cr}}{\tau_{cr}} \right) \quad (2.20)$$

Finally, the total bed-load sediment transport is given by

$$q_b(t) = \frac{1}{2} D_{50} \rho_s D_*^{-0.3} \left(\frac{\tau'_{cw}}{\rho_w} \right)^{0.5} T \quad (2.21)$$

At low bed-shear stresses (Shields parameter $< 0.8-1$) the bed-load transport occurs primarily through the migration of small-scale bed forms while at high bed-shear stresses (Shields parameter $> 0.8-1$) the bed-load is in the form of sheet flow (Bosboom & Stive, 2021). In both cases, the sediment transport is strongly related to the particle-particle interaction and gravity.

Suspended transport concerns particles that are suspended for a longer period of time due to fluid turbulence above the threshold of motion. For a sediment grain to remain in suspension, the upward force due to the turbulent motion of the velocity must be larger than the settling velocity. Once sediment is in suspension it is assumed to move with the water velocity and thus the suspended sediment flux can be computed from the concentration profile and the vertical velocity distribution (Bosboom & Stive, 2021). Integrating from the top of the bed-load layer ($z = \delta$) to the instantaneous water level (h) leads to

$$q_s(t) = \int_{\delta}^h u(z, t) c(z, t) dz \quad (2.22)$$

where $u(z, t)$ is the vertical velocity distribution, $c(z, t)$ is the concentration profile and h the water depth. When dealing with combined wave-current motion, the velocity and current consist of a mean and an oscillatory part. Furthermore, the water depth consist of a constant value (\bar{h}) and a time-varying tidal component (\tilde{h}) and thus $h = \bar{h} + \tilde{h}$. Therefore, the time-averaged suspended sediment transport can be divided into a current-related (mean current), a wave-related (oscillatory motion) and a tidal wave (difference between high and low water) component as follows

$$\langle q_s \rangle = \underbrace{\int_{\delta}^h UC dz}_{\text{current-related part}} + \underbrace{\int_{\delta}^h \langle \tilde{u} \tilde{c} \rangle dz}_{\text{Wave-related part}} + \underbrace{\int_{\bar{h}}^{\bar{h} + \tilde{h}} uc dz}_{\text{Tidal wave-related part}} \quad (2.23)$$

In many cases, the current-related term will be larger than the wave-related term (Bosboom & Stive, 2021) and the last term can be neglected if $\bar{h} \gg \tilde{h}$. The suspended sediment transport is dependent on the concentration profile which is largely determined by the fall velocity, the grain

size and the bed-shear stress. A widely applied method is based on reference concentration at the top of the bed-load layer (c_δ) and assumes a parabolic distribution of the diffusion coefficient with water depth as suggested by Einstein (1950) and Rouse (1950). The resulting Rouse profile (for derivation see Bosboom and Stive (2021) and Soulsby et al. (1993)) is computed as follows

$$\frac{c}{c_\delta} = \left(\frac{(h-z)}{2} \frac{\delta}{(h-\delta)} \right)^{z_*} \quad (2.24)$$

where h is the water depth, z is the height above the bed, δ is the reference level and z_* is the Rouse number defined as $z_* = \frac{w_s}{\kappa u_*}$. The reference level (δ) is the maximum value of half the wave-related and half the current-related bed roughness value. Here w_s is the fall velocity, κ is the Kármán coefficient ($= 0.4$) and u_* is the shear velocity related to the bed-shear stress through $\tau_{cw} = \rho u_* |u_*|$. The c_δ is the near-bed reference concentration based on the bed-shear stress due to waves and currents (T; eq. 2.20) according to

$$c_\delta = 0.015 \frac{d_{50}}{\delta} \frac{T^{1.5}}{D_*^{0.3}} \quad (2.25)$$

2.4. Sediment transport mechanisms

Morphological change only occurs if there is a net sediment transport over a certain time period (f.i. a day, a month or a year). For a symmetric and sinusoidal wave, the crest and trough phase are identical, and thus sediment is transported back and forth over a wave period. Therefore, no net sediment transport takes place if the wave is symmetric and there is no mean current is present. In the subsequent section, the mechanisms that result in a net sediment transport are discussed.

2.4.1. Tides

First of all, since the tide is a sum of sinusoidal components (astronomical constituents), the distortion of the tide in the confinement of tidal basins leads to the non-linear growth of higher harmonics or overtides (Friedrichs & Aubrey, 1988). The combination of the principle tide and its higher harmonics result in an asymmetry in the periodic tidal velocity with respect to the slack water point (Van de Kreeke & Robaczewska, 1993). Along the Dutch coasts, the semi-diurnal lunar tide (M2) is the dominant astronomical constituent with the first harmonic (M4) as the most significant overtide. The combination of these two harmonics is used to demonstrate the sediment transport mechanism due to tidal asymmetry. However, other semi-diurnal and diurnal tidal constituents also contribute to the tidal signal and thus the asymmetry.

Following Friedrichs and Aubrey (1988), the tidal velocity can be modelled by the superposition of the M2 and M4 tidal waves as follows

$$V = v_0 + v_{M2} * \cos(\omega t - \phi_{M2}) + v_{M4} * \cos(2\omega t - \phi_{M4}) \quad (2.26)$$

where v_0 is a mean tidal current, v_{M2} and v_{M4} are the velocity amplitude of the M2 and M4 tide, ω is the tidal frequency, t is the time and ϕ_{M2} and ϕ_{M4} is the phase of the M2 and M4 tide. A net sediment transport can be driven by a mean tidal flow due to residual eddies or through flow (Ridderinkhof, 1988). In addition, the form of the tidal asymmetry is a function of the relative phase difference between the M2 and M4 tide ($\Delta\theta = 2\theta_{M2} - \theta_{M4}$) and can result in a velocity or duration asymmetry (figure 2.6). First of all, the velocity asymmetry is the consequence of the alignment of the M2 and M4 peaks ($\Delta\theta = 0^\circ$) leading to an asymmetry in peak velocity for the ebb and flood current (a in figure 2.6). As both the bed-load ($q_b \propto u^3$; eq. 2.21) and suspended ($q_s = uc$ with $c \propto u^2$; eqs. 2.22 & 2.25) sediment transport have an exponential relation with the velocity, the velocity asymmetry leads to a net sediment transport (shown in panel c in figure 2.6 for suspended sediment transport).

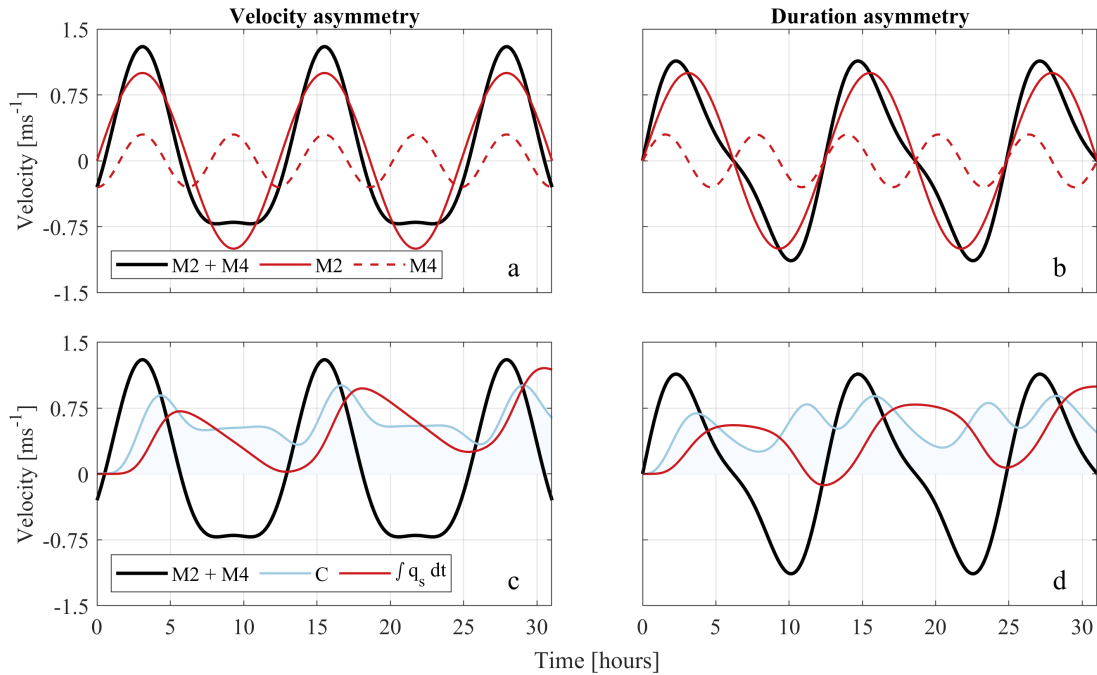


Figure 2.6.: The velocity (left) and duration (right) asymmetry for the principle M2 lunar tide and the M4, the first harmonic of M2. The M2 amplitude = 1m and the M4 amplitude = 0.3m. The concentration in panel c and d is computed with equation 2.27 and the cumulative suspended sediment transport is computed with the simple relation $q_s = \int C u^3 dt$. Both the concentration and sediment transport have an arbitrary scale.

The duration asymmetry ($\Delta\theta = \pm 90^\circ$), a difference in the time from ebb to flood and flood to ebb, leads to a local settling lag (Groen, 1967). The time evolution of the concentration is affected by the settling lag, as particles entrained during the ebb (flood) phase are still in suspension during the flood (ebb) phase. A simple equation for the concentration following De Swart and Zimmerman (2009) is given by

$$\frac{\partial C}{\partial t} = \alpha u^2 - \gamma C \quad (2.27)$$

where C is the concentration, u is the velocity, t is the time, α is the erosion coefficient and γ is the deposition coefficient which is a function of the fall velocity of a particle. This mechanism only holds for fine sediment as coarse sediment will settle down quickly during lower velocities (high γ). For example, if a flood dominance is present, the maximum ebb current is preceded by a longer period of low velocities than the maximum flood current (panel b in figure 2.6). Therefore, more particles have settled before the maximum ebb current relative to the maximum flood current. As a result, the concentration, and thus suspended sediment transport, is larger during flood than during ebb (panel d in figure 2.6).

2.4.2. Waves

In addition to the tides, short waves can also lead to a net sediment transport due to wave-driven currents and wave-shape asymmetry. The wave energy balance in the coastal zone, under stationary wave conditions, is given by

$$\frac{\partial}{\partial x}(E c_g \cos \theta) + \frac{\partial}{\partial y}(E c_g \sin \theta) = -D_f - D_w \quad (2.28)$$

with the total wave energy, given by $E = \frac{1}{8} \rho H_{rms}^2$, is propagated at the wave group velocity (c_g) in the wave direction (θ) (Bosboom & Stive, 2021). The energy propagation is balanced by the dissipation of energy through wave-breaking (D_w) and friction (D_f). When a wave propagates to a water depth of about half the wavelength, the waves will interact with the bed leading to a decrease in wavelength and propagation speed. As a result, the waves in deeper water catch up with waves in shallower water leading to an increase in wave height, this process is called shoaling (Holthuijsen, 2010). Furthermore, if waves arrive at an angle or the bathymetry is non-uniform in the alongshore direction, the changes in water depth are not uniform along the wave crest. As a result, part of the wave crest slows down leading to refraction (waves at an angle) or diffraction (non-uniform coast) towards the coast.

Furthermore, during the process of shoaling, the shape of the wave and orbital motion exerted on the bed become increasingly non-linear due to the amplification of higher harmonics (Ruessink

et al., 2012). The non-linear wave shape first changes into an asymmetry about the horizontal axis (skewness) and secondly asymmetry about the vertical axis (asymmetry). The asymmetric shape of the orbital motion results for both cases in onshore directed transport (Hoefel & Elgar, 2003; Ribberink & Al-Salem, 1994), similar to the net sediment transport due to tidal asymmetry. Morphodynamic modelling is often based on linear wave theory, as wave shape is a non-linear process, there is a need for parameterization. Ruessink et al. (2012) developed a parameterization based on the Ursell number that determines the non-linearity of waves as a function of water depth, wave height and wave period.

Waves do not only transport energy but also momentum: the product of a mass (the mass of a water particle) and velocity (the motion of the water particle). Therefore, the momentum is a vector quantity and the total amount of momentum per unit surface area in the direction of the wave (Bosboom & Stive, 2021; Holthuijsen, 2010) is given by

$$q = \int_{-h}^{\eta} \rho u dz \quad (2.29)$$

where η is the water level variation due to short waves and u the orbital velocity. The amplitude of the orbital velocity according to linear theory is given by

$$\hat{u}(z) = \omega a \frac{\cosh k(h+z)}{\sinh kh} \quad (2.30)$$

with ω the angular frequency, a the wave amplitude, k the wavenumber and L the wavelength. As the amplitude of the orbital velocity (vertical and horizontal) increases with water depth, the motion in the direction of the wave propagation during the crest is larger than the motion in the opposite direction during the trough. As a result, there is a net mass flux between the wave trough and crest for non-breaking waves in the direction of wave propagation ($q_{non-breaking}$).

In shallow water, the shoaling process leads to a decrease in wave speed while the wave height increases. As the orbital motion is proportional to the wave amplitude (eq. 2.30), the horizontal particle velocity exceeds the wave speed leading to depth-induced breaking. In addition, breaking waves transfer part of their energy into turbulent kinetic energy in the form of a roller (q_{roller}). The roller is a layer of air and water acting as a temporary storage of energy and momentum (Bosboom & Stive, 2021). Therefore, there is a net mass flux on the surface in the direction of the propagation due given by

$$q_{drift} = q_{non-breaking} + q_{roller} = \frac{E}{c} + \frac{\alpha E_r}{c} \quad (2.31)$$

with E the wave energy, c the wave speed and α a roller coefficient (derivation in Bosboom and

Stive (2021)). The net onshore mass flux between the wave trough and crest leads to water piling up at a coastal boundary. As a result, an offshore-directed return flow exists near the bed to compensate for the mass flux near the surface, known as the undertow (Fredsoe (1984); figure 2.7). As the current needs to compensate for the onshore mass flux, the depth-averaged velocity is given by

$$U_{undertow} = -\frac{q_{drift} \cos \theta}{\rho h} \quad (2.32)$$

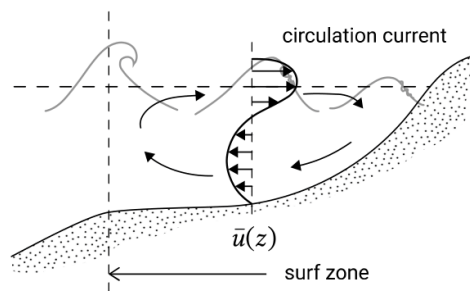


Figure 2.7.: The circulation current in the nearshore zone due onshore transport near the surface and a return flow near the bottom.)

Furthermore, the flux of wave-induced momentum between locations results in a force, known as radiation stresses (Longuet-Higgins & Stewart, 1964). The momentum flux consists of wave-induced momentum transfer through a plane by the particle velocity and a wave-induced pressure force (Fredsoe, 1984). The radiation stress tensors, shown in figure 2.8, are proportional to the wave energy and thus the wave height. Therefore, spatial differences in the wave height, arising due to wave transformation, result in spatial changes in radiation stress. These horizontal gradients in the radiation stress lead to a residual wave-induced force (Bosboom & Stive, 2021).

In the cross-shore momentum balance, the radiation stress gradient normal to the coast is compensated by a change in water level (set-up, set-down) according to

$$\frac{d S_{xx}}{d x} = -\rho g h \frac{d \bar{\eta}}{d x} \quad (2.33)$$

The increase in wave height due to shoaling leads to a positive radiation stress gradient resulting in a set-down. On the contrary, the decrease in wave height due to wave breaking results in a set-up near the coast. Furthermore, the normal radiation stress parallel to the coast (S_{yy}) only results in a residual stress if the wave height is alongshore variable. Finally, the long-shore gradient in the radiation shear stress drives an alongshore current in the direction of wave propagation. The gradient in the radiation shear stress arises from waves arriving at an angle. As a result, the wave

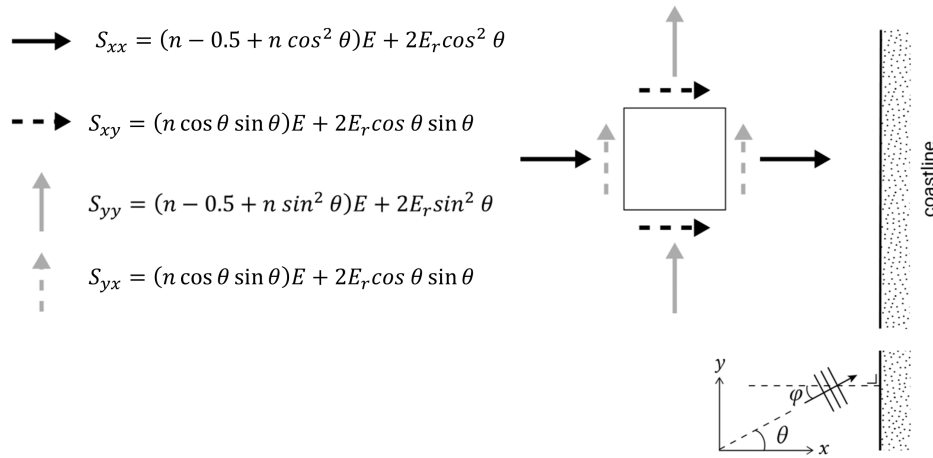


Figure 2.8.: The radiation normal and shear stress tensors with the first term from linear theory and the second term from the wave roller. Adjusted from Bosboom and Stive (2021)

crest transforms non-uniform in the alongshore direction. The radiation shear stress is given by

$$\frac{d S_{xy}}{d x} = -\tau_{b,y} \approx -\rho c_f |\bar{v}| \bar{v} \quad (2.34)$$

with $\tau_{b,y}$ the residual force in the long-shore direction, c_f the friction coefficient and \bar{v} the alongshore current. The derivation of the radiation stresses and for further detail, the reader is referred to textbooks of Bosboom and Stive (2021), Fredsøe (1984), and Holthuijsen (2010). Finally, figure 2.9 summarizes the different wave-induced mean currents and wave asymmetry for the near-shore zone.

2.4.3. Wind

The wind exerts a shear stress on the water surface resulting in water motion in roughly the same direction as the wind. Furthermore, in multiple-inlet tidal embayments wind can cause a mean current between the two inlets (Buijsman & Ridderinkhof, 2007). The direction and intensity of the mean residual current is dependent on the wind direction, wind velocity and the geometry of the basin. The residual current can have a significant contribution to the overall mean current (Duran-Matute et al., 2016).

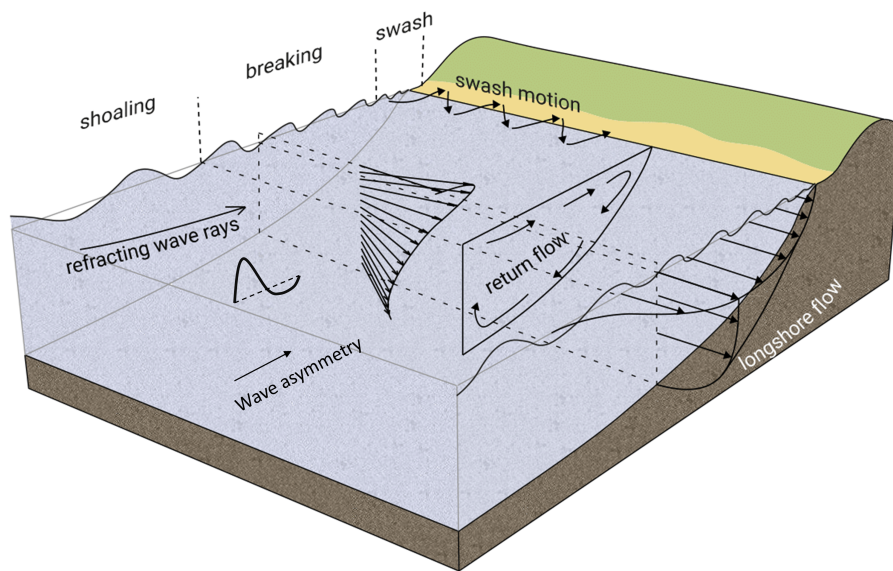


Figure 2.9.: Wave-induced currents and fluxes in the near-shore zone. The circulation flow arising from the mass transport from wave trough to crest and the resulting return flow, undertow. The alongshore current is a result of gradients in the radiation shear stress and the wave-averaged transport due to wave asymmetry. Adjusted from Bosboom and Stive (2021)

3. Materials and methods

3.1. Observations

3.1.1. SEDMEX field campaign

The SEDMEX (mixed SEDiments in Mixed Energy eXperiment) field campaign lasted from 7 September to 19 October 2021 during which a wide variety of instruments were deployed, GPS measurements were performed and sediment samples were collected. The instruments measured subtidal wave height with a pressure sensor at a depth of $-1.40\text{m} + \text{NAP}$ and near-shore current velocity with an Acoustic Doppler Velocimeter at $-0.75\text{m} + \text{NAP}$. Furthermore, along each transect the bed level was measured at a two to three-day interval. Finally, high temporal resolution sediment samples of the top layer ($\sim 5\text{cm}$) were taken at several cross-shore locations along the L2 transect. In the long-shore direction, lower temporal resolution sediment samples were taken.

The data collected during the SEDMEX field campaign is extensively analyzed in two master theses. First of all, Woerdman (2022) examined the alongshore variability in the hydrodynamics along the dike and its implications for sediment transport. Second of all, Klein Obbink (2022) focused on the morphological evolution and bed composition changes along a single transect. In the present study, the outcomes of these two studies and a selection of the collected data are used to relate the bed composition changes to the hydrodynamic conditions along the dike. For more details about the data collection and processing, the reader is referred to (Klein Obbink, 2022; Woerdman, 2022).

3.1.2. Wind forcing and hydrodynamic conditions

During the SEDMEX field campaign, the tidal range varied between a minimum of 0.57m and a maximum of 1.87m during roughly 3 spring-neap cycles (yellow line in Figure 3.1). Furthermore, the lowest water level was -1.07m while the highest water level reached 1.34m (blue line in Figure 3.1). In addition to the astronomic tidal driven transport, there was also a residual current which is almost exclusively positive and reached a maximum of 0.37m (black line in the upper panel of figure 3.1). The mean wind velocity measured is 4.8ms^{-1} while during stormy periods the velocity reached values over 10ms^{-1} (red line in figure 3.1). Furthermore, the wind direction shows quite some variance, but the highest velocities are the results of the dominant west and south wind direction (figure 3.2 & ??). The wind field during the SEDMEX campaign represents the longer-term conditions fairly well (figure ??). Nevertheless, more extreme storm conditions from all direction are observed. Furthermore, the wave height has a mean value of 0.13m and a maximum

3.1. OBSERVATIONS

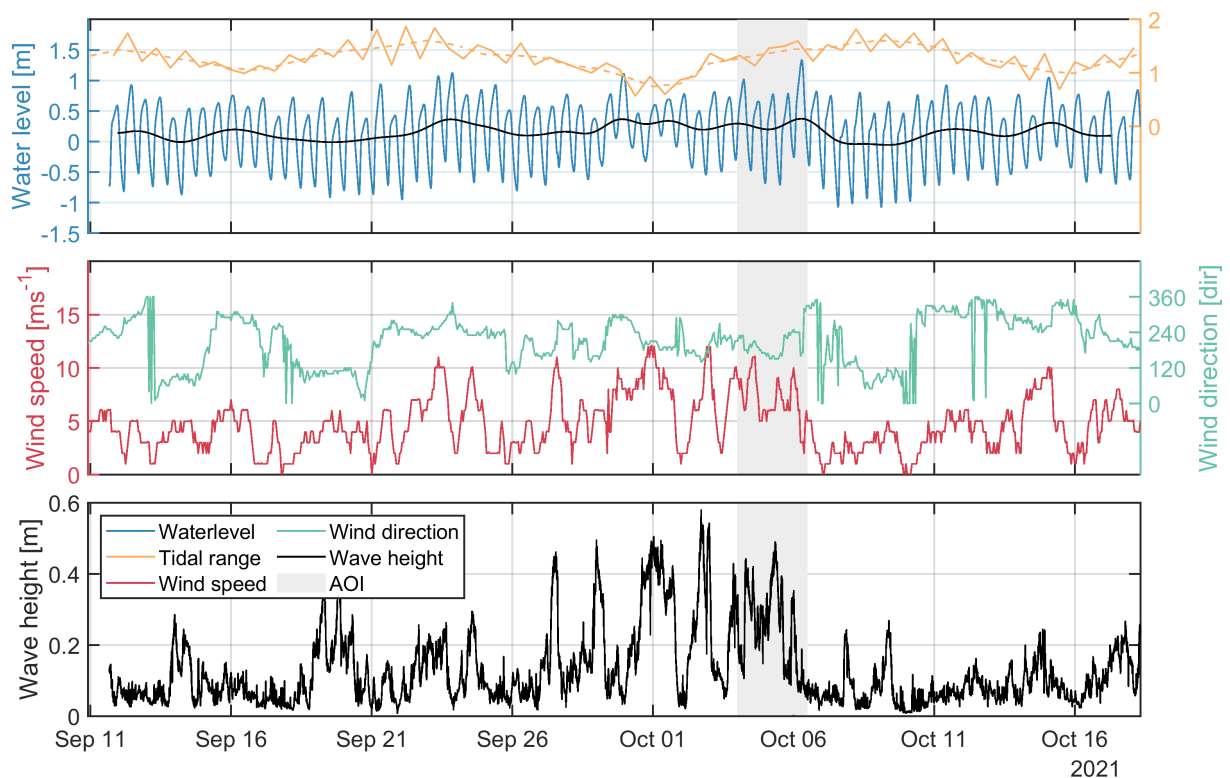


Figure 3.1.: The observed water level and tidal range (upper), wind direction and wind velocity (middle) and wave height (lower) for the SEDMEX field campaign. The grey shaded area indicates the area of interest (AOI) used in the Delft3D simulations.

value of 0.58m (black line in the lower panel of figure 3.1). The periods of large waves correlate to the highest measured wind velocities. Finally, the wave height is related to wind direction, as waves only grow relatively large from winds coming from the southwest to the east (figure 3.2).

Woerdman (2022) found several hydrodynamic gradients in the long-shore direction as a result of the sheltering effect of the NIOZ harbour (figure 1.1). First of all, wave heights increased further away from the harbour under similar forcing conditions. Second of all, the more exposed spit (L4-L1) showed a dominance in flood peak currents and a residual flow from SW to NE. On the contrary, along the sheltered beach (L5-L6) the residual flow was in the ebb direction. Furthermore, the current velocities are dominantly in the along-shore direction, differing almost a magnitude of order. However, this difference is smaller at the sheltered beach due to relatively higher importance of a re-circulation cell (Woerdman, 2022).

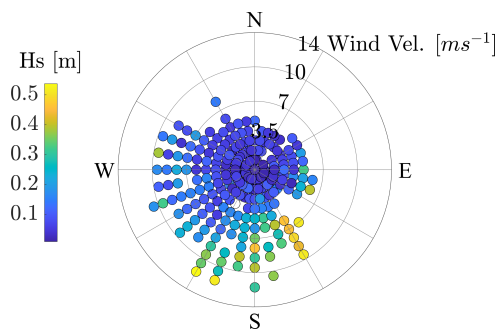


Figure 3.2.: Wave-wind rose with wind data from the 'de Kooy' weather station of the KNMI and wave heights from the SEDMEX field campaign. The colours indicate wave height, the radial axis shows direction and the magnitude of the wind is given by the distance from the centre.

3.1.3. Sediment size fractions

The Schanserwaard shoal below the PHZD dike consists for a substantial part of finer material compared to the sediment used for the construction of the PHZD (figure 3.3). Furthermore, the samples taken during the SEDMEX field campaign show a coarser grain size distribution compared to the sediment used during the construction (figure 3.3). A possible explanation is the accumulation of coarser sediment in the upper layer of the bed and by the shells and shell fragments in the sediment samples. The sediment composition of the top layer of the bed shows relatively fine sediments at the sheltered beach and spit while the centre of the PHZD shows a coarser composition (middle panel in figure 3.3). In addition, there is a fining trend towards the plateau of the deeper located Schanserwaard shoal below the PHZD (right panel in figure 3.3). Therefore, it is likely that little sediment of the Schanserwaard inter-tidal flat was transported towards the PHZD.

3.1.4. Bed composition change and morphological change

The bed level changes along the dike show erosion and flattening of the beach face along the dike and sedimentation at the spit (figure 3.4). This trend was predicted during the design of the dike (Perk et al., 2019) and confirmed by the data analysis of klein Obbink (2022) and Woerdman (2022).

Furthermore, klein Obbink (2022) came up with a conceptual model for the morphodynamic changes at L2. The bed composition of the top layer becomes coarser and the bed face steeper during calm conditions while during storm conditions the bed composition of the top layer becomes finer and the beach face more gentle. Although the data in the long-shore direction is of much lower resolution, the area from L2 to L4 seems to show similar behaviour in bed composition and beach face changes (figure 3.5). This corresponds to the area with more energetic conditions

3.1. OBSERVATIONS

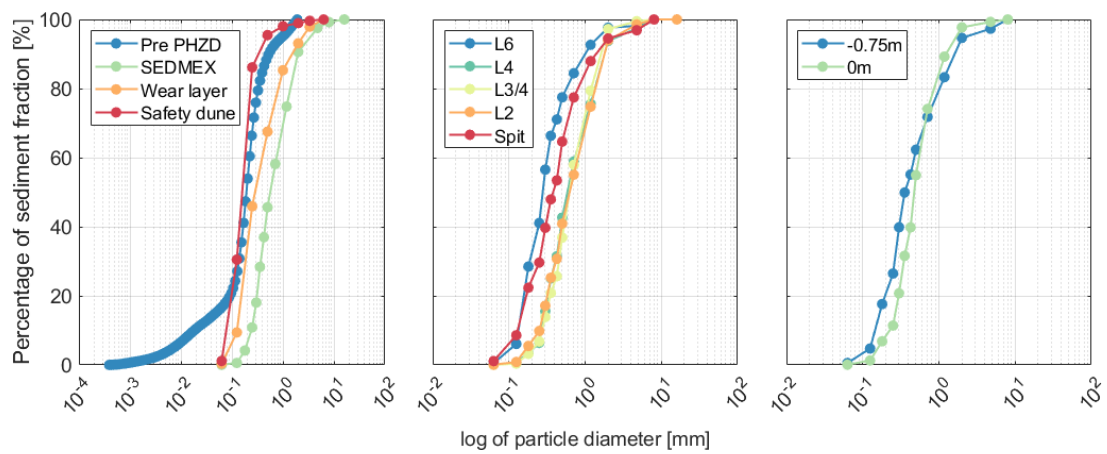


Figure 3.3.: Sediment size distribution of the PHZD. The left panel shows the distribution prior to the construction of the dike (blue), during the SEDMEX campaign (green) and the sediments used for the safety dune (red) and erosional wear layer (orange)). The two other panels show the size distribution of the PHZD area during the SEDMEX campaign differentiating between long-shore location (middle) and depth (right)

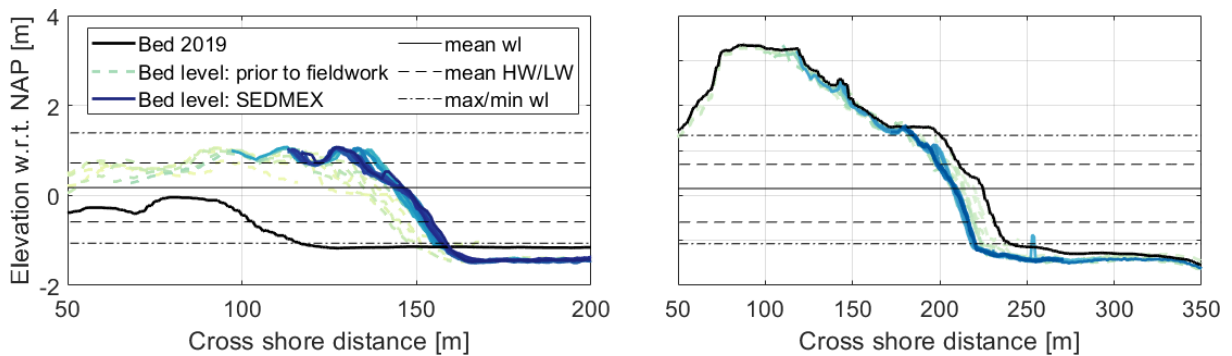


Figure 3.4.: Cross section indicating the bed level changes since the construction of the dune. Erosion of the centre of the dune (left) and sedimentation at the spit (right)

Woerdman (2022). In contrast, the sheltered beach and the spit do not show a clear trend in bed composition changes. Nevertheless, the slope of the beach face does show a similar pattern as the area between L2 and L4. Finally, both the data studies of klein Obbink (2022) and Woerdman (2022) predict preferential transport of fine material towards the spit as a result of hydrodynamic gradients and daily conditions close to critical bed shear stress of incipient motion. The sediment composition variability along the PHZD support this theory as finer sediments are found at the spit (figure 3.3).

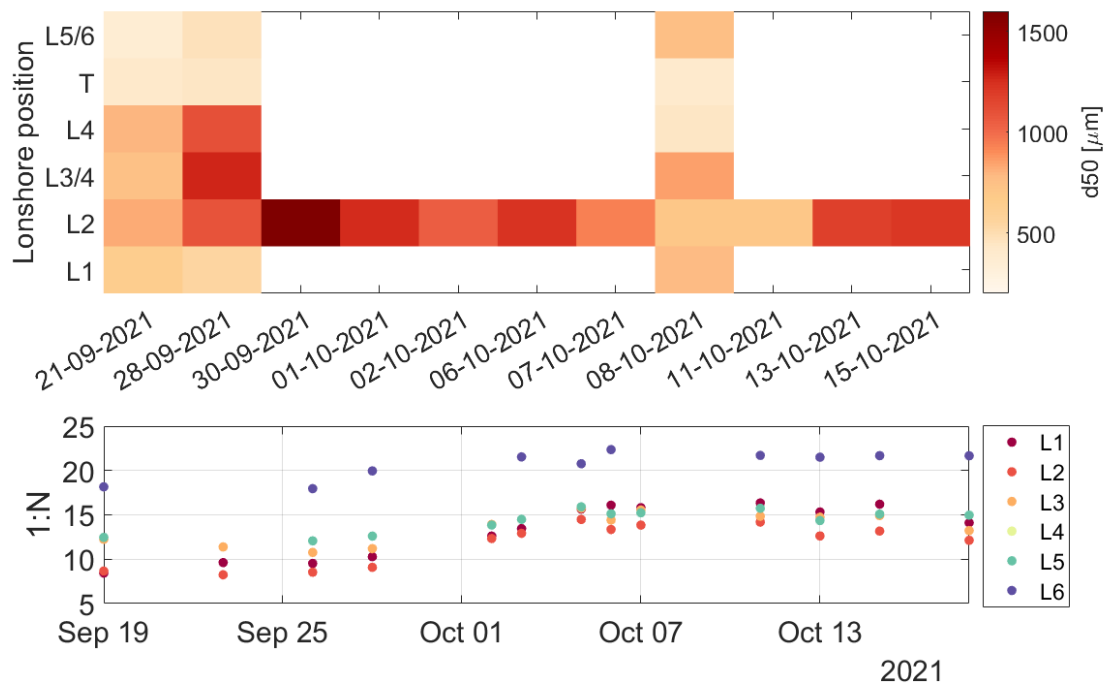


Figure 3.5.: The bed composition and slope changes during the SEDMEX field campaign

3.2. The Delft3D model set-up

Delft3D-FLOW is a numerical, morphodynamic model that solves the depth-averaged, unsteady shallow-water equations on a staggered grid (Lesser et al., 2004). The Delft3D-flow model performs online computation of the sediment transport and morphological changes. Furthermore, the model can be online coupled with the third generation spectral wave model SWAN (Simulating Waves Nearshore; Booij et al. (1999)). The SWAN model describes the wave field with the two-dimensional wave action density spectrum that accounts for the refractive propagation over arbitrary bathymetry and current fields (Booij et al., 1999). The output of the SWAN model consists of wave heights, orbital velocities, wave period, wavelength and bed-shear stress due to waves. Through the online coupling, two-way wave-current interaction between Delft3D-FLOW and SWAN, these wave parameters are communicated to the FLOW module. The Delft3D-FLOW module computes the depth average velocity, water level and bed-shear stresses due to the combined action of waves and currents. Subsequently, the sediment transport and bed level changes are computed according to the theory discussed in section 2. Finally, the water level, current velocities and bed levels are communicated back to SWAN.

In addition, the following effects of the flow on the waves are taken into account: set-up, current

3.2. THE DELFT3D MODEL SET-UP

refraction and enhanced bottom friction. Furthermore, the following effect of waves on the flow are taken into account: enhanced turbulence, friction on the current and enhanced bed-shear stresses. The set-up of the model and the feedbacks between the components are illustrated in figure 3.6. In addition, the model uses a staggered grid and the Alternating Direction Implicity (ADI) time integration method (Deltares, 2014). The ADI method divides one time step into two stages, solving each separately with at least second-order accuracy in space. Finally, the initial model set-up was provided by WaterProof Marine Consultancy BV. (personal communication with WaterProof, October 2022)

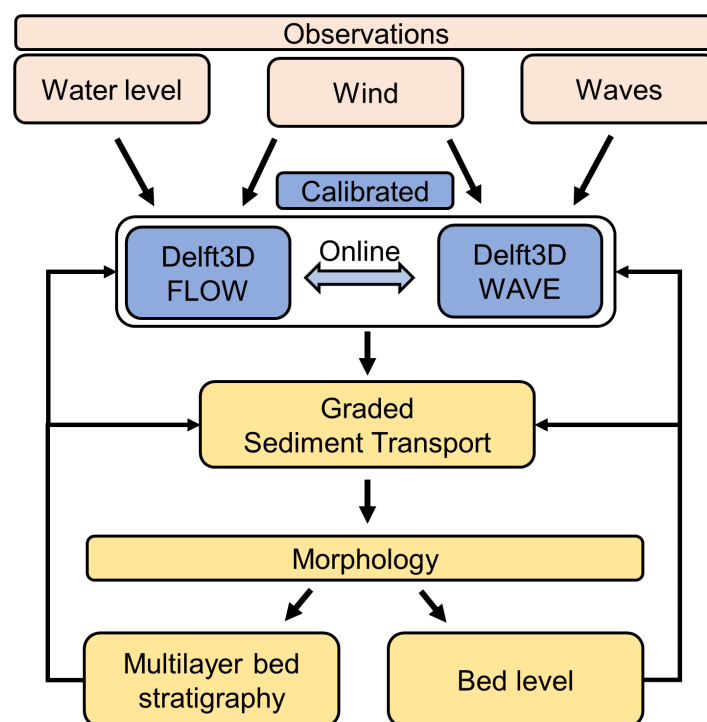


Figure 3.6.: Flow chart of the model set-up and input parameters.

The model is made up of three curvilinear grids that cover the dutch Wadden Sea and a roughly 20km band of the North Sea from the north holland coast to the most eastern tip of Terschelling (Fig. A.2). The three grids are divided with the domain decomposition technique which allows the computation of each grid separately. As a result, these computations can be carried out simultaneously (parallel computing) and thus the computation time is greatly reduced. The different grids communicate through internal boundaries called domain decomposition boundaries (DD-boundaries; striped line in Fig. A.2). As the computations for the different grids are performed simultaneously, the grid resolution can differ per grid. Therefore, the resolution can be enhanced locally while keeping it low further away from the area of interest (Table 3.1), resulting in a decrease in computation

time.

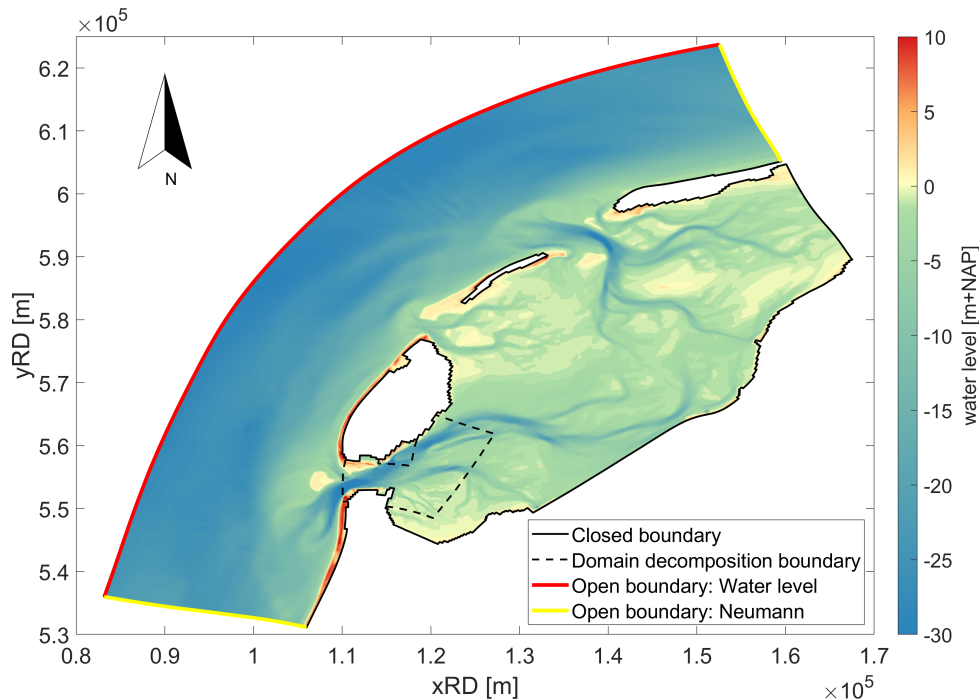


Figure 3.7.: The Delft3D model domain shows the three different grids and the bathymetry. The black lines indicate closed boundaries, the striped line indicates domain decomposition boundaries, the red line indicates an open boundary forced with water level time series and the yellow lines indicate an open boundary with Neumann time series.

Table 3.1.: Table showing the minimum and maximum grid size per grid

Grid	Min grid size [m]	Max grid size [m]
1	400x400	500x1300
2	90x90	140x140
3	7x14	10x12

The boundary conditions of the model are imposed along three boundaries: times series of the water level on the seaward boundary and water level gradient time series (Neumann boundary conditions) along the southern and northern boundary (Fig. A.2). The hourly water level data is retrieved from the Dutch Continental Shelf Model (RWS-WVL & Deltares, 2017) which is accessible through the MATROOS website (<https://noos.matroos.rws.nl/>) of the RWS (Department of Waterways and Public Works). The water level is interpolated to a time series with a 10 minutes interval with a spline interpolation. Furthermore, the seaward boundary is divided into 25 sections in order to account for the gradient in water level along the boundary. For each of these sections the water level of the two outer grids is given as input and in between the water level is linearly interpolated

3.2. THE DELFT3D MODEL SET-UP

to the other grids. Along the northern and southern boundary, a Neumann boundary is chosen in order to not over constrain the model. For both Neumann boundaries, the spatial gradient in the direction of the tidal wave is determined for both outer grids of the boundary. Furthermore, the data of the swell wave conditions on the North Sea are retrieved from several wave buoys of RWS (<https://waterinfo.rws.nl/>). Finally, the hourly wind velocity and direction are taken from a nearby weather station (de Kooy) from the KNMI.

The bathymetry of the model is a composition of three bathymetric measurement campaigns. First of all, the PHZD area is measured 4 times a year by Jan de Nul (design company) and the 2021 first quarter measurement was used (the latest measurement available at the time of creation). Secondly, the bathymetry of the dutch coastal waters is measured every couple of years by RWS, known as 'Vaklodingen'. From these measurements, the 2015 complete Wadden Sea and 2018 Marsdiep basin data were taken and combined.

The bed composition changes are administrated with a multi-layer bed stratigraphy with an active layer approach (Huisman et al. (2018), Ribberink (1987), and Sloff and Mosselman (2012); Fig. 3.8). In such an approach, the changes in the fraction of each sediment size fraction is registered per layer and per grid cell. The sediment transport for a grid cell is calculated separately for each sediment fraction and than reduced proportional to the availability of that sediment fraction in the active layer (eq. 2.15; figure 3.8). Next to that, the critical bed shear stress for each fraction is corrected by the corresponding hiding and exposure factor (eq. 2.3).

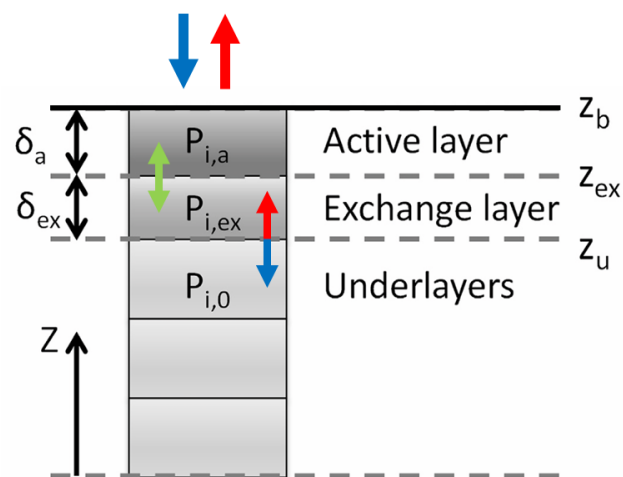


Figure 3.8.: The multilayer bed stratigraphy method within Delft3D where red arrows indicate erosion, blue arrows sedimentation and the green arrow exchange of sediment size fractions (adjusted from Huisman et al. (2018))

In this study, the multi-layer bed stratigraphy is used with and without bed level updating. In the set-up without bed level change, only the bed composition changes while the bed level is held constant ($z_b = 0$), but the exchange layer is able to move up and down. The underlayers can be seen as bookkeeping layers and are inactive. Furthermore, the active layer has a vertically fixed layer thickness based on the zone that is considered to be mixed by waves in line Huisman et al. (2018) and Sloff and Mosselman (2012). This results in the following processes, during sedimentation the new sediment is mixed in proportionally in the active layer. Subsequently, a representative part of the active layer is mixed with the material in the exchange layer (green arrow fig. 3.8). The upper layer of the substratum (z_u) moves down during sedimentation (small blue arrow in fig. 3.8). When there is sufficient sedimentation a new layer will be created which results in the exchange layer to become an inactive underlayer. However, the opposite happens during sufficient erosion, sediments of the active layer are eroded leading to the sediment of the exchange layer moving up into the active layer while the upper layer of the substratum (z_u) moves up (small red arrow in fig. 3.8). When sufficient erosion occurs, the exchange layer erodes and the first underlayer becomes the new exchange layer.

3.3. Model calibration

Delft3D is a complex numerical model that solves multiple physical processes with feedback loops on large grids. Numerical models such as Delft3D often contain parameterizations as they are not able to solve all physics explicitly. Therefore, calibration of such a model to the local environment is considered essential. The delft3D model for the PHZD is calibrated through minimization of the error between the model output and the observational data of the SEDMEX field campaign. First of all, the calibration focuses on the minimization of the error of the water levels and velocity. These simulations only use the Delft3D-FLOW module, thus wave effects and sediment transport are not considered. Subsequently, the Delft3D-FLOW module is coupled to the Delft3D-WAVE module in order to calibrate the wave parameters.

3.3.1. Flow calibration

The water level and velocity are calibrated by varying the bottom friction which directly influences the flow. In Delft3D, the Chezy coefficient (eq. 2.11) represents the bottom friction and can be determined by several options. The first method is a direct computation of the Chezy coefficient as a function of the water depth and the total bed roughness (eq. 2.11). The total bed roughness is a function of the flow and therefore there is a feedback between the bed and the flow. Furthermore,

3.3. MODEL CALIBRATION

the Chezy coefficient can be a user-defined value which can be spatially constant or vary per grid cell. In addition, the Chezy coefficient can be computed with Mannings n (eq. 3.1).

$$C = \frac{\sqrt[6]{H}}{n} \quad (3.1)$$

where H is the water depth and n is the Manning coefficient. By using the user-defined Chezy coefficient and computation with the Manning coefficient (eliminating eq. 2.11), the flow does not depend on the total bed roughness (k_s). However, sediment transport still depends on the bed roughness as it is a function of the reference level (δ in eq. 2.24). Finally, the k_s can be given directly as input with the Coleman-Whitebrook method. Therefore, the bed does not affect sediment transport using this method, as the k_s is not computed. For the calibration, a low and a high value for the Coleman-Whitebrook, Mannings and user-defined Chezy methods are used. In addition, the user-defined Chezy parameter is spatially varied per cell or per grid based on the average depth (Table C.1).

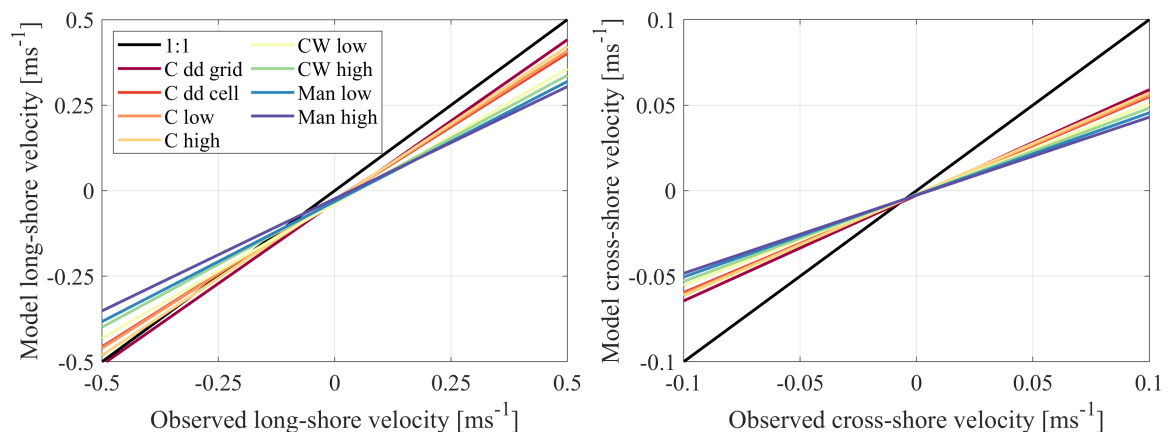


Figure 3.9.: The figure shows the fitted lines between the model and observed cross- and long-shore velocities. The different colours of the lines indicate the parameterization of that simulation.

The calibration shows that the water level is reproduced well for all of the roughness formulations, but the grid varying Chezy parameter performs best (figure C.1 & table C.3). Furthermore, the long-shore velocity is also well reproduced but shows larger deviations from the observations and between the models (figure C.2). In addition, the cross-shore velocity is less well reproduced, displaying a relatively large RMSE with respect to the magnitude (table C.3) and a large spread comparing the model to the observational data (figure C.3). Nevertheless, for the majority of the time, the magnitude is of the right order and the sign is correct. For both the cross- and the long-shore component, the model velocities are on average lower (figure 3.9). However, this is variable along-shore and is related to a time lag for some locations. The grid varying Chezy parameter

3.3. MODEL CALIBRATION

performs best considering water level, cross- and long-shore velocity (table C.3). Furthermore, Brakenhoff et al. (2020) suggested that the largest errors in sediment transport occur by removing the effect of the flow on bed roughness as this directly affects suspended sediment transport. In the formulation with a constant Chezy value, the bed roughness is still used for the calculation of the concentration.

3.3.2. Wave calibration method

The Delft3D-WAVE module is calibrated by varying several model parameters, boundary conditions and included processes. The base simulation is set up with the default parameter value for bottom friction, white capping formulation and stress formulation due to waves (Table C.4). Furthermore, waves are only locally generated by the wind and triad-triad interactions are not included. Each of the calibration simulations varies one of the parameters, including triad-triad interactions or the wave boundary condition imposed on the outer boundary opposed to locally generated waves (Table C.2). Finally, the time step and the coupling time between the FLOW and the WAVE module are varied to determine the model sensitivity.

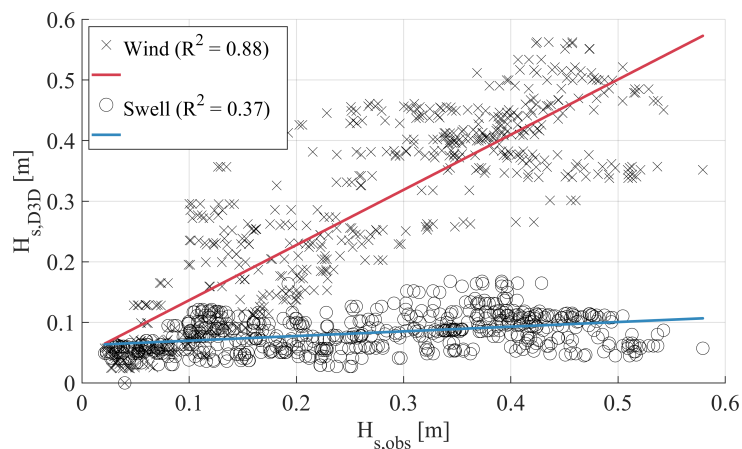


Figure 3.10.: The observed and modelled wave heights for the simulation with wind-generated waves and the simulation with swell waves.

The wave height is well reproduced when including local wind-generated waves opposed to the simulation with swell waves (figure 3.10). Furthermore, varying the other parameters and processes did not alter the modelled wave height and orbital velocity (figures C.5 & C.6). Therefore, the default parameters are used without swell waves forced on the boundaries and the generation of wind waves activated. In addition, the difference in wave height and orbital velocity is minimal for the three coupling times used (Table C.5). Furthermore, the simulation with half the time step shows nearly identical results compared to the original simulation. This is not only the case for the

wave height and orbital velocity, but cross- and long-shore velocity show a RMSE of 0.003 ms^{-1} .

3.4. Experimental design

The boundary conditions and included processes of the calibrated Delft3D model are systematically varied to assess the influence of the environmental conditions, graded sediments and bed composition. The subsequent section elaborates on the experimental design for each research question and the methods used in the analysis.

Research question 1

What is the relative importance of different drivers on the transport of sediment with a uniform grain size in a sheltered coastal environment, during a) calm weather conditions and b) storm conditions?

Several model simulations with uniform grain size, but varying environmental conditions are set up to isolate the effects of tidal currents, wind-driven currents, wind waves and swell waves (D simulations in table 3.4). For the astronomic water level simulation (D1), the hourly water level data is decomposed into separate tidal constituents using t-tide (Pawlowicz et al., 2002). Subsequently, the tidal constituents are used to reproduce the water level time series without the wind influence. In order to assess the role of different drivers, the sediment transport for simulations with only selective drivers (D1-4) is compared. In addition, simulations with synthetic wind conditions are set up to assess the influence of the wind velocity (D6) and direction (D7). The bed-shear stresses due to currents and waves are computed (eqs. 2.10 & 2.12) to evaluate the relative importance of currents and waves under varying environmental conditions (D6 & D7). Finally, in order to assess the role of the tide and wind-driven current, the current velocity is decomposed through harmonic analysis (Pawlowicz et al., 2002) into a tidal and residual current.

Research question 2

What is the effect of graded sediment and initial bed composition on sediment transport and the related erosion/deposition patterns in a sheltered coastal environment, during a) calm weather conditions and b) storm conditions?

First of all, the effect of the sediment mixture on sediment transport is assessed by simulating with a varying number of fractions and the fractions sizes under identical environmental conditions

3.4. EXPERIMENTAL DESIGN

(D6(10ms⁻¹) and GS simulations; table 3.2). Furthermore, the sediment mixture is examined with simulations GS4 and GS4B. Here the same number of sediment size fractions is chosen, but the sizes themselves differ. These fractions are chosen in such a way that the D_{50} of both mixtures is similar. The total sediment transport of each simulation is compared to assess the role of sediment size fractions on sediment transport. Furthermore, the exceedance of the critical bed-shear stress during calm and storm conditions (BC1 3ms⁻¹ and GS) for the different sediment fractions is examined.

Table 3.2.: Sediment fractions for the GS simulations

Simulation(s)	Sediment size fractions [μm]
D	300
GS2	300, 2000
GS4	125, 300, 850, 2000
GS4B	150, 400, 1000, 1600
GS6	125, 300, 500, 850, 1200, 2000
GS8	125, 200, 300, 500, 850, 1000, 1200, 2000

Second of all, simulations with a varying vertical bed composition are set up for both calm and storm conditions. The BC simulation consists of four pairs of model configurations with a different initial bed composition, each set consists of calm (wind = 3 ms⁻¹) and storm (wind = 10 ms⁻¹) conditions (table 3.4). The bed composition of BC1 (BC2) is made up of a uniform relatively fine (coarse) sediment mixture (table 3.3). Furthermore, the BC3 configuration represents the situation in which a coarse armour layer is present on top of a fine layer. On the contrary, BC4 simulates the opposite vertical composition in which a fine top layer is situated on top of a coarse substrate. For all of the BC simulations, the active layer is chosen at a constant thickness of 0.1m. Furthermore, the top layer in the non-uniform vertical layered simulations (BC3 & BC4) is of the same thickness as the active layer. The differences in the rate of sediment transport for the different initial bed compositions are analysed. Furthermore, the bed composition changes for the simulations with different vertical bed layering are examined. For each bed layer, a sediment size distribution curve is fitted to the modelled percentages of the sediment size fractions (figure ??). Both the fine and the coarse sediment mixture are initially poorly sorted (table 3.3)

The sensitivity of the model to the active layer thickness for different vertical layered bed compositions is examined. The combination of initial bed composition and the active layer thickness can influence the bed composition changes during the simulation. Furthermore, Huisman et al. (2018) indicated that the thickness of the active layer influences the rate of initial changes in D_{50} (Huisman et al., 2018). Therefore, the thickness of the active layer is varied between 0.05m and 0.2m for simulations BC2 and BC4.

3.4. EXPERIMENTAL DESIGN

Table 3.3.: The sediment composition for the fine and coarse sediment mixture, the values indicate the fraction present in the mixture, the D50 and the $\frac{D90}{D10}$

Sediment size fraction [μm]	Fine	Coarse
125	0.3	0.05
300	0.6	0.3
850	0.1	0.4
2000	0	0.25
D50 [μm]	183	516
D90/D10	3.8	11.3

Table 3.4.: Table showing the model study simulations performed to identify the effect of different drivers and processes on sediment transport

Simulation	Boundary conditions	Wind growth	Bed composition	Period	Sediment fractions	Multilayer bed
D1	Astronomic water level	No	Uniform	2	1	No
D2	Water level, wind	No	Uniform	2	1	No
D3	Water level, wind	Yes	Uniform	2	1	No
D4	Water level, swell waves	No	Uniform	2	1	No
D5	Water level, SSW wind: 15 ms^{-1}	Yes	Uniform	1	1	No
D6	Water level, SSW wind: 5, 10, 15, 20 ms^{-1}	Yes	Uniform	2	1	No
D7	Water level SSE/S/E wind: 15 ms^{-1}	Yes	Uniform	2	1	No
GS2	Water level SSW wind: 10 ms^{-1}	Yes	Uniform	2	2	No
GS4	Water level SSW wind: 10 ms^{-1}	Yes	Uniform	2	4	No
GS4B	Water level SSW wind: 10 ms^{-1}	Yes	Uniform	2	4*	No
GS6	Water level SSW wind: 10 ms^{-1}	Yes	Uniform	2	6	No
BC1	Water level SSW wind: 3/10 ms^{-1}	Yes	Uniform fine	2	4	Yes
BC2	Water level SSW wind: 3/10 ms^{-1}	Yes	Uniform coarse	2	4	Yes
BC3	Water level SSW wind: 3/10 ms^{-1}	Yes	Fine layer on top of coarse	2	4	Yes
BC4	Water level SSW wind: 3/10 ms^{-1}	Yes	Coarse layer on top of fine	2	4	Yes

4. Model results

The following section will show the model results for the sediment transport along the PHZD. The vector data of the model results is rotated to align with the PHZD, resulting in a long- and cross-shore component (figure 4.1). For the long-shore component, the positive axis is to the northeast (flood direction) and for the cross-shore component, the positive axis is to the southwest (offshore direction; figure 4.1). Furthermore, several long-shore locations are used to analyse the model results in more detail corresponding to the location of the measurements of the SEDMEX field campaign (L1-L6).

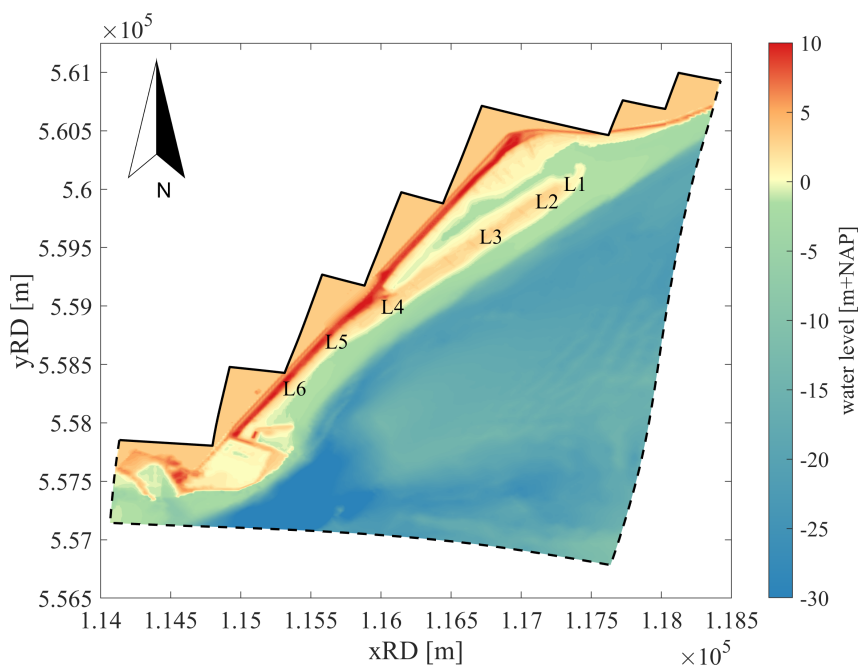


Figure 4.1.: The bathymetry of the inner model domain of the PZDH area with the 6 long-shore locations is indicated. The dashed lines indicate the domain decomposition boundaries with the middle model domain. The arrows indicate the direction of the long- and cross-shore axis.

4.1. Drivers

4.1.1. The relative importance of wind, waves and tides on uniform sediment transport

The relative importance of wind, waves and tides on sediment transport is assessed by comparing the simulations that isolate the effect of the astronomical tide (D1), the wind effect on the tide (D2), wind waves (D3) and swell waves (D4). First of all, the sediment transport at a single location (L2 at $z = 1.54\text{m}$) is examined for simulations D1 to D4. The sediment transport does not change significantly when the wind effect is included, while the magnitude of transport increases, the direction does not change (astronomical to tides transport rose in figure 4.2). The bed-load is in the long-shore direction with a slightly larger transport in the northeast (flood) direction (figure 4.2). In addition, the suspended transport is relatively small and in the north-northeast (onshore-flood) direction. Furthermore, wind waves significantly alter the magnitude and direction of sediment transport while swell waves only result in a marginal increase in magnitude (wind wave and swell wave roses in figure 4.2). This is in line with the results of the calibration, which showed that swell waves do not reach wave heights larger than 0.1 m at the beach of the PHZD (figure 3.10). Therefore, the subsequent section will focus on the differences in sediment transport between the simulation with (D3) and without (D2) wind waves.

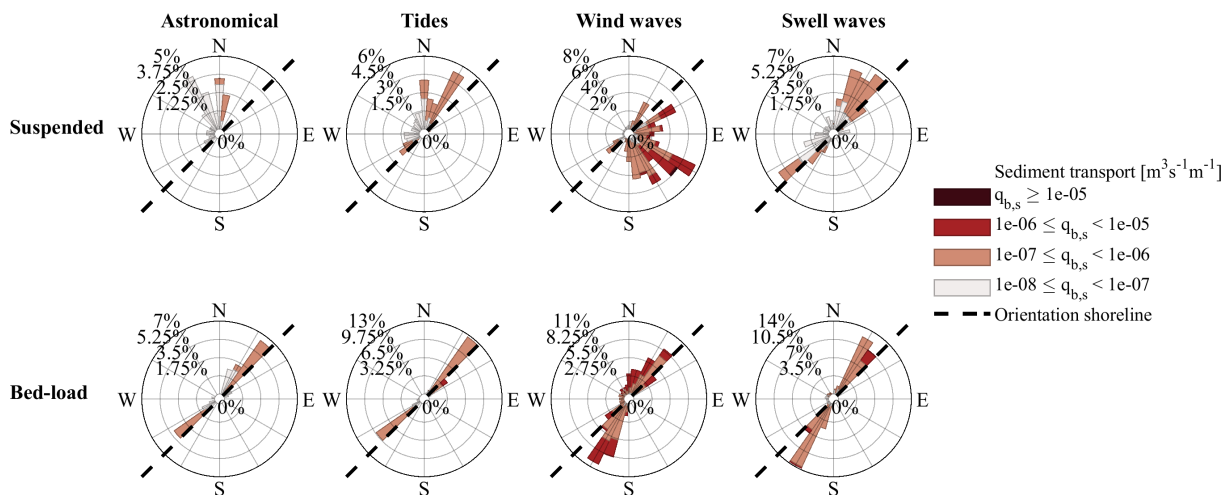


Figure 4.2.: Bed-load and suspended sediment transport roses of L2 for the simulations with varying processes driving the sediment transport (D1-D4). The radial axis indicates the direction and frequency of occurrence while the colors indicate the magnitude of sediment transport. A step in colour intensity indicates an order of magnitude increase in sediment transport.

Both the mean suspended and bed-load transport is roughly parallel to the shoreline, in the flood direction for the centre of the PHZD (left panels in figure 4.3). The transport magnitude is largest

4.1. DRIVERS

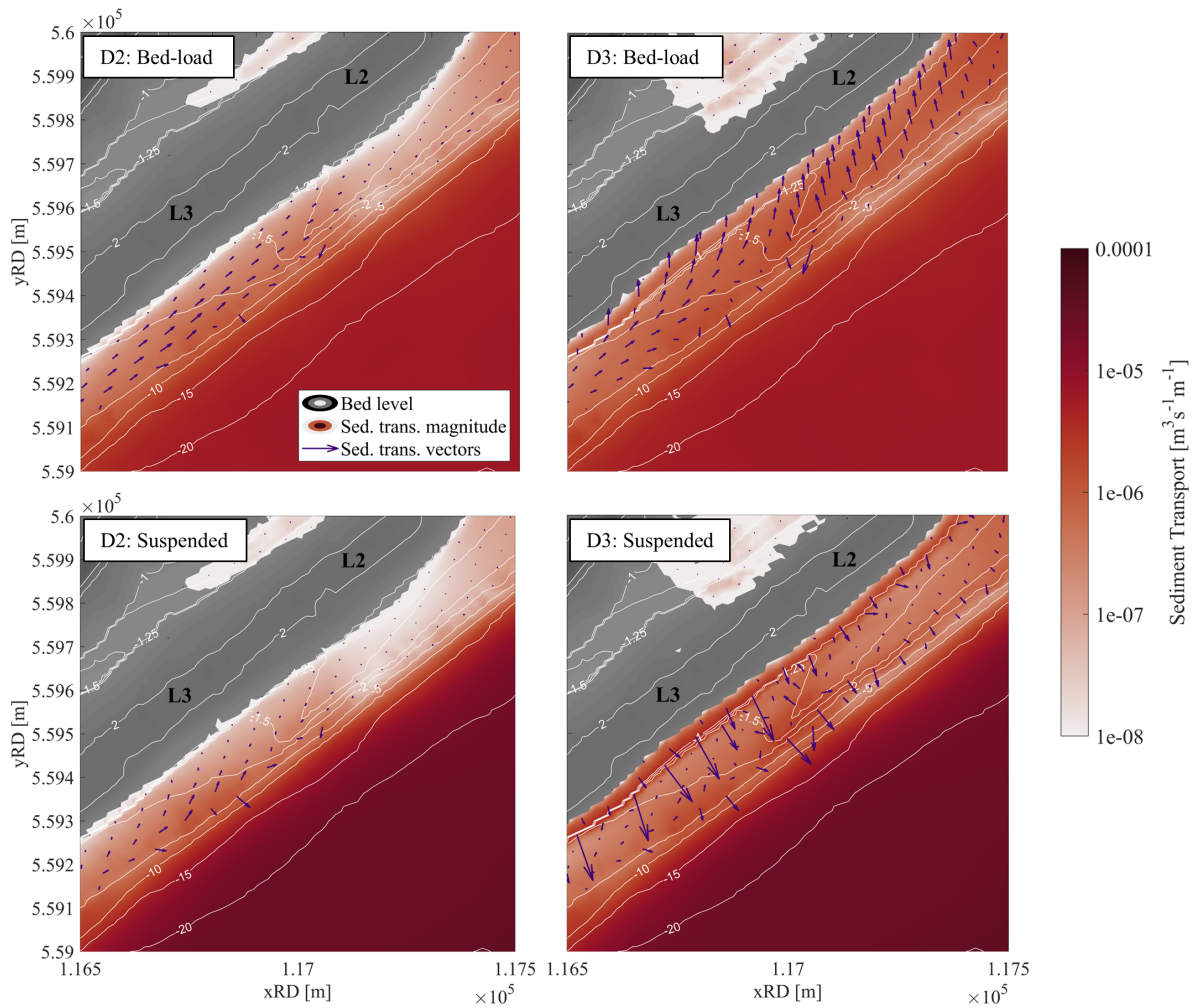


Figure 4.3.: The mean suspended (lower) and bed-load (upper) transport for the simulation with (D3; right) and without (D:left) wind waves for the spit of the PHZD. The grey shades indicate the bed level, the red shades the sediment transport magnitude on a log scale and the arrows indicate the sediment transport vector.

in the deeper channel and decreases several orders of magnitude towards the beach. The mean transport in the flood direction is the result of a flood-dominant tidal asymmetry in the peak velocity (see section 2.4.1). During the flood phase, the velocities are higher than during the ebb phase (for L2 are on average 0.051 ms^{-1} in figure 4.5). The bed-shear stresses are larger as a result of the higher velocities during the flood phase ($\tau \propto u^3$; figure A.4), leading to a mean suspended and bed-load transport. However, the mean sediment transport decreases and reverses towards the ebb direction at L5 and L6 (left panels in figure 4.4). The difference in hydrodynamics for the sheltered beach (L5 and L6) is also seen in the long- and cross-shore currents and bed-shear stresses near

4.1. DRIVERS

the NIOZ harbour (L6 in figure A.4).

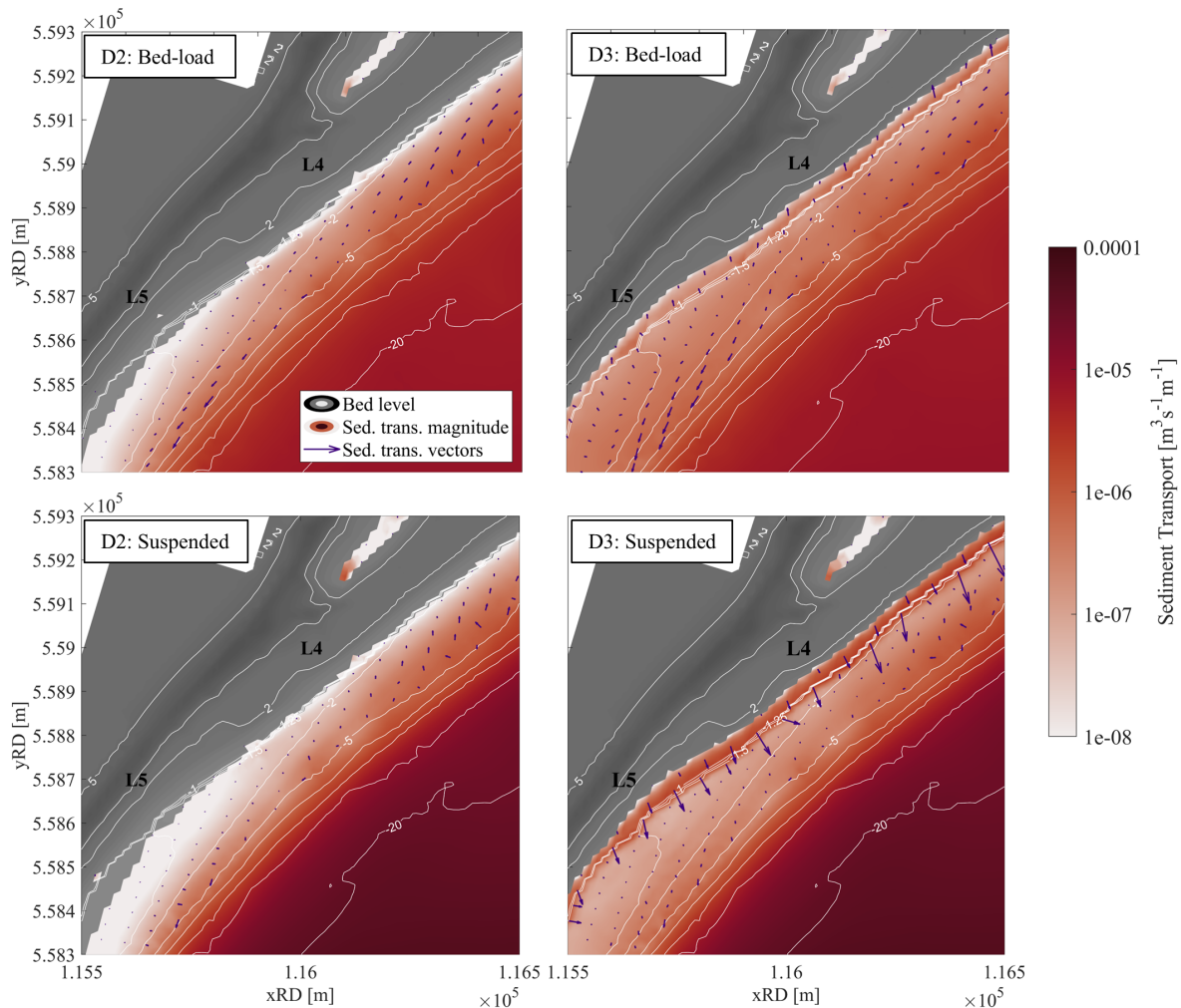


Figure 4.4.: The mean suspended (lower) and bed-load (upper) transport for the simulation with (D3; right) and without (D:left) wind waves for the centre and sheltered area of the PHZD. The grey shades indicate the bed level, the red shades the sediment transport magnitude on a log scale and the arrows indicate the sediment transport vector.

Along the entire dike the wind-generated waves substantially increase the magnitude of the suspended and bed-load transport, especially at the beach face (figure 4.3 & 4.4). The increase in magnitude is the result of an increase in the maximum bed stress due to the wave orbital motion, resulting in a higher entertainment rate of sediment (figure 4.6). This is illustrated by the correlation between the orbital velocity, the maximum bed-shear stress and the concentration for the simulation with wind waves (blue lines in the figure 4.6). For the simulation with only tides, the concentration is more than 2 orders of magnitude lower and correlated to the highest velocities. In

4.1. DRIVERS

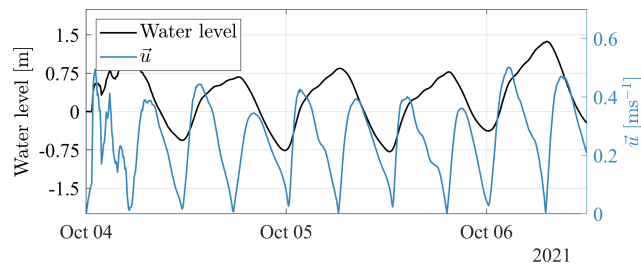


Figure 4.5.: The water level and current velocity magnitude for the tides only simulation (D2).

addition, the mean bed stress (wave and current combined) does not change significantly due to the effect of waves (middle panel in figure 4.6). For the simulation with only tides, the maximum bed shear stress is roughly equal to the mean bed-shear stress.

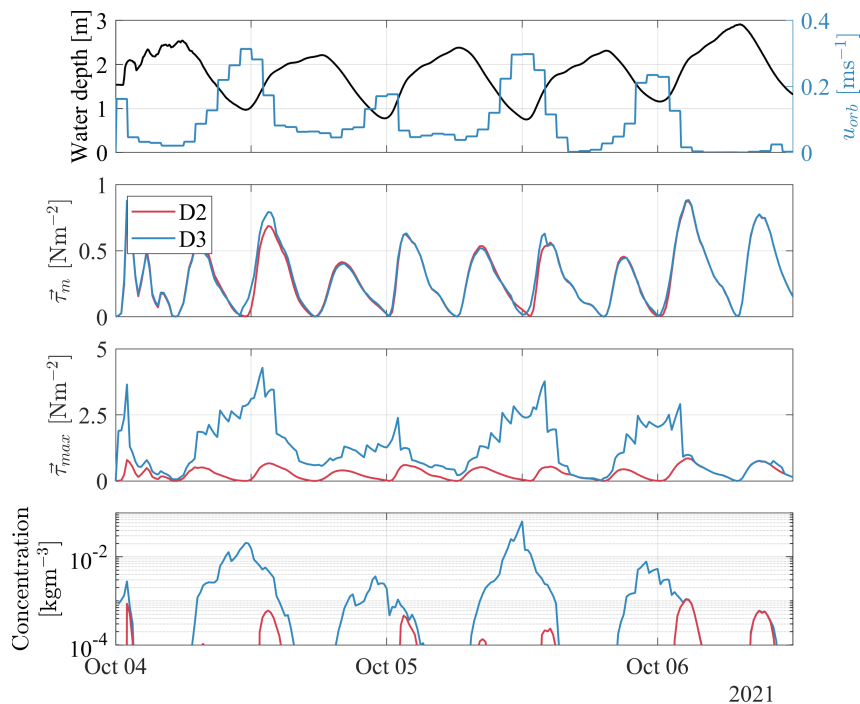


Figure 4.6.: The change of mean and maximum bed shear stress is related to the water level and orbital velocity. The water level and orbital velocity are shown in the upper panel. The second panel shows the current-related bed-shear stress and the third panel shows the maximum bed shear stress. In the lower panel, the concentration is shown for both simulations on a log scale to visualize both simulations.

The mean suspended sediment transport at the beach is in the off-shore direction (figure 4.3 & 4.4) as a result of high concentrations during off-shore directed currents (figure 4.7). As indicated before, the high concentrations are the result of the wave orbital velocity near the bottom which is

4.1. DRIVERS

largest during low water (upper panel in figure 4.6). In addition, high concentrations coincide with relatively low long-shore and relatively high cross-shore current velocities (figure 4.7). As this is not the case for the simulation without waves, it is an indication that the relatively high cross-shore current is not tide-driven, but wave-driven. Along the entire PHZD, a similar change in pattern is observed, but the magnitude decreases towards the sheltered beach (L5 and L6) and towards the northeastern most point of the spit (figure 4.3 & 4.4). The larger suspended sediment transport at the beach is located at the area where the plateau in front of the PHZD is of greater depth (area between L4 and L3).

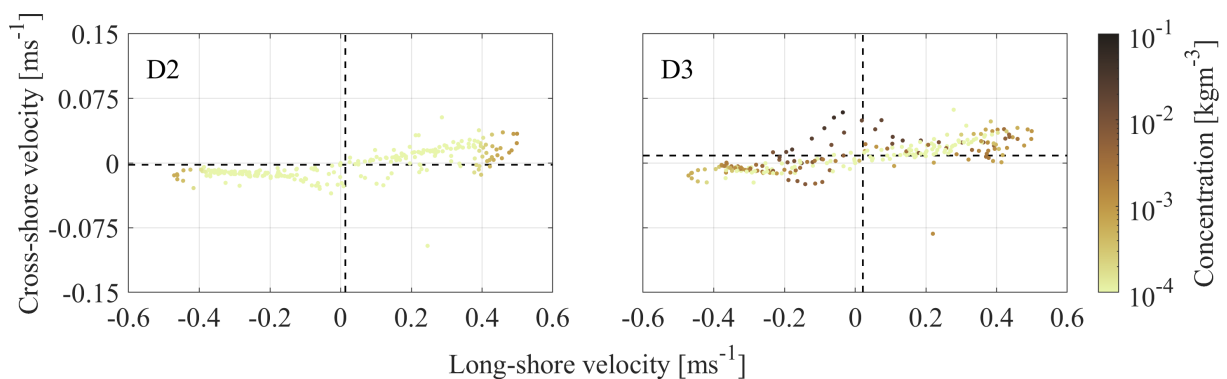


Figure 4.7.: Scatter plot of the long- and cross-shore velocity of L2 for the simulation with (D3) and without (D2) wind waves. The colours indicate the concentration on a log scale.

In contrast to the suspended sediment transport, the mean bed-load transport is onshore directed at shallower depths ($z > -1.5\text{m}$) and in the flood direction at greater water depths (figure 4.3). Similar to the suspended transport, the magnitude decreases towards the sheltered beach (figure 4.4). In deeper water ($z < -1.5\text{m}$), the bed-load transport is relatively unaffected by waves as it is in the same direction as the simulation without wind waves (figure 4.3). However, the orbital motion near the bottom is increasing with decreasing water depth and is relatively high at the areas with onshore transport (left panel in figure 4.8). In these areas the wave shape, and thus the orbital motion, is affected by the bed resulting in skewed waves (green shades in the right panel in figure 4.8). In addition, the onshore bed-load transport (left panel in figure 4.8) is in the same direction as the wave propagation (right panel in figure 4.8). The waves travel in the same direction as the wind (north northeast), but refract towards the beach in shallower water. And thus, the onshore-directed transport at shallower water depths is the result of the skewed orbital motion near the bed.

4.1. DRIVERS

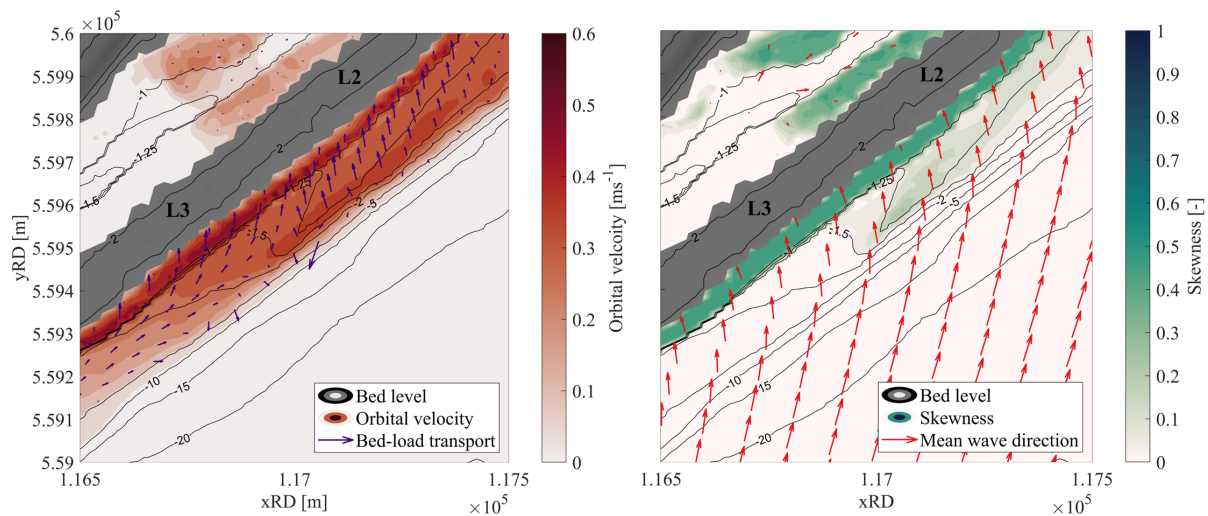


Figure 4.8.: The bed-load transport in relation to the wave direction and skewness for simulation D3. The left panel shows the mean peak near-bed orbital velocity (red shades) and the bed-load transport (purple vectors) for the centre of the spit at the PHZD. In the right panel, the skewness (green shades) and the direction of wave propagation (orange vectors) are shown for the same area.

4.1.2. Sediment transport under varying wind velocity and direction

In the following section, the effects of the wind velocity and direction are discussed by analysing the sediment transport of the simulations with synthetic wind conditions (D6 & D7). With increasing wind velocity, the bed load transport is amplified towards the north northeast, the direction of the wave propagation (lower roses in figure 4.9). The increase in bed-load transport is the result of larger waves (right panel in figure 4.10) and higher orbital velocities (left panel in figure A.11). In addition, the wave shape is transformed to a skewed shape at larger depths due to the increase in wave height (right panel in figure A.11). As a result, the wave-induced bed-load transport occurs at larger depths (figure A.10)

Furthermore, the suspended transport is mainly in the offshore direction for moderate energetic conditions (10ms^{-1} , upper left two roses in figure 4.9). However, with further increasing wind speeds, the suspended sediment transport intensified and rotates towards the flood direction (10ms^{-1} , upper right two roses in figure 4.9). The change in suspended transport is the result of an increasing residual current. As the wind velocity increases relatively large flood directed, and a smaller offshore-directed, residual current arise (left panel in figure 4.10). The residual current in both directions increases faster than linear with increasing wind velocities.

The Shields parameter shifts towards higher wave-related bed shear stress for wind velocities between 5 to 15ms^{-1} (figure 4.11). However, from 10 to 20ms^{-1} , the residual current increases

4.1. DRIVERS

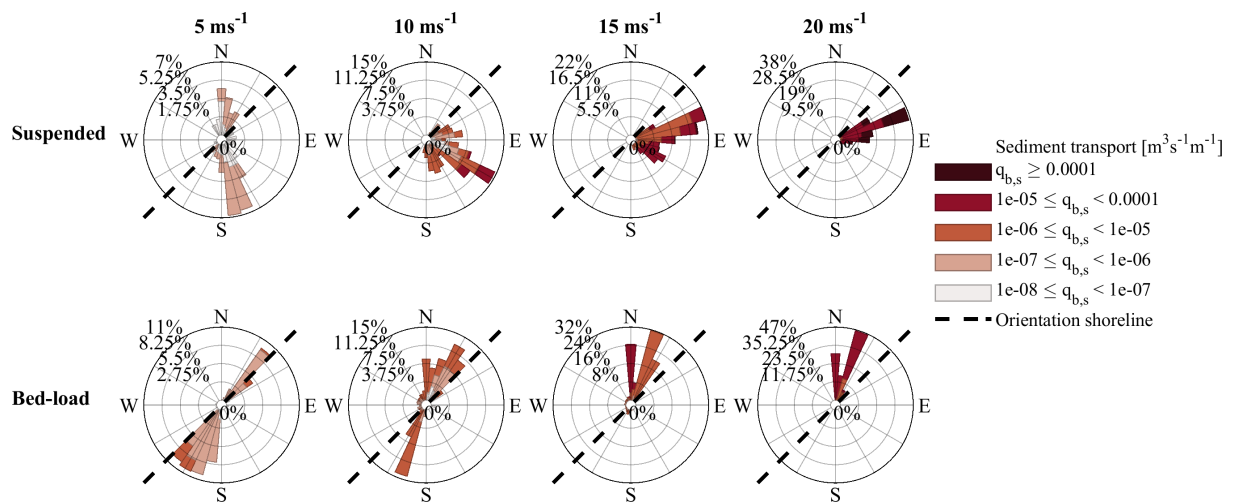


Figure 4.9.: Bed-load and suspended sediment transport roses for the simulations with increasing wind velocity (D6). The radial axis indicates the direction and frequency of occurrence while the colours indicate the magnitude of sediment transport. A step in colour intensity indicates an order of magnitude increase in sediment transport.

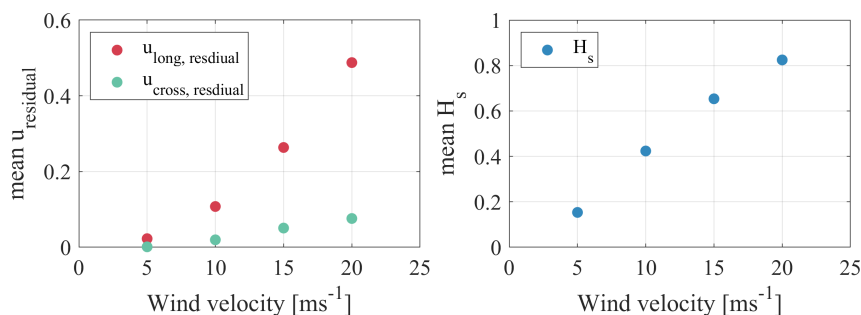


Figure 4.10.: The residual long-shore wind-driven current and the wave height as a function of forced wind velocity. The decomposed current velocities of the harmonic analysis can be found in figure A.7.

substantially leading to an increase in the current-related bed shear stress. Therefore, the system first shifts towards a wave-only situation for moderate energetic conditions. During these conditions the residual current is small and the wave motion dominates the bed-shear stresses. However, with further increasing wind velocity the system moves more towards a mixed-energy environment as a result of the increasing residual currents.

Finally, the results of varying wind directions are presented. As discussed above, the bed-load transport is wave-driven and thus the direction rotates jointly with the wind direction (figure A.12). For the suspended transport the changes are less uniform. For the deeper areas, the sediment transport is mainly in the offshore direction for all wind directions. Furthermore, the largest suspended

4.1. DRIVERS

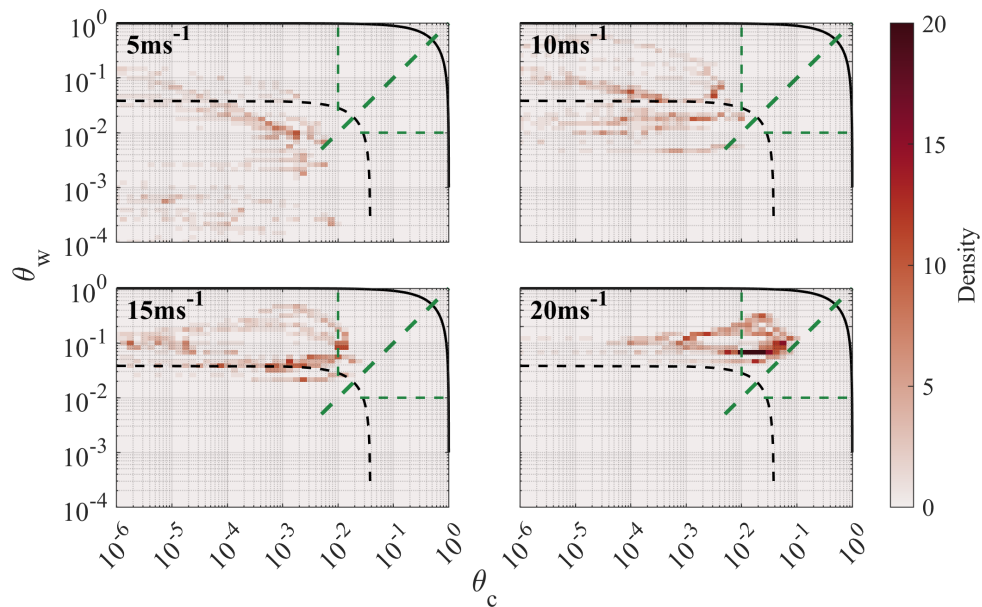


Figure 4.11.: The x-axis shows the current related Shields bed shear stress (θ_c) and the y-axis, the wave-related Shields parameter (θ_w). The colours indicate the density of the output of the simulation for each of the wind velocities. The dotted black line shows the threshold for incipient motion for the 300 μm sediment fractions and the solid black line indicates the sheet flow threshold. Furthermore, the thick dotted green line indicates the separation between wave/tide-dominated and the thin dotted green lines the separation between a mixed or a wave/tide only environment.

sediment is at the large bed-level gradients and is offshore directed. However, the suspended sediment transport in the shallower areas, where waves interact with the bed, varies with the wind direction. The suspended transport is in the flood direction for the winds from the SSS and S, onshore directed for the SSE wind direction and in the ebb direction for the E wind (figure A.13). In addition, the mean wave height does not differ significantly with changing wind direction (right panel in figure 4.12). However, the residual current is strongest when the wind direction is in the same orientation (south-southwest) as the PHZD (left panel in figure 4.12). The residual current is in the flood direction for winds from the south-southwest to the south southeast and in the ebb direction for winds coming from the east.

4.2. GRADED SEDIMENT

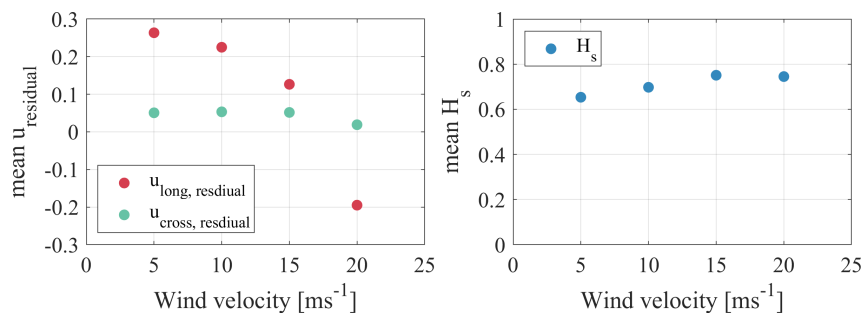


Figure 4.12.: The residual long-shore wind-driven current and the wave height as a function of forced wind direction.

4.2. Graded sediment

4.2.1. The effect of graded sediment on sediment transport

In the next section, fractional sediment transport and the influence of the sediment mixture on sediment transport are examined. First of all, during moderate energetic storm conditions (wind velocity is 10ms^{-1}) all sediment fractions are mobilized. Nevertheless, the smaller the particle the more frequently the incipient motion threshold is surpassed (figure 4.13;table 4.1). A similar pattern for the sediment fractions is seen for calm conditions, but with less exceedance of the threshold for incipient motion. However, this pattern changes when the hiding and exposure mechanism for incipient motion is taken into account. As a result, the threshold for incipient motion is exceeded nearly equal amount of times for all sediment size fractions (values in brackets table 4.1). However, the coarse sand fractions (300 & 850 μm) show a slightly higher exceedance rate. For all cases, the conditions at the bed are around the threshold for incipient motion. In addition to the environmental conditions, the water depth also influences the bed shear stress and thus the possibility for mobilization. Generally, the bed shear stress is higher at shallower water depths, with the largest bed-shear stress due to waves at $z = -1.2$ and the highest bed-shear stress due to currents at $z = 0.25$ (figure A.14).

Table 4.1.: The number of times the incipient motion threshold is exceeded for the four sediment fractions of GS4. The value in between brackets indicates the number for the case with the hiding and exposure correction.

Sediment fraction	Calm	Storm
125 μm	70 (37)	184 (93)
300 μm	58 (44)	171 (119)
850 μm	44 (44)	119 (120)
2000 μm	32 (37)	77 (97)

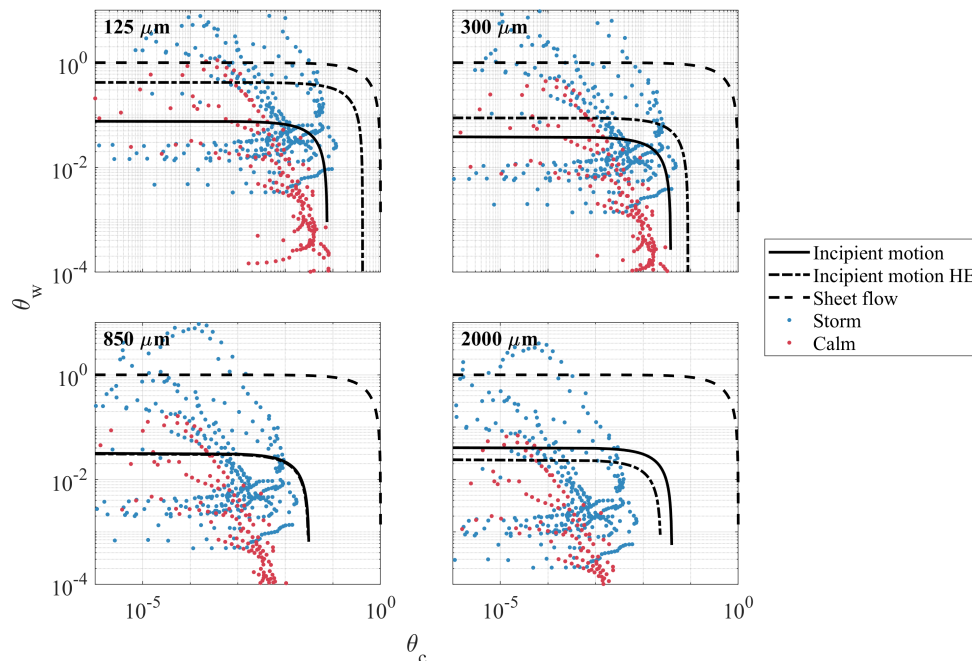


Figure 4.13.: The wave- and current-related bed shear stresses plotted against each other for different water depths. The four plots show the four sediment fractions used in the GS4 simulation. Furthermore, the incipient motion threshold and sheet flow regime are indicated

The total sediment transport differs significantly for the simulations with varying sediment mixture (figure 4.14). The difference in sediment mixture results in the largest variability in the suspended sediment transport while the bed-load component indicates smaller differences. For suspended sediment transport increasing the number of sediment fractions leads to a higher transport rate, except for the bimodal mixture. However, the simulations with 4, 6 or 8 fractions also include a relatively small fraction (125 or 150 μm) while the bimodal mixture does not (the smallest size is 300 μm). The bimodal mixture only consists of 2 sediment fractions, therefore half of the bed is made up of the gravel fraction ($D_{50} = 2000\mu\text{m}$).

Furthermore, with an increasing number of fractions the suspended sediment transport rate converges to a rate of approximately 1.09 times the rate of a single fraction (left panel in figure 4.15). For the bed-load transport, all multiple sediment fraction simulations lead to a smaller sediment transport, except for the 4 fraction mixture (GS4). However, the number of fractions has a limited effect on the bed-load transport rate. In addition, the root mean square deviation of the suspended transport rate is significantly larger compared to the bed-load transport rate. Next to this, the two simulations with 4 sediment fractions and a similar mean D_{50} , but different sediment sizes, also exhibit a relatively large difference. Therefore, the sediment fractions chosen for the mixture have a significant impact on total sediment transport.

4.2. GRADED SEDIMENT

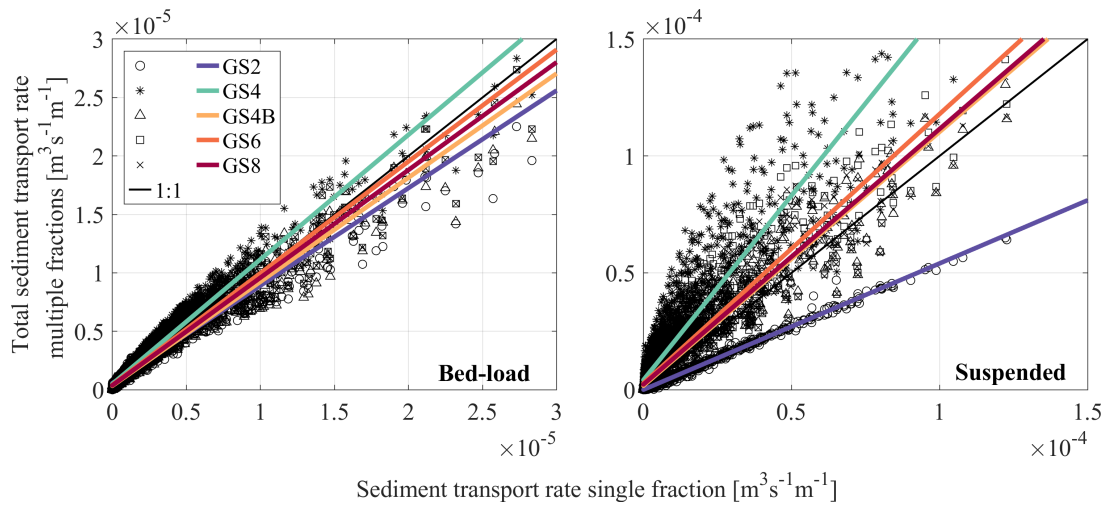


Figure 4.14.: Total suspended and bed-load sediment transport for the simulations with different sediment mixtures compared to the simulation with a single fraction.

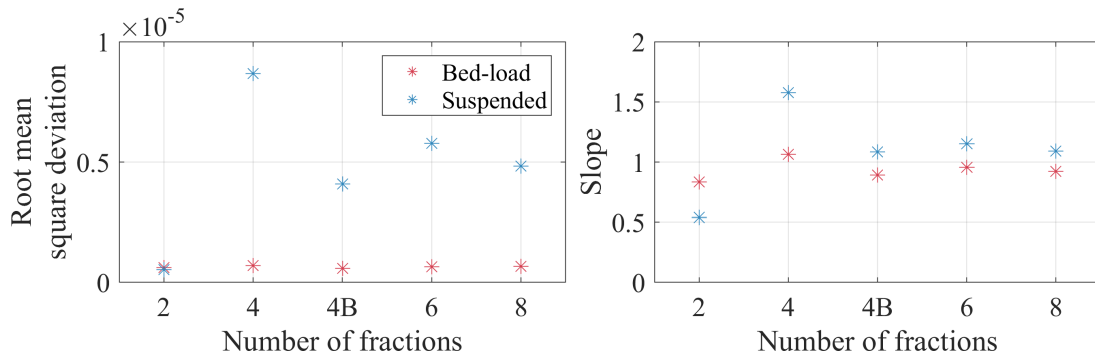


Figure 4.15.: The root mean square deviation and the slope of the fitted lines for the multiple sediment fractions.

The sediment transport roses for the different sediment fractions show a large difference in magnitude for the suspended sediment transport (figure 4.16). Even though the threshold for incipient motion is exceeded a similar amount of times with the HE effect taken into account (figure 4.13), the smaller fractions have a larger suspended sediment transport rate. Therefore, the difference in sediment transport must be related to sediment unable to settle, remaining in suspension or suspended sediment transport from adjacent cells. Furthermore, the 2000 μm fraction does not show any sediment transport. The bed-load transport shows fewer changes in magnitude and direction (lower right rose in figure 4.16).

4.2. GRADED SEDIMENT

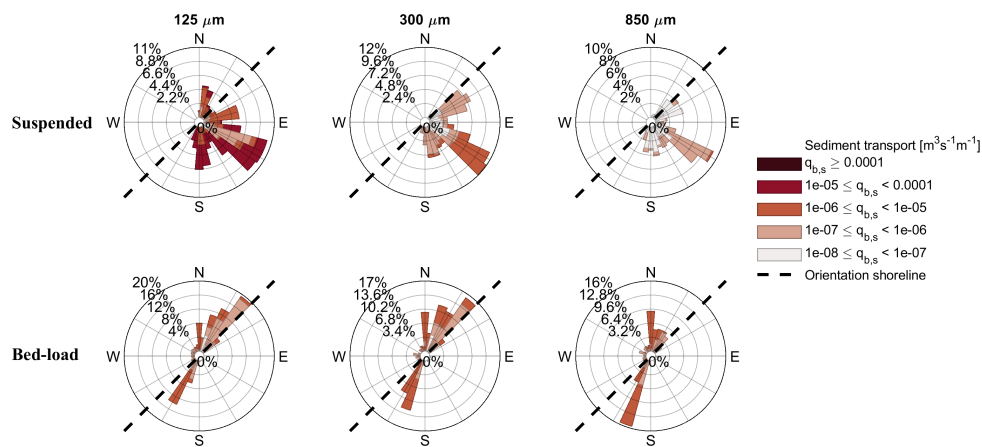


Figure 4.16.: Total suspended and bed-load sediment transport for the simulations with different sediment mixtures compared to the simulation with a single fraction.

4.2.2. Importance of initial bed composition on initial erosion/deposition patterns

In the final section of the results, the influence of the initial bed composition on initial erosion and deposition patterns is analysed. The results shown in this section will focus on the beach face in the cross- and long-shore direction. Therefore, along the dike the first four grid cells covering the beach face between 1m and -2m bed elevation are selected (figure A.15). First of all, the sediment transport rate between no, a fine and a coarse initial bed composition for moderate storm conditions are compared for a single cross-section. For each of the simulations, the largest suspended and bed-load transport rate occurs between 0 and -1m bed elevation (figure ??). The bed-load transport rate is largest for the simulation without a bed stratigraphy followed by the fine and subsequently the coarse initial bed. Furthermore, the bed-load transport rate for the fine and coarse initial bed composition differs significantly for the first 12 hours but are comparable for the rest of the simulation.

Similar to the bed-load component, the suspended transport rate is largest for the simulation without an initial bed composition, except for the first 12 hours where the fine initial bed has the highest transport rate (figure ??). Compared to the bed-load transport rate, the difference in suspended transport between fine and coarse initial bed composition remains relatively large throughout the simulation. Finally, the pattern of this cross-section is similar along the entire dune (figure A.17 & A.16). Furthermore, during calm conditions (wind velocity is 3 ms^{-1}), the largest sediment transport rates are found at greater water depths (figure 4.18). For both the suspended and bed-load the transport rate is largest for the simulation with the fine initial bed composition. However, the sediment transport rates are much lower compared to the stormy conditions (the colour scale is an order of magnitude lower compared to figure ??). In contrast to the storm

4.2. GRADED SEDIMENT

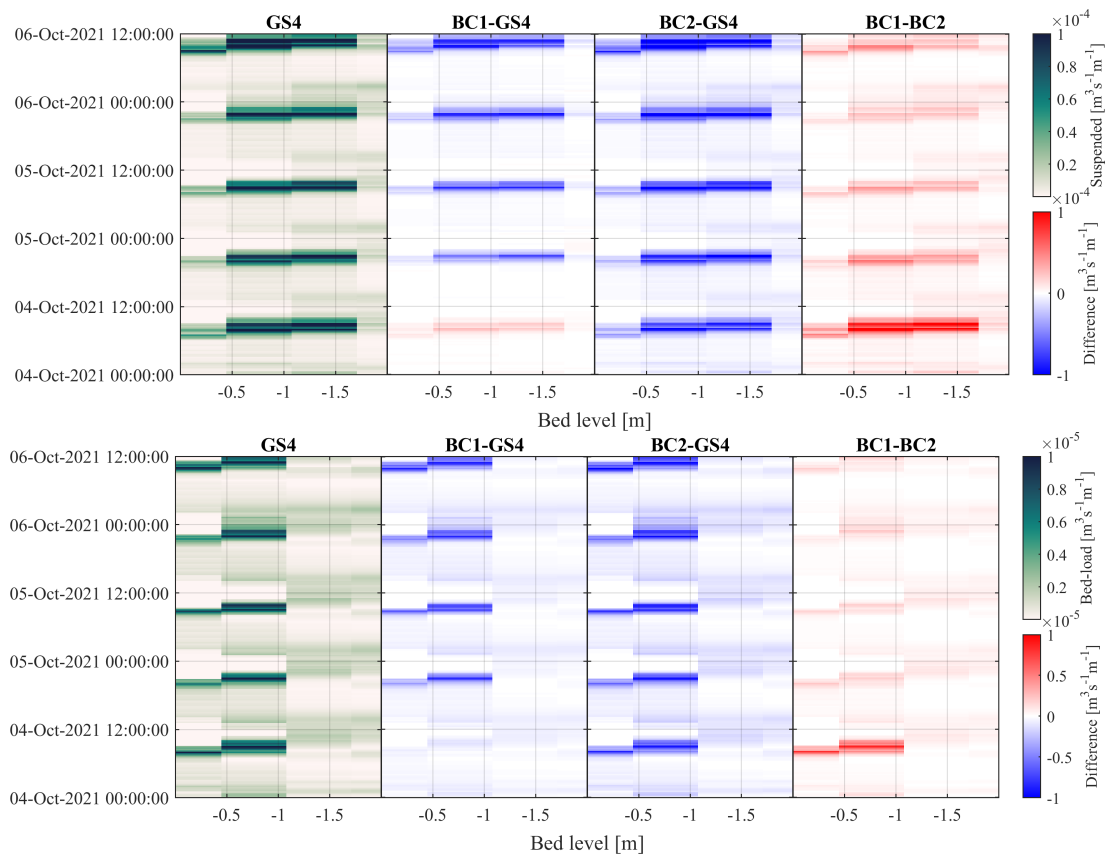


Figure 4.17.: The suspended (upper) and bed-load (lower) sediment transport rate for the L2 cross-section for the simulations with no bed stratigraphy (GS4), the difference with the fine initial bed composition (BC1-GS4), the coarse initial bed composition (BC2-GS4) and the difference between the fine and coarse bed composition (BC1-BC2).

conditions, the difference in sediment transport increases over time during calm conditions.

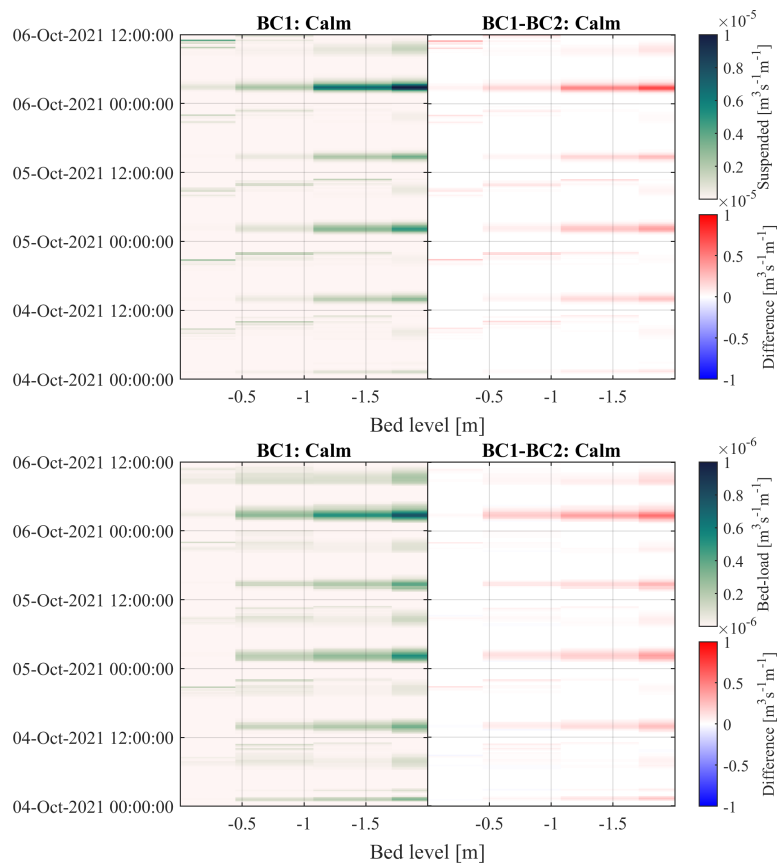


Figure 4.18.: Suspended (upper) and bed-load (lower) transport rate for the BC1 simulation during calm conditions for a single cross-section of the beach face (left). The difference in the bed-load transport rate between the BC1 (fine) and BC2 (coarse) simulation during calm conditions. Here positive values indicate a larger suspended transport rate for the BC1 simulation.

4.2. GRADED SEDIMENT

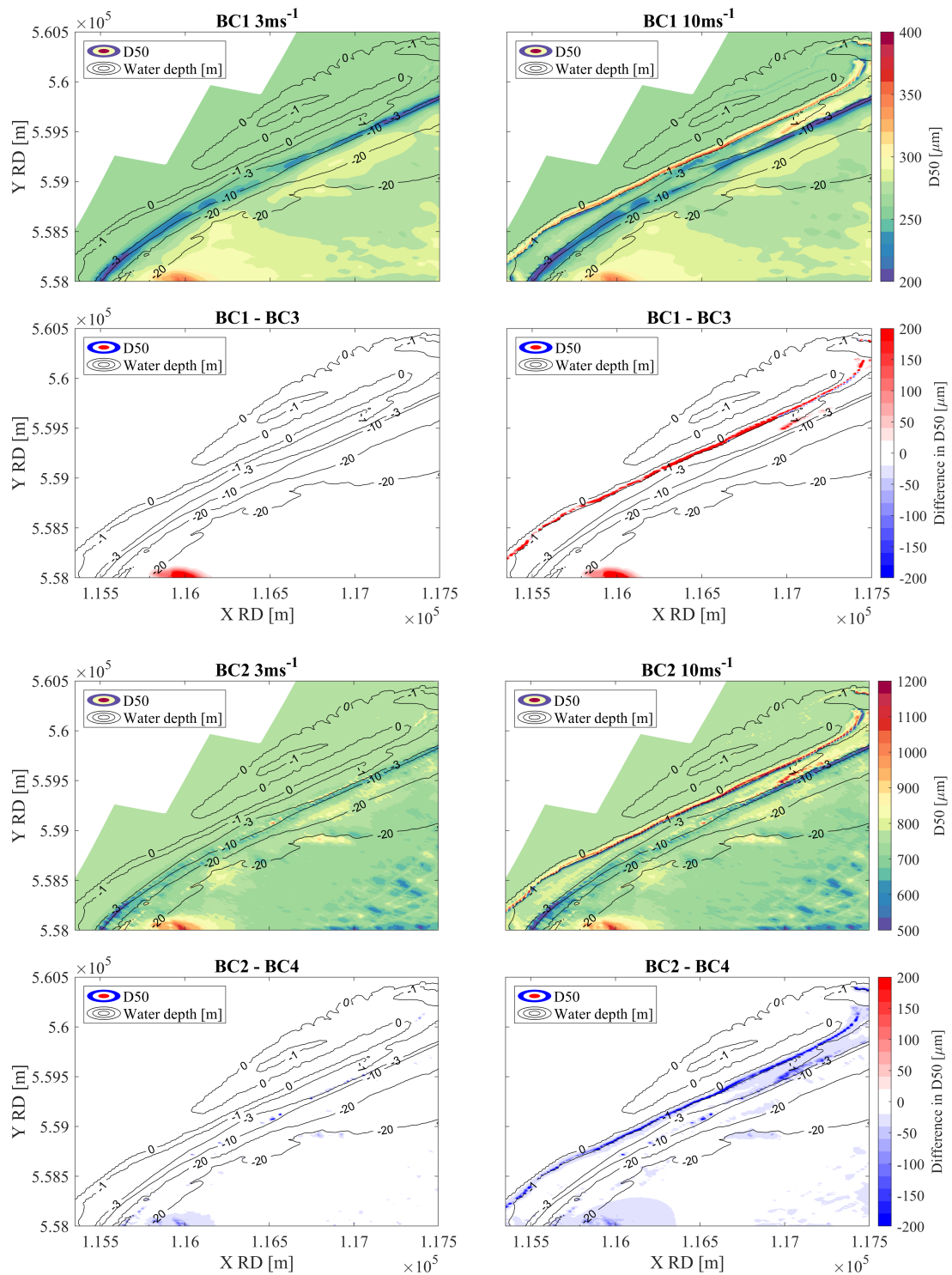


Figure 4.19.: Map of the D50 changes of the PHZD for the fine and coarse initial bed composition simulations for both calm and storm conditions. The upper two panels show the D50 at the end of the simulation for the calm (left) and storm conditions (right). The lower two panels show the difference with the vertically layered simulation (fine on top of coarse) where red indicates a coarse bed and blue a finer bed for the vertically layered simulation.

4.2. GRADED SEDIMENT

During calm conditions (wind velocity is 3 ms^{-1}) the bed composition shows no change at the beach face for both the fine and the coarse bed composition (figure 4.19). However, during moderate energetic conditions, the upper beach face becomes coarser while the lower bed becomes finer for the simulations with a vertically uniform composition (figure 4.19). This pattern is uniform along the dune, but the magnitude of change is largest in the centre of the dune.

The initial vertical bed stratigraphy greatly influences the changes in bed composition at the beach face (figure 4.19). If a fine layer is located on top of a coarse layer, the bed will become more coarse at locations of erosion compared to a uniform fine layer (BC3-BC1; 4.19). The opposite happens if a coarse layer is situated on top of a fine substrate, here the bed becomes finer compared to the uniform coarse bed composition (BC4-BC2; figure 4.19).

In the final section of the results, the bed level and bed composition changes for fine on coarse (BC3) and coarse on fine (BC4) initial bed composition with bed level updating. First of all, the erosion and deposition pattern is similar for both simulations, with erosion at the beach face and sedimentation at the foot of the beach face (figure 4.21). Along the whole PHZD, the largest erosion is at the locations with a large slope and sedimentation at the foot of the slope (left and middle figure 4.20). Furthermore, the coarse upper layer leads to less erosion than the fine upper layer, but the differences are relatively small

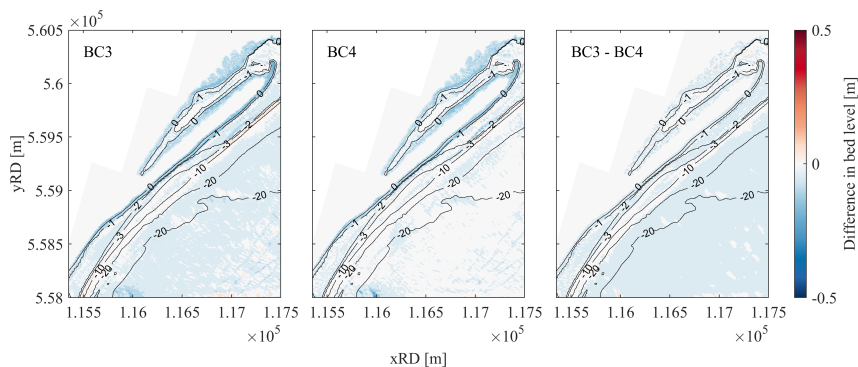


Figure 4.20.: The bed level changes for the simulation BC3 (left) and BC4 (middle) where blue indicates erosion and red sedimentation. The right figure indicates the difference between BC3-BC4 with blue (red) indicating lower (higher) bed level for simulation BC4

For the case of a fine top layer, erosion leads to a coarsening of the bed while sedimentation leads to no changes in bed composition (figure 4.21). The coarsening is the result of selective transport of the finer fractions ($D_{50} = 125 \text{ and } 300 \mu\text{m}$) and the subsequent inflow of coarse fractions from the under layer (4.22). Furthermore, the unchanged bed composition in the grid cell with sedimentation appears to be the result of an inflow of sediment similar to the initial bed composition (figure 4.22).

4.2. GRADED SEDIMENT

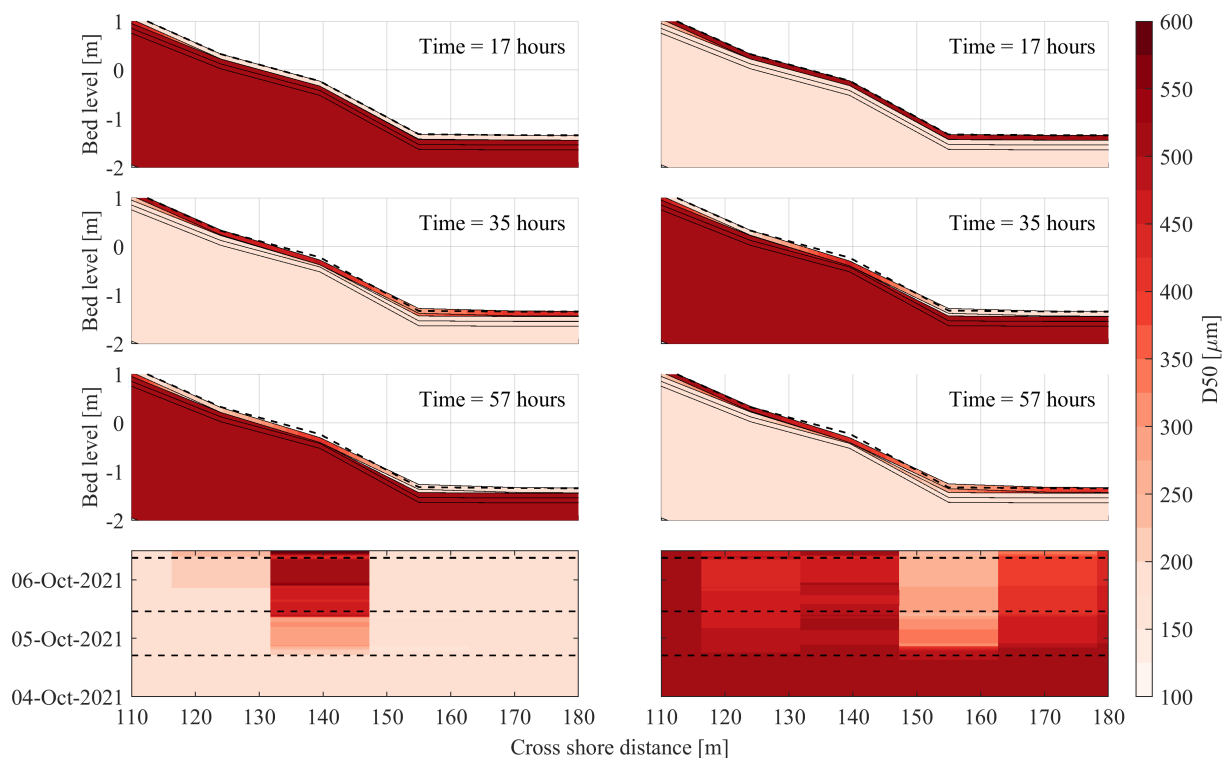


Figure 4.21.: The bed level and bed composition changes at the L2 cross-section for the BC3 (fine on the coarse, left panel) and the BC4 (coarse on fine, right panel) simulation with bed updating. The upper three panels show the cross-section for different moments in time. Here the colours indicate the D50 and the dashed line the initial bed level. The lower panel shows the D50 changes of the top layer over time (y-axis) where the dashed line indicates the moments in time of the cross-sections in the upper three panels.

For the case of a coarse top layer, erosion leads to a slightly finer bed composition while the sedimentation greatly decreases the D50 (lower panel figure 4.21). The slight fining of the bed for the location with erosion is the result of selective transport of the finer fractions ($D50 = 125$ and $300\mu\text{m}$), but these are replenished from the fine under layer (figure 4.22). Furthermore, the fining of the bed composition in the grid cell with sedimentation is the result of an inflow of fine sediment (figure 4.22).

Finally, the difference in bed composition changes between the simulations with and without bed level updating are examined. For both the fine and coarse top layer, the difference in composition between the simulation with and without bed level updating is relatively small ($\Delta D50 < 50\mu\text{m}$; figure A.20). The difference is largest for the simulation with the coarse top layer.

4.2. GRADED SEDIMENT

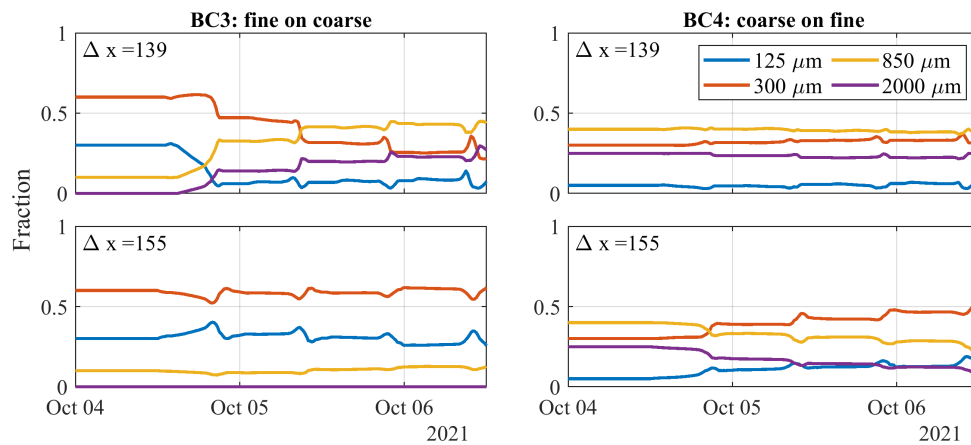


Figure 4.22.: The changes are sediment fractions for simulation BC3 (left panel) and BC4 (right panel) for the grid cell with erosion at the beach face (upper panel) and the grid cell with sedimentation at the foot of the beach face (lower panel). The Δx indicates the position in the cross-shore direction in figure 4.21

4.2.3. Sensitivity analysis

Varying the active layer thickness, but with constant initial bed composition, leads to large differences in bed composition changes (figure 4.23). First of all, if the active layer thickness is larger than the initially specified top layer, it merges the top layer with the under layers. As a result, the initial bed composition in the top layer for the active 0.2m active layer thickness differs from the other simulations. For the simulation with an active layer thickness of 0.05m, the initial coarse top layer is divided into two layers. As a result, the exchange layer is coarser compared to the simulation with an active layer of 0.1m. Therefore, with an active layer thickness of 0.05m, the final bed composition is much coarser.

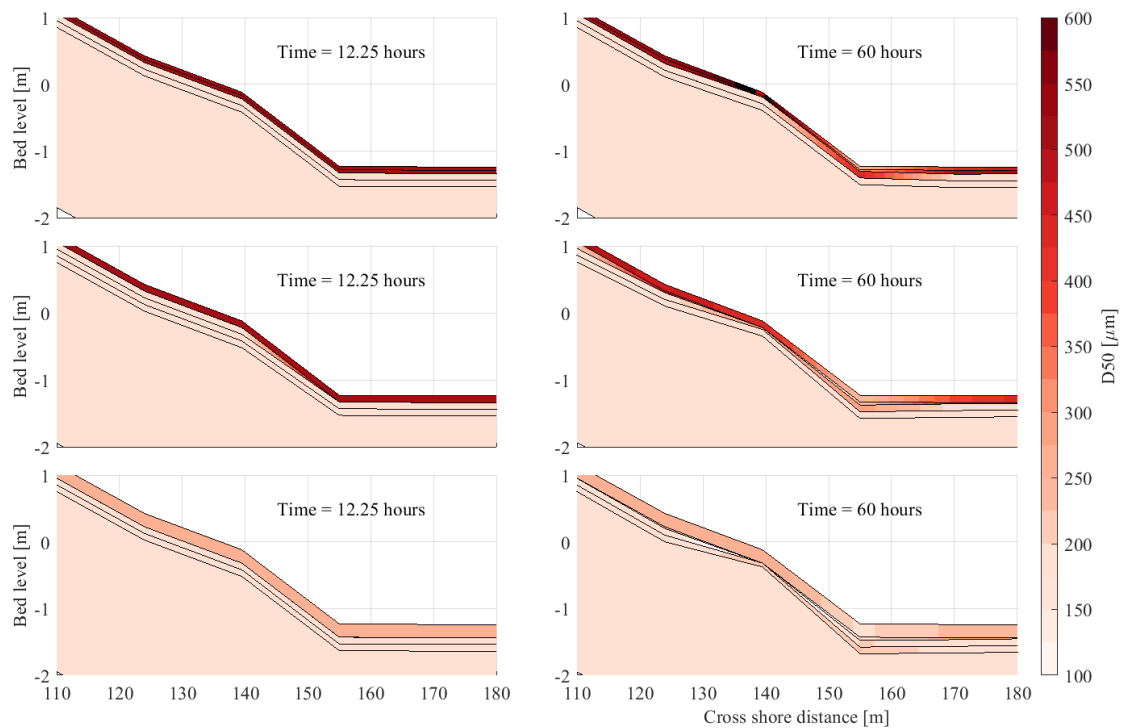


Figure 4.23.: The bed composition changes at the L2 cross-section for the varying active layer thickness, but the same initial bed composition without bed updating. The left panels show the initial state and the right panels the final state. From top to bottom, the active layer thickness is 0.05m, 0.1m and 0.2m.

5. Discussion

In this section, the importance of different drivers and a graded bed on sediment transport in a sheltered coastal system. First of all, the relative importance of different drivers under varying environmental conditions for the PHZD will be discussed. Subsequently, the implication of the results of the PHZD as a prototype for a sheltered coastal system in general will be considered. Thereafter, the influence of multiple sediment fractions and initial bed composition on initial erosion/deposition patterns and their implications will be treated. In addition, the feedbacks between the hydrodynamics, bed composition changes and morphodynamics are examined. Furthermore, the importance and difficulties of graded sediment and bed composition modelling are discussed. Finally, the section will end with the limitations of this study and recommendations for future graded sediment transport studies in sheltered, mixed-energy coastal systems.

5.1. The role of wind, waves and tides

5.1.1. PHZD

During moderate storm conditions, the sediment transport at the PHZD is largely determined by the wind-generated waves. The wave orbital motion greatly increases the maximum bed shear stress while the mean bed stress is relatively unchanged (figure 4.6). Thus, the waves stir the sediment, but the currents drive the transport in agreement with theory (Fredsoe, 1984; Soulsby et al., 1993). As a result, the magnitude of both suspended and bed-load transport increases significantly compared to simulation with only astronomical tides, tides with wind influence or swell waves (figure 4.2). The sediment transport is significantly larger along the spit (L4-L1) than at the sheltered beach towards the NIOZ (L5-L6). Woerdman (2022) found a gradient in the wave height and current velocity correlating to the gradient in sediment transport. Furthermore, at depths where the waves do not interact with the bed, there is a net bed-load and suspended sediment transport in the flood direction along the spit, resulting from a flood dominant tidal asymmetry. This transport is larger for increasing depths as the tidal current increases. However, the sheltered location near the NIOZ harbour shows an ebb dominance, possibly related to a recirculation current (Woerdman, 2022).

For the simulation with wind waves, the bed-load transport increases significantly due to the orbital motion. As a result of the wave interaction with the bed, the orbital motion becomes skewed leading to sediment transport in the direction of wave propagation. At larger depths, the waves

do not affect the motion at the bed, and thus the bed-load transport is still driven by the flood dominant tidal asymmetry. Furthermore, the suspended transport at the beach is dominantly in the offshore direction due to the presence of waves. During low water, high concentrations, due to the wave orbital motion, coincide with an offshore directed current. The offshore current can be explained as an undertow current ($U_{undertow}$) to compensate for the onshore mass flux between wave trough and crest ($q_{non-breaking}$; eq. 2.31 & 2.32). Therefore, the wave orbital motion stirs the sediment and the undertow transports the suspended sediment at the beach.

With increasing wind, the residual currents increase leading to a larger contribution to the bed-shear stresses (figure 4.11). The undertow increases as it is proportional to the mass flux by waves which are larger for higher waves (figure 4.10). In addition, a strong long-shore current arises with increasing energetic storm conditions. The residual driven current depends on the wind direction and magnitude. During winds from the south-southwest to south southeast, the current is in the flood direction while it is ebb directed with winds from the east. As the wind most often comes from the southwestern direction (figure A.1), the sediment transport is expected to be largest in the flood direction in agreement with Klein Obbink (2022) and Woerdman (2022). The residual long-shore current can arise through two mechanisms: 1) alongshore current due to long-shore gradients in the radiation shear stresses (eq. 2.34) or wind-driven throughflow. The long-shore current is in the direction of wave propagation and increases with wave height. Furthermore, the long-shore current is largest in shallower areas where waves already dissipate part of their energy. Therefore, the long-shore wave-driven current can explain net long-shore suspended sediment transport at shallower depths. In addition, the long-shore current could be the result of wind-driven throughflow in the Marsdiep basin (Buijsman & Ridderinkhof, 2007). To summarize, during moderate storm conditions, suspended sediment transport is determined by the undertow. However, during more extreme storm conditions the long-shore current becomes increasingly more important and is driven by long-shore gradients in the radiation shear stress and wind-driven current.

Therefore, it can be said that local wind conditions are the most important driver of sediment transport at the PHZD. For moderate energetic wind conditions, the locally generated wind waves are the most important driver of sediment entrainment and transport. However, during more extreme conditions, the residual long-shore current results in large suspended sediment transport. Nevertheless, the bed shear stresses show that the system is always on the wave-dominated side of the spectrum (figure 4.11).

5.1.2. Implications for sediment transport in sheltered coastal systems

The results discussed above illustrate that the relative importance of tides, wind, wind waves and swell waves is highly dependent on the properties of the local system. The geometry, orientation and position of the tidal inlet(s) are decisive for the relative importance of the different drivers. First of all, the geometry and bathymetry of the basin determine the fetch for the generation of wind waves. At the PHZD, the generation of wind waves was only significant for a small range of wind directions due to the fetch limitation by the geometry of the basin. Furthermore, as tidal basins consist for a large part of inter-tidal areas, the bathymetry will also limit wave growth. Nevertheless, the waves are often essential for significant sediment entertainment while both waves and currents drive transport (PHZD, Carniello et al. (2011), Carniello et al. (2012), Fagherazzi and Wiberg (2009)).

Furthermore, the position of the tidal inlets and geometry of the basin determine if swell waves are able to reach the beach. For the PHZD, the swell waves are unable to penetrate deep into the Marsdiep basin and refract with significant energy towards the PHZD. Similar results are shown for different tidal basins, showing that swell waves do not significantly affect the beaches on the bay side of basins (Sorourian et al., 2020; Travers et al., 2010; Zijlema, 2009). Furthermore, the number and position of the tidal inlets in combination with the local winds determine the effects of wind-driven throughflow. The wind-driven throughflow is important for the PHZD and this is shown for different tidal basins with two connections to the open ocean (Buijsman & Ridderinkhof, 2007; Stanev et al., 2003; Zimmerman, 1976). However, for tidal basins with one connection to the open ocean, different processes as Ekman transport related sea-level fluctuations or water level slopes due to local along-estuary directed winds are of greater importance (Buijsman & Ridderinkhof, 2007; Garvine, 1985).

As a result, the sediment transport patterns at sheltered, mixed-energy coastal systems are often determined by the geometry of the basin. The relative importance of wind waves, wind- and tidal-driven currents will depend on the properties of the basin and the local wind and tidal conditions. As a result, the sediment transport patterns will have larger variability per location compared to the open ocean sites. Therefore, it is important to assess the relative importance of the different drivers for sheltered systems before constructing a coastal intervention.

5.2. Graded sediments and bed composition

5.2.1. Graded sediment

The environmental conditions at the PHZD result in conditions around the threshold for incipient motion (section 4.2.1). Therefore, the differences in critical bed shear stress for the entertainment of different grain sizes could potentially result in preferential transport of fine sediment fractions (Komar, 1987). At wave-dominated, open ocean coasts the conditions are almost exclusively above the threshold for incipient motion (Huisman et al., 2016). In lower energy, sheltered coastal systems the conditions will be often closer to the threshold of incipient motion (figure 4.11). Nevertheless, in environments with a mixed bed, the difference in critical bed-shear stress is often reduced through the effect of hiding and exposure (table 4.1). The degree of hiding and exposure is determined by the sediment sorting (D_{90}/D_{10}) and as a result, the bed composition is a key factor in sediment transport. For the PHZD, the bed is poorly sorted (table 3.3) and thus the hiding and exposure effect influence sediment transport. As a result of the hiding and exposure effect, the bed-load transport is of similar magnitude for all sediment size fractions (figure 4.16). However, the suspended sediment transport is significantly larger for smaller fractions (figure 4.16). As the critical bed-shear stresses are similar, the difference must be related to the difference in fall velocity (eq. 2.2.2). Therefore, it can be said that the hiding and exposure effect is larger for the bed-load component, this is in agreement with literature (De Meijer et al., 2002).

Furthermore, by including more sediment size fractions, the model should close in on the actual behaviour of a mixed-bed. For both the suspended and bed-load transport, increasing the number over sediment size fractions leads to the convergence of the total sediment transport (figure 4.14). The total sediment transport converges for 6 to 8 sediment size fractions, corresponding to the number of fractions proposed by Van Rijn (2007b). In the case of bed-load transport, the effect of including more sediment fractions is limited (figure 4.14). The bed-load transport is lower in the case of multiple sediment fractions, in line with the results for a coarse sand mixture by Van Rijn (1997). In contrast, for the suspended transport the amount of fractions greatly influences the total suspended transport. The suspended transport converges to a sediment transport larger than in a single fraction approach, contrary to findings of De Meijer et al. (2002) and Van Rijn (1997). In addition, the root mean square deviation is significantly larger for suspended transport (figure 4.15). Furthermore, the larger spread between the single and the multi-fraction total sediment transport is related to the fall velocity of finer grain sizes (figure 4.15). While these remain in suspension, contributing to sediment transport, the larger sediment of the single size simulation has already settled.

5.2.2. Bed composition

The bed stratigraphy model allows for the 'bookkeeping' of available sediment opposed to an unlimited supply when the bed composition is not registered. As a result, mechanisms such as armour layering, hiding and exposure and preferential transport can be properly included in the model. The effect of these processes can be seen in the higher rate of sediment transport for the simulation without a bed stratigraphy model (GS) compared to the simulation with a bed stratigraphy model (BC) (figure 4.21). Furthermore, the decrease in the difference in sediment transport between the initial fine and coarse top layer during storm conditions (figure ??) is the result of the development of a coarse armour layer (figure 4.21). During calm conditions, the difference in sediment transport between an initial fine and coarse bed increases over time, thus no armour layer develops. Therefore, it is essential to include a bed stratigraphy model for the correct representation of graded sediment dynamics.

However, the hydrodynamics are of greater importance as similar patterns and magnitudes of sediment transport are found for an initially fine or coarse bed composition. The largest changes in bed composition are found at the location with the largest slope and at the beach face. Furthermore, the bed level changes are relatively similar for simulation with a fine or a coarse initial bed composition (figure 4.20). However, overall a coarser bed results in less erosion along the PHZD (figure 4.20). Huisman et al. (2018) also found that the hydrodynamics are more important for the evolution of the Sand Motor compared to the initial bed composition.

In addition to the effect of the top layer on sediment transport and bed composition, the vertical bed stratigraphy is found to be essential for the evolution of the bed composition. The multi-layer bed leads to a flux of the sediment mixture from the underlayer to the top layer during erosion (eq. 2.15). During sedimentation, the flux from the water level to the bed is a function of the advection of sediment from adjacent cells. As a result, a fine substrate leads to fining of the top layer and a coarse substrate leads to coarsening of the top layer. Therefore, the initial vertical bed composition has a substantial effect on the bed composition changes.

Properly implementing multiple sediments and a bed stratigraphy into a model, such as Delft3D, is not trivial. First of all, including only several size fractions is a simplification of the wide range of grain sizes present in a mixed-sediment system. As the modelled total sediment transport is sensitive to the grain sizes selected (section 4.2.1), this can impose sensitivity of the model to selected sediment size fractions. Around 6 to 8 sediment size fractions resulted in a convergence of sediment transport. However, increasing the number of sediment fractions greatly increases the computation time and storage capacity as the model computes and stores all the equations for each sediment fraction separately.

Second of all, the bed stratigraphy introduces a new and difficult to define boundary condition for the system, namely the initial bed composition (Holland & Elmore, 2008). As a result of the wide range of sediment size fractions with often large spatial and temporal variations present in natural systems, it is difficult to determine the initial bed composition. This would require a large effort of sediment sampling to get the appropriate resolution. Furthermore, even when the initial bed composition is properly defined, the hydrodynamics in the model will still change the bed composition as it tries to reach the model equilibrium. This is often not the same as the observed bed composition. Therefore, trends and patterns can be derived from modelling, but deterministic modelling of bed composition is difficult. Furthermore, the vertical layering of the initial bed is shown to have a major effect on the evolution of the top layer bed composition using a multi-layer bed stratigraphy (section 3.3). Especially for longer time simulation, the vertical layering of the bed may become an important boundary condition for the morphodynamics of the model.



Figure 5.1.: On the left a fine layer is deposited on a coarse substrate after energetic conditions while on the right an armour layer present at the PHZD is shown.

Finally, the multi-layer bed stratigraphy uses a diffusive approach for the fluxed between the active layer, the under layer and the water column. However, the observed bed composition changes are event-based dynamics of the actual system and lead to discrete bed layers. The observed bed composition changes showed a coarsening of the bed during calm conditions resulting in an armour layer (figure 5.1). After storm events, the bed composition was vertically sorted due to the settling mechanism leading to a fine top layer on top of a coarse under layer (klein Obbink (2022); upper row in figure 5.2). However, during an erosion event, the multi-layer stratigraphy without bed level changes results in a fraction of the sediment mixture in the active layer being suspended. As a result, the active layer will be filled with sediment from the underlayer (middle row in figure 5.2). During a sedimentation event, the settling sorting mechanism still leads to a difference in settling time, but both the fine and coarse sediment fractions will be mixed with the same mixture of the active layer. A fraction of the sediment of the active layer will be mixed in with the underlayer.

5.3. LIMITATIONS AND FUTURE RECOMMENDATIONS

Therefore, the multi-layer bed stratigraphy without bed level changes leads to a diffusive interaction between the water column, active and under layer. As a result, this method is unable to replicate the more discrete layering of the sorting events observed. If the multi-layer bed stratigraphy is used in combination with bed level changes, it was expected to better represent the vertical layering (lower row in figure 5.2). However, the differences in bed composition changes with and without bed level change are relatively small and the pattern does not change (figure A.20). As a result, the settling mechanism is also not well replicated with the multi-layer model in combination with bed level changes.

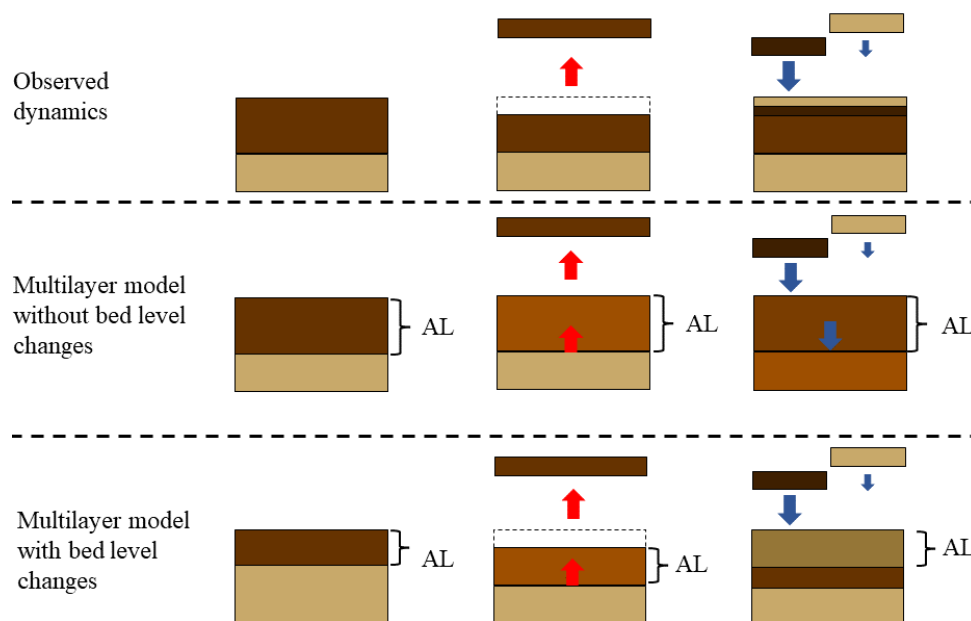


Figure 5.2.: Schematic illustration of the bed composition changes in the bed stratigraphy during an erosion event followed by a phase of sedimentation. The brown colour indicates the D50 of the layer with darker brown indicating a coarser layer, the red arrow indicates sediment fluxes during erosion and the blue arrow indicates sediment fluxes during sedimentation. The active layer is indicated by the parentheses with the text 'AL'.

5.3. Limitations and future recommendations

In addition to the difficulties with the multi-layer model, this study has several other limitations. First of all, the model uses a curvilinear grid in an area that has a complex geometry. Furthermore, the grid cells are not parallel to the beach (as it has to fit in the outer North Sea grid) and thus

local enhancement of the grid is not possible. Even though the model consists of three domains in order to enhance resolution, the grid cells at the beach are in the order of 10 by 12m. As a result, the short and steep beach face is represented by only 2 to 3 grid cells even though the most important processes occur in this small area. Furthermore, the small and short period waves in combination with the relatively large grid result in several waves per grid cell which is undesirable for numerical stability. Therefore, it is recommended to use an unstructured grid for the more complex geometries of tidal basins (f.i. Delft3D FM). This will allow for the appropriate resolution in areas with large gradients.

Furthermore, the simulations with a constant wind in time and space use a tidal time series from a different period. Therefore, the effect of storm surges is not taken into account in the tidal time series at the boundaries of the model. Next to this, the initial bed composition was based on sediment samples which were limited in spatial and temporal resolution. Furthermore, vertical heterogeneity of the bed was taken into account but horizontal variations were not considered. As a result, the initial bed composition was a simplified representation of the sediments found at the PHZD. In addition, the Delft3D model does not take carbonates into account, even though these were frequently found in the sediment samples.

The initial composition is difficult to appropriately implement in the model and is sensitive to several user-defined parameters. In addition, the initial bed composition is often poorly known in the spatial (horizontal and vertical) and temporal domains. Therefore, it might be better to use a vertically uniform bed with sediment fractions based on sampling. Furthermore, in order to deal with the model trying to reach equilibrium in the initial adjustment phase, would be to use the outcome of the previous spin-up simulation. When the model is simulated with the multi-layer bed stratigraphy without bed level changes and a morphological acceleration factor, the initial changes of the model trying to reach equilibrium will be circumvented (van der Wegen et al., 2011).

6. Conclusions

The aim of this research was twofold: to identify the drivers of sediment transport in a sheltered coastal system under varying environmental conditions and to examine the effect of graded sediment and initial bed composition on sediment transport in a sheltered coastal system. In order to do so, a combined Delft3D-FLOW and WAVE model was extensively calibrated with field data collected during the 6-week SEDMEX field campaign. Subsequently, the model was used to structurally examine the effect of different drivers, graded sediment and initial bed composition. In the following section, the conclusions of this research will be presented according to the research question.

What is the relative importance of different drivers on the transport of sediment with a uniform grain size at a sheltered coastal environment, during a) calm weather conditions and b) storm conditions?

Sediment transport in a sheltered, mixed-energy coastal system is subjected to the force of tides, winds and waves. For the sheltered, mixed-energy systems the local wind in combination with the geometry of the basin is shown to have the largest influence on sediment transport. Furthermore, swell waves are unable to reach the sheltered site with significant energy and this is found frequently in mixed-energy, sheltered coastal systems. At the PHZD, wind waves are identified as the main stirring mechanism while wind and wave-driven currents in combination with the wave shape determine the direction of sediment transport. Wind wave generation is limited by the fetch and the local wind climate. Furthermore, the wind-driven residual current depends on the geometry of the basin, the number of tidal inlets and the local wind climate.

Under varying wind velocity and direction, the relative importance of the different drivers on sediment transport changes. During calm conditions, sediment transport rates are small and are mostly determined by the tidal currents. For moderate storm conditions ($10 - 15 \text{ ms}^{-1}$ wind velocity), the waves become the most important stirring and transport mechanism in shallow water depths. As a result, the system is classified as a wave-dominated to a wave-only system (figure 4.11). Bed-load transport is shown to be almost exclusively caused by waves while suspended transport is the result of combined wave-driven and wind-driven currents. During extreme storm conditions ($15 - 20 \text{ ms}^{-1}$ wind velocity), the residual wind-driven current becomes increasingly more important. As a result, the system shifts towards a mixed-energy wave-dominated system (figure 4.11). Furthermore, the direction of residual wave- and wind-driven current is highly dependent on the wind direction. As the wind most often comes from the southwestern direction, the sediment transport is expected to be largest in the flood direction. Therefore, it can be concluded that in sheltered, mixed-energy

systems, the relative importance of the different drivers varies due to the geometry of the tidal basin and varying environmental conditions.

What is the effect of graded sediment and initial bed composition on sediment transport and the related erosion/deposition patterns in a mixed-energy coastal environment, during a) calm weather conditions and b) storm conditions?

The conditions at these sheltered, mixed-energy systems are more often around the threshold for incipient motion compared to open ocean coasts. As a result, the condition for preferred transport is more frequently met. However, for poorly sorted beds this is counteracted by the effect of hiding and exposure. Therefore, in order to properly account for graded sediment dynamics (preferential transport, hiding and exposure and bed armouring), it is necessary to model bed stratigraphy. Furthermore, the total sediment transport is sensitive to the sediment fractions chosen while it is difficult to determine the appropriate sediment fractions.

During calm conditions bed composition changes are small and at the beach face no significant change. However, during moderate storm conditions, the bed composition changes are significant at the beach, concentrated in the areas with the largest gradient in bed level. At the beach face, the fine sediments at the steep beach face slope are transported to the plateau below leading to a coarse slope and a fine plateau below. This is the result of the model trying to reach equilibrium and at these steep slopes, large gradients in bed composition will arise.

Including a bed composition model will limit sediment transport as preferential transport of fine material results in a coarse armour layer, limiting sediment transport. However, the sediment transport rate between a fine and a coarse initial bed composition does not vary significantly during a simulation. Only during the start of the simulation when the model is quickly adjusting to the hydrodynamics, do the sediment transport rates differ. The vertical layering in the bed composition in combination with the definition of the thickness of the active layer does show to have a large influence on sediment transport. During erosion, the active layer is replenished with sediment from the mixture below and thus this determines the change in D_{50} of the top layer.

To conclude, the complex interaction of different drivers and graded sediment at a mixed-energy back-barrier beach is difficult to model. First of all, the role of the different drivers is tidal basin and environmental conditions dependent. Furthermore, including graded sediments and a bed stratigraphy has a significant effect on sediment transport. However, the current configuration of the multi-layer bed stratigraphy is not optimal as it is sensitive to user-defined parameters and the initial conditions. Finally, the new introduced boundary condition of the initial bed composition is difficult to determine based on observations.

Acknowledgements

Foremost, I would like to thank dr. Timothy Price and Prof. dr. Huib de Swart for supervising me during my master thesis. I am grateful for the opportunity to do a combined thesis project with two supervisors from two different faculties. Timothy, thank you for your daily supervision, the useful feedback session and the possibility to always approach you with the numerous troubles that I encountered on the way. Huib, thank you for your lectures on physics and the many well-put metaphors to serve as motivation or to simplify difficult phenomena. Furthermore, I would like to thank dr. Maarten van der Vegt for his help with Delft3D and valuable contributions during feedback sessions. Without the help of Timothy, Huib and Maarten, I would not have succeeded and learned as much as I did.

Furthermore, I would like to thank my fieldwork colleagues Jorn Bosma, Marlies van der Lugt, Martijn klein Obbink and Jelle Woerdman for the good times in the field and for all the work put into the data collection and data processing. In addition, I would like to thank the technical teams of the TU Delft and the University Utrecht for setting up all the equipment. Special thanks go out to Martijn and Jelle for being my colleagues during the interesting but difficult period of writing a master thesis. In addition to graduating, this also resulted in new friendships. Besides, I want to thank the other students and friends for working on their own thesis, making the days of working on my thesis more fun. Furthermore, I would like to thank Kimberley Koudstaal for helping me get started with Delft3D and for solving numerous model errors along the way.

Also, I would like to thank my parents for making it possible for me to study in the first place and to pursue my passion. Finally, I want to express my gratitude to Stella, for all the meals cooked so I could continue working and the talks to clear my mind.

Appendix

A. Supplementary figure

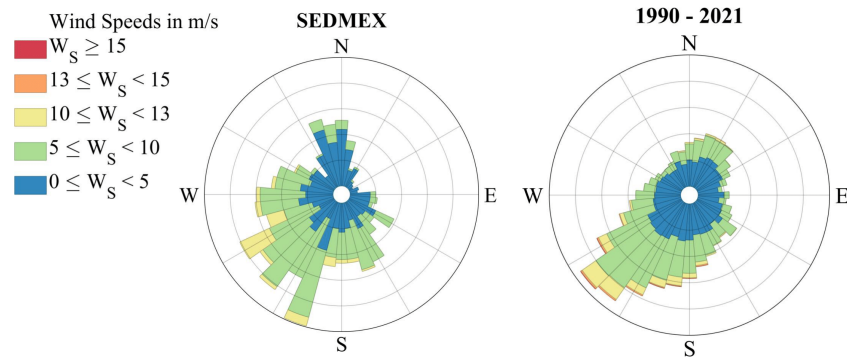


Figure A.1.: The measured windroses for the 'de Kooy' weather station of the KNMI for the period between 1990-2021 (left) and the SEDMEX field campaign (right). The colours indicate the wind velocity while the radial grid shows the occurrence.

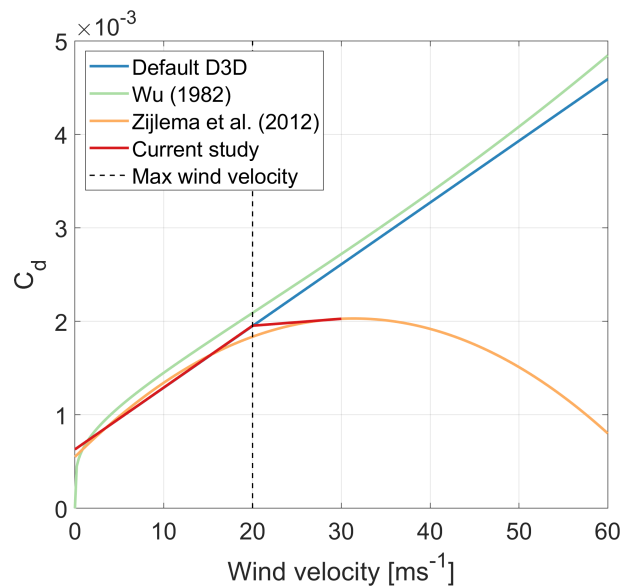


Figure A.2.: The wind drag coefficient according to the Delft3D default, Wu (1982), Zijlema et al. (2012) and the coefficient used in this study.

A.1. DRIVERS

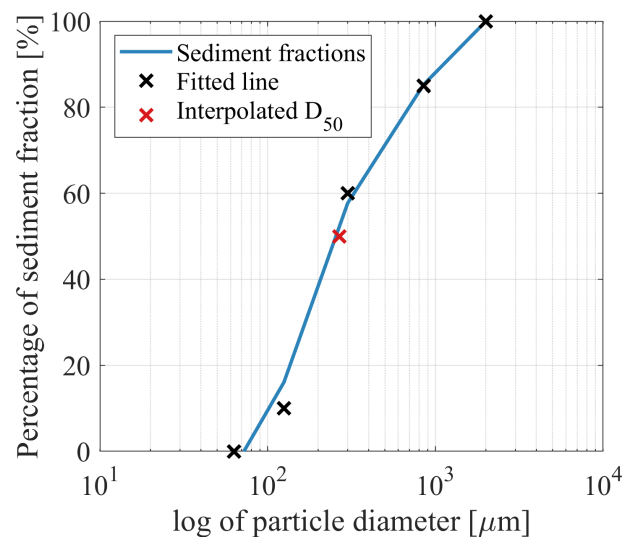


Figure A.3.: Example of the fitting procedure to determine the D50 based on the sediment size fractions.

A.1. Drivers

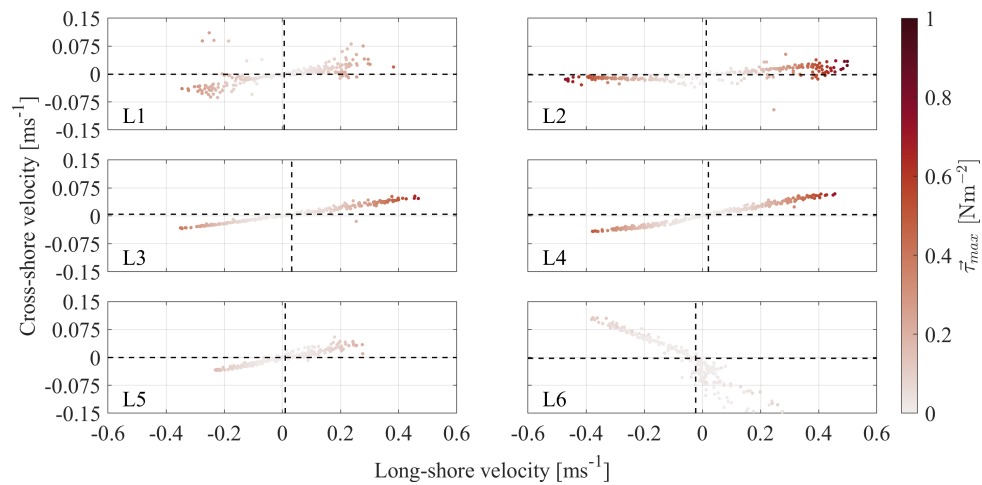


Figure A.4.: Scatter plot of the long- and cross-shore velocity of the 6 long-shore locations for the simulation with only tides (D2). The colours indicate the concentration on a log scale and the dashed lines the mean long- and cross-shore velocity.

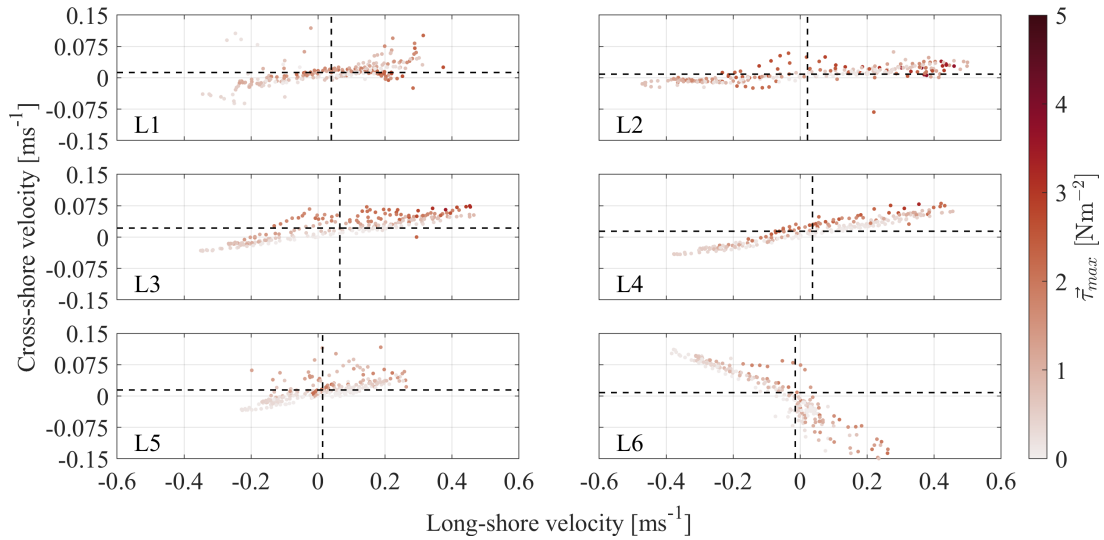


Figure A.5.: Scatter plot of the long- and cross-shore velocity of the 6 long-shore locations for the simulation with wind waves (D3). The colours indicate the concentration on a log scale and the dashed lines the mean long- and cross-shore velocity.

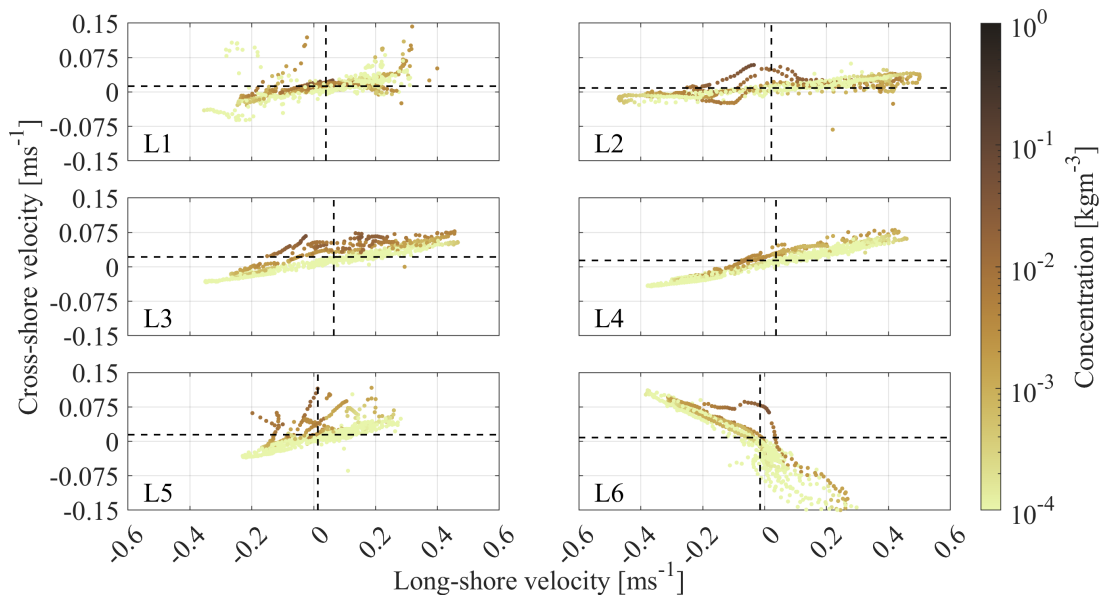


Figure A.6.: Scatter plot of the long- and cross-shore velocity of the 6 long-shore locations for the simulation with wind waves (D3). The colours indicate the concentration on a log scale and the dashed lines the mean long- and cross-shore velocity.

A.1. DRIVERS

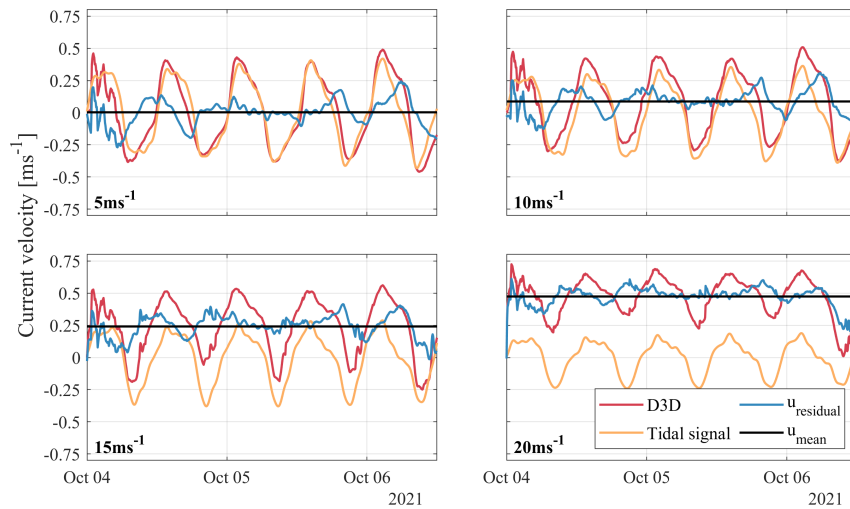


Figure A.7.: Current velocity over time for the simulations with increasing wind velocity (D6). The red line indicated the time series of Delft3D, the yellow line the extracted tidal signal, the blue line the residual current and finally the black line shows the mean current.

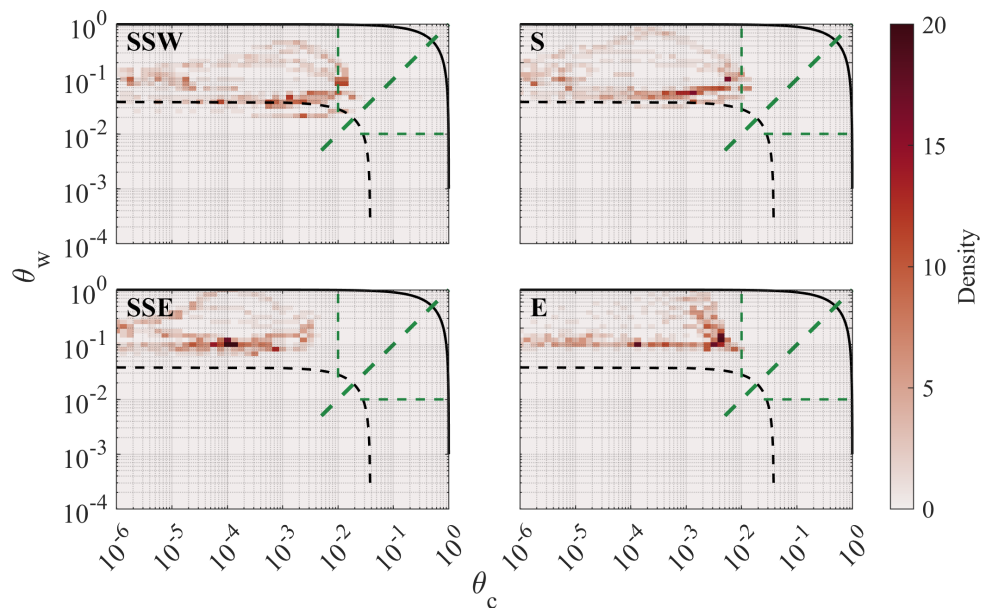


Figure A.8.: The current- and wave-related bed-shear stresses for the simulations with varying wind directions (D7). The x-axis shows the current related Shields bed shear stress (θ_c) and the y-axis the wave-related Shields parameter (θ_w). The colours indicate the density of the output of the simulation for each wind direction. The dotted black line shows the threshold for incipient motion for the $300\ \mu\text{m}$ sediment fractions and the solid black line indicates the sheet flow threshold. Furthermore, the thick dotted green line indicates the separation between wave/tide-dominated and the thin dotted green lines the separation between a mixed or a wave/tide only environment.

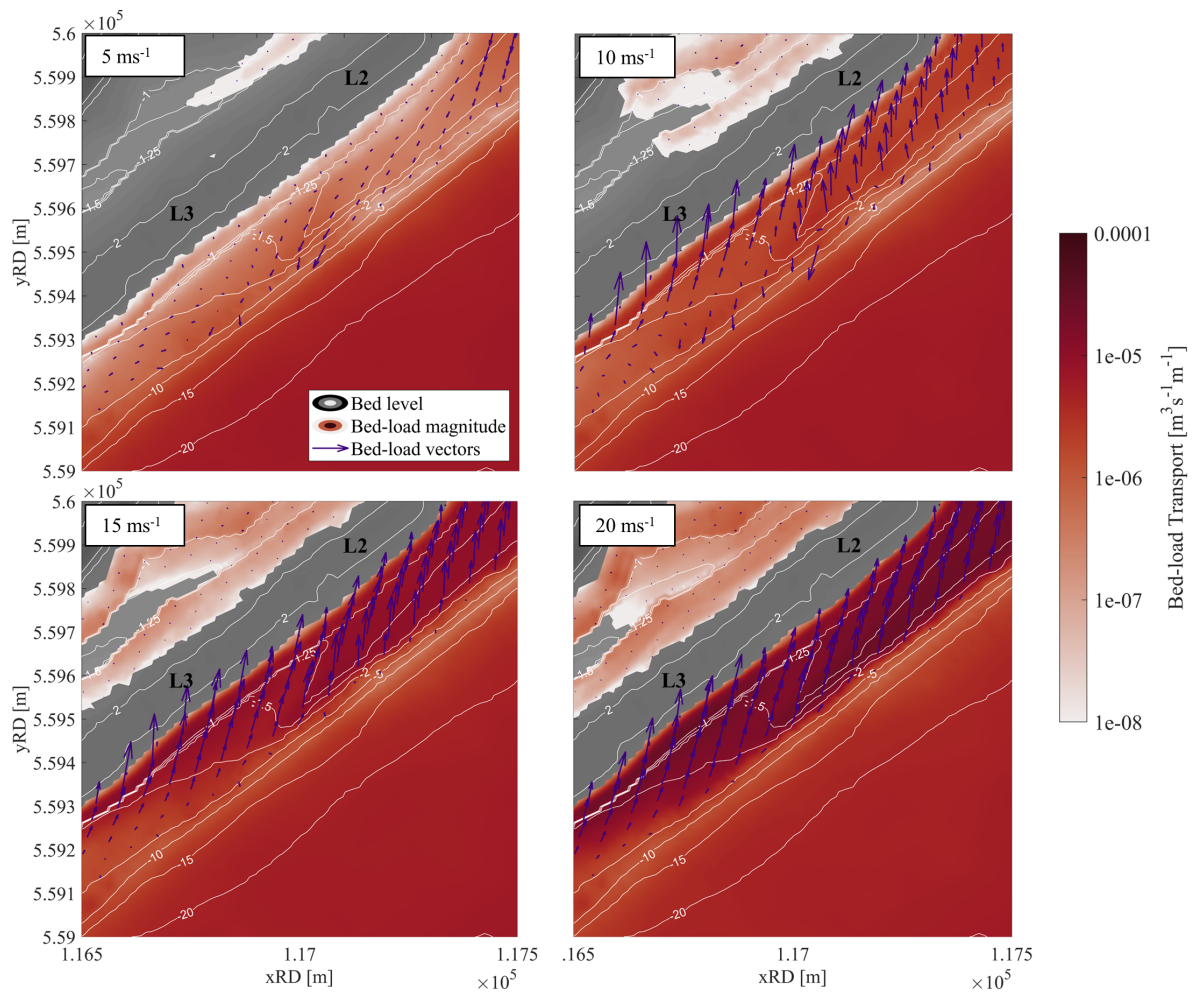


Figure A.9.: The mean bed-load transport for the D6 simulations with varying wind velocities for the centre of the spit at the PHZD. The grey shades indicate the bed level, the red shades the bed-load sediment transport magnitude on a log scale and the arrows indicate the bed-load sediment transport vector.

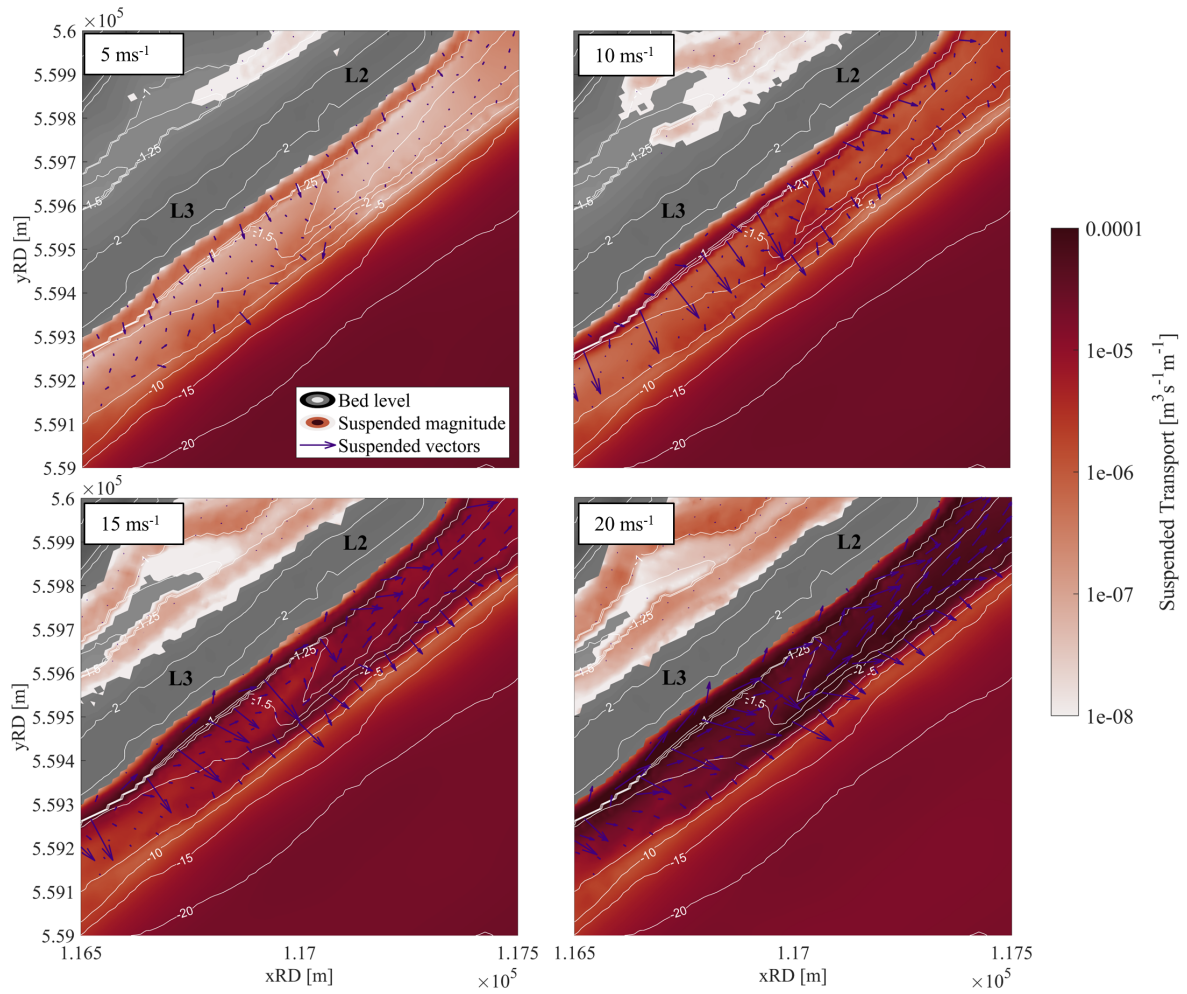


Figure A.10.: The mean suspended transport for the D6 simulations with varying wind velocities for the centre of the spit at the PHZD. The grey shades indicate the bed level, the red shades the suspended sediment transport magnitude on a log scale and the arrows indicate the suspended sediment transport vector.

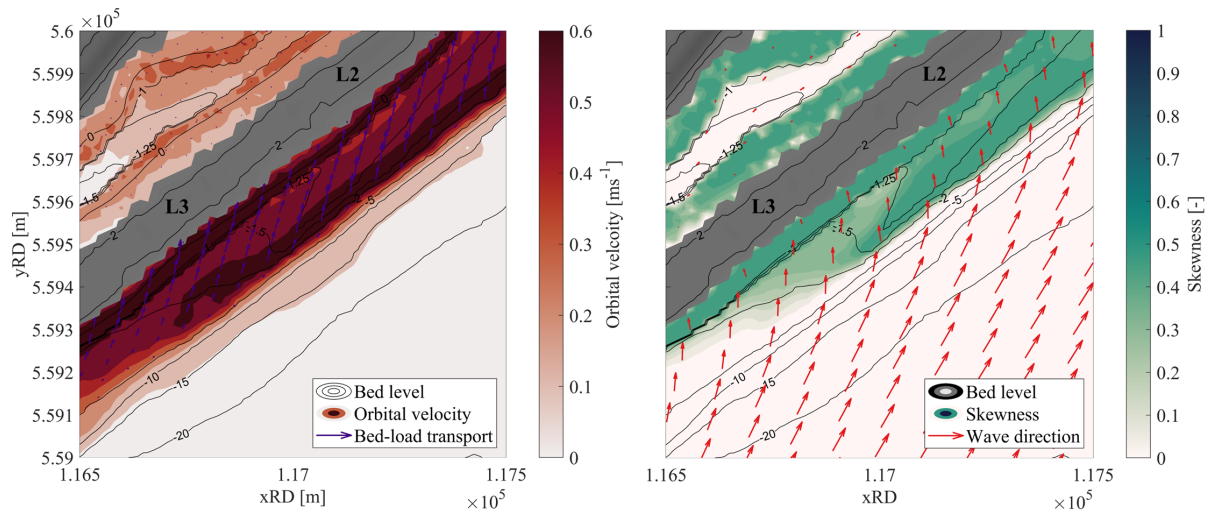


Figure A.11.: The bed-load transport in relation to the wave direction and skewness for simulation D6 (20ms^{-1}). The left panel shows the mean peak near-bed orbital velocity (red shades) and the bed-load transport (purple vectors) for the centre of the spit at the PHZD. In the right panel, the skewness (green shades) and the direction of wave propagation (orange vectors) are shown for the same area.

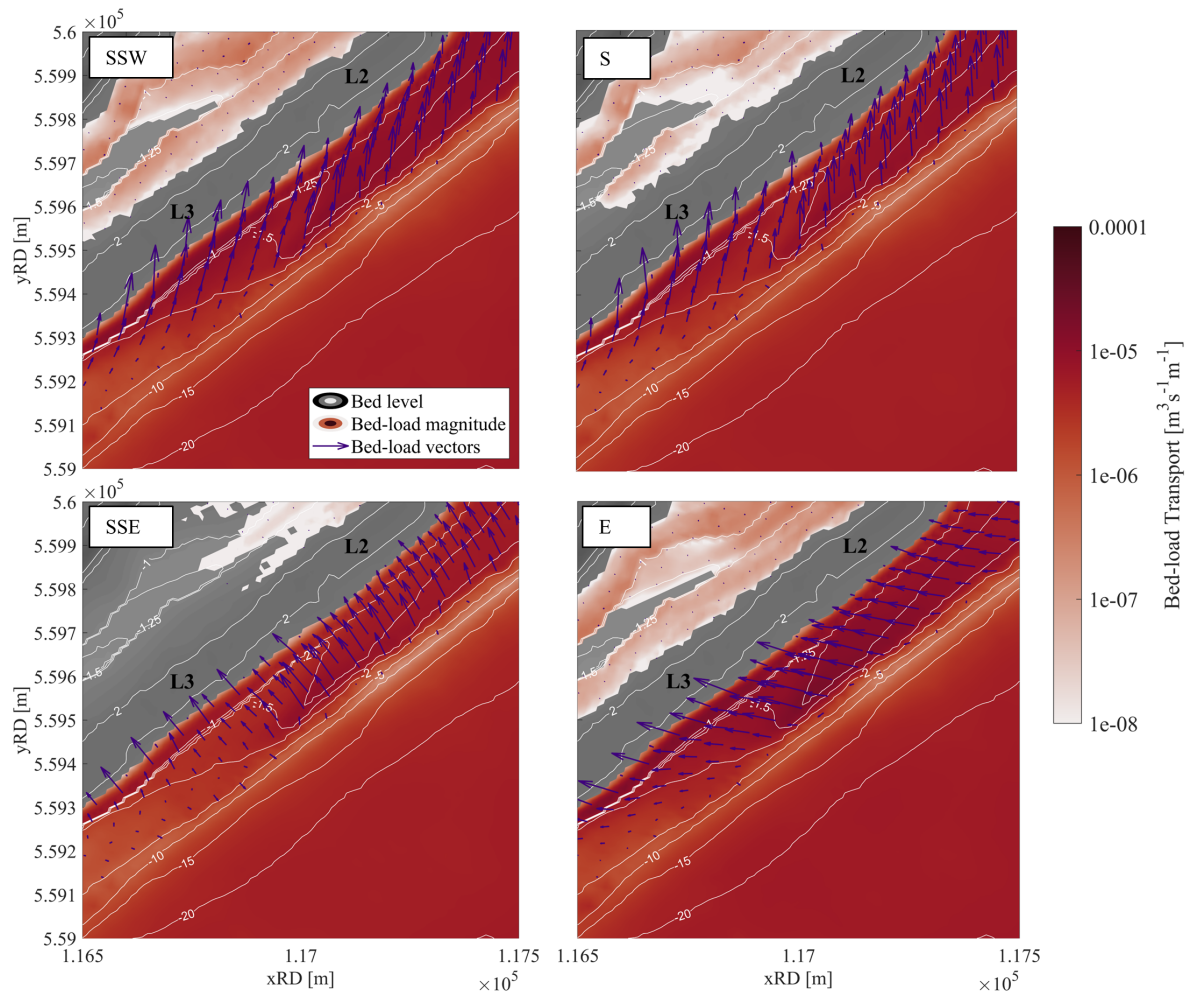


Figure A.12.: The mean bed-load transport for the D7 simulations with varying wind directions for the centre of the spit at the PHZD. The grey shades indicate the bed level, the red shades the bed-load sediment transport magnitude on a log scale and the arrows indicate the bed-load sediment transport vector.

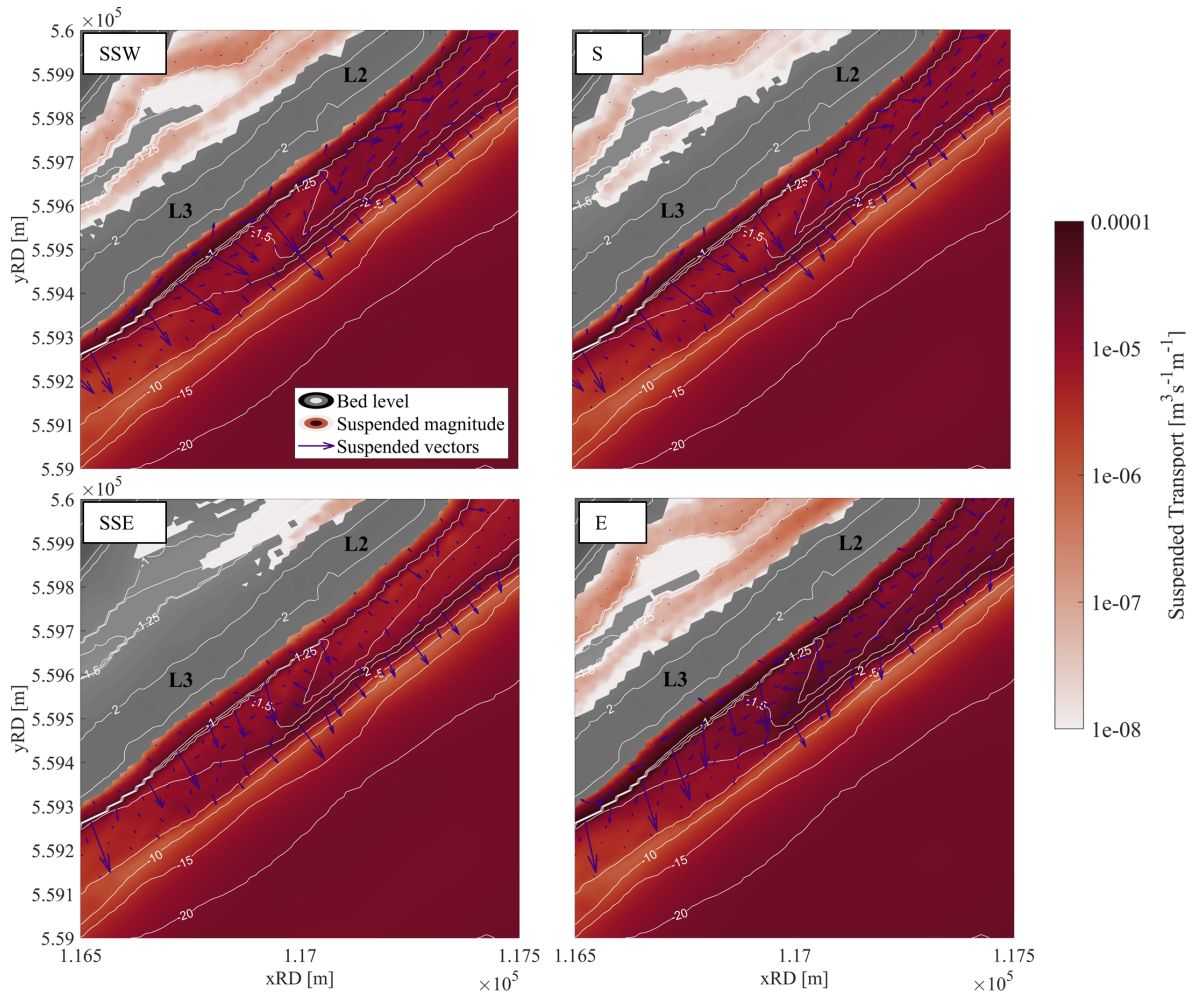


Figure A.13.: The mean suspended transport for the D7 simulations with varying wind directions for the centre of the spit at the PHZD. The grey shades indicate the bed level, the red shades the suspended sediment transport magnitude on a log scale and the arrows indicate the suspended sediment transport vector.

A.1. DRIVERS

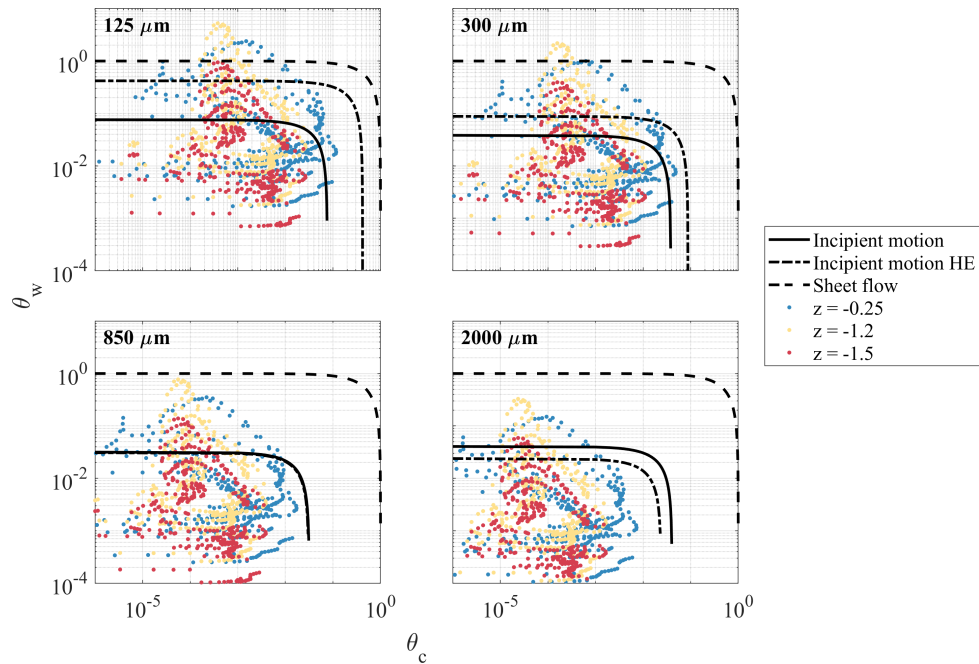


Figure A.14.: The wave- and current-related bed shear stresses plotted against each other for different water depths. The four plots show the four sediment fractions used in the GS4 simulation. Furthermore, the incipient motion and sheet flow regime are indicated

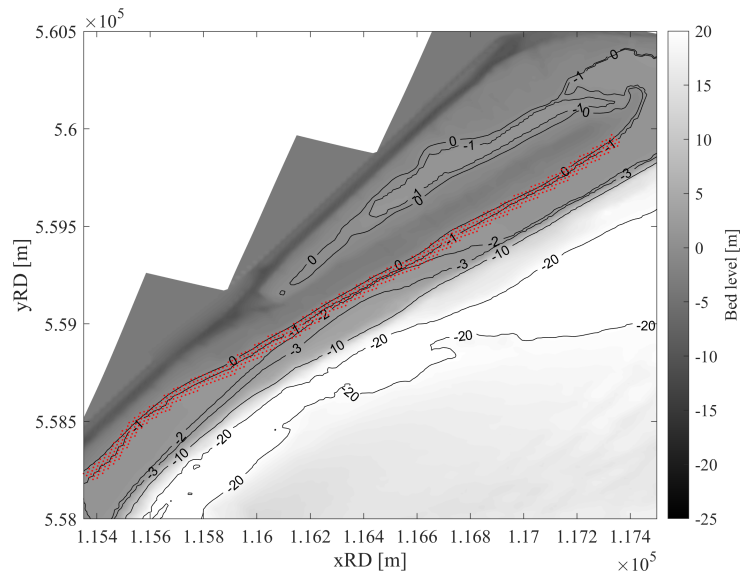


Figure A.15.: The centres of the grid cells were used for the data analysis of the influence of the initial bed composition.

A.1. DRIVERS

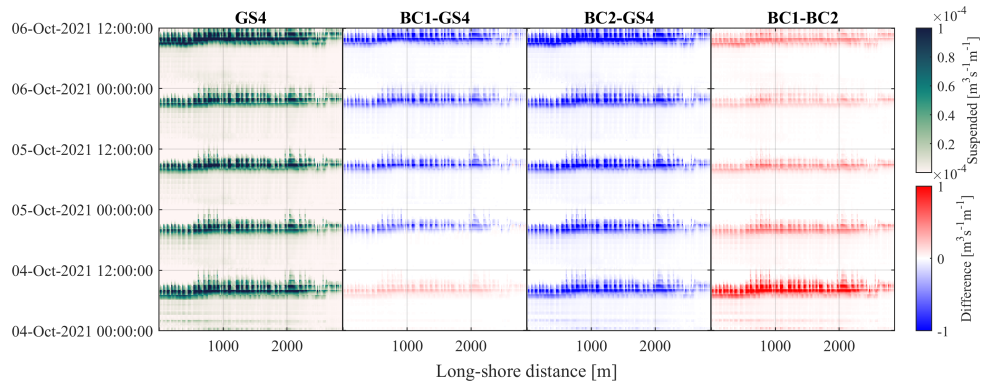


Figure A.16.: Total suspended sediment transport for the first grid cell above the -1m bed elevation in the long-shore direction. The long-shore axis follows the water line where the 0m is located at the spit and increases towards the sheltered beach

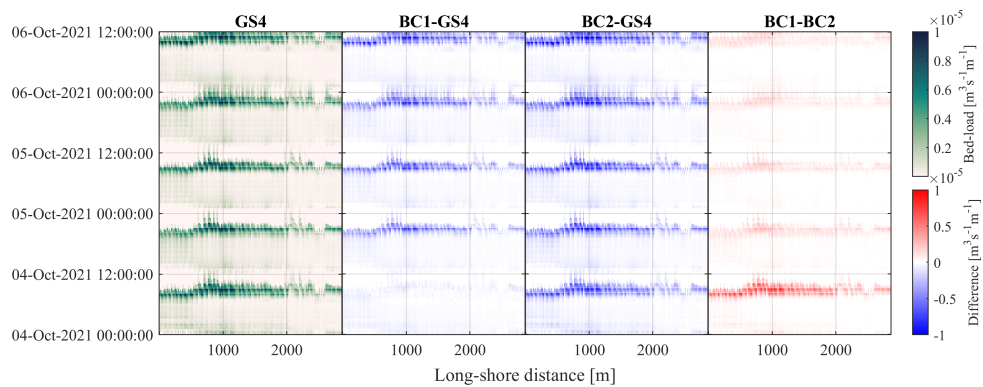


Figure A.17.: Total bed-load sediment transport for the first grid cell above the -1m bed elevation in the long-shore direction. The long-shore axis follows the water line where the 0m is located at the spit and increases towards the sheltered beach

A.1. DRIVERS

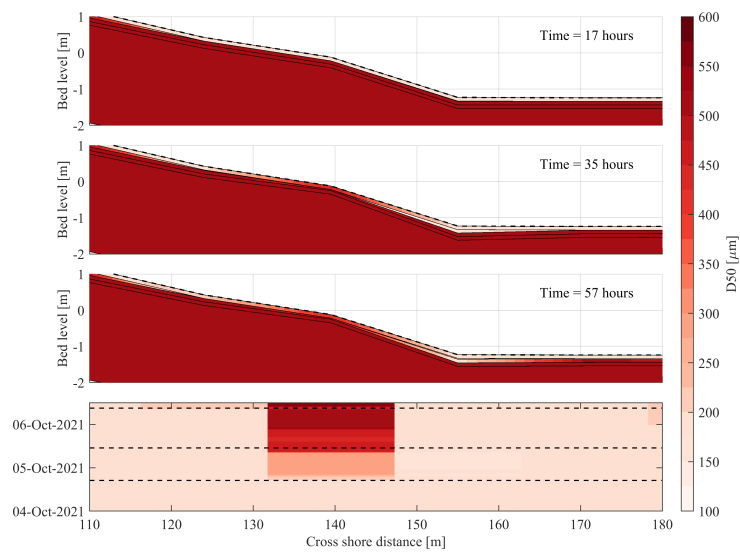


Figure A.18.: The bed composition changes at the L2 cross-section for the BC3 simulation without bed updating. The upper three panels show the cross-section for different moments in time. Here the colours indicate the D50 and the dashed line the initial bed level. The lower panel shows the D50 changes of the top layer over time (y-axis) where the dashed line indicates the moments in time of the cross-sections in the upper three panels.

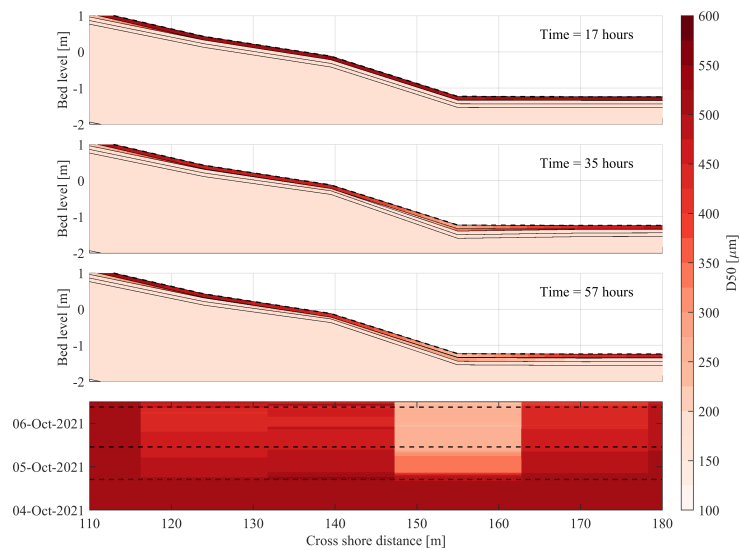


Figure A.19.: The bed composition changes at the L2 cross-section for the BC4 simulation without bed updating. The upper three panels show the cross-section for different moments in time. Here the colours indicate the D50 and the dashed line the initial bed level. The lower panel shows the D50 changes of the top layer over time (y-axis) where the dashed line indicates the moments in time of the cross-sections in the upper three panels.

A.1. DRIVERS

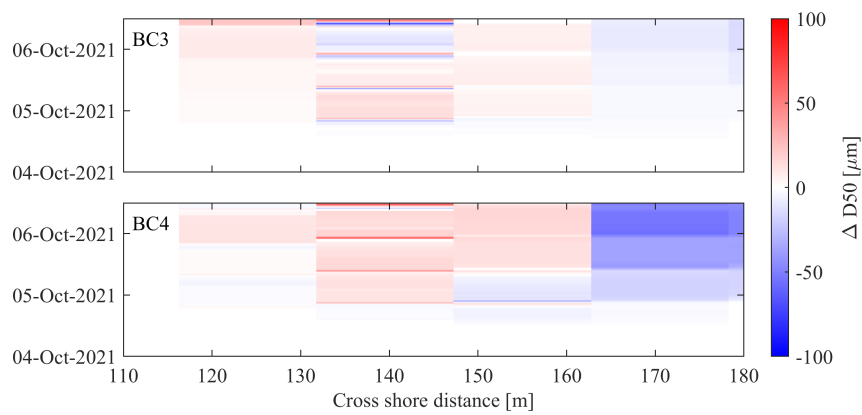


Figure A.20.: The changes in sediment fractions for simulation BC4 for the grid cell with erosion at the beach face (upper panel) and the grid cell with sedimentation at the foot of the beach face (lower panel). The Δx indicates the position in the cross-shore direction in figure 4.21

B. Background information PHZD

The PHZD is a back-barrier beach located on the southeast side of Texel in the Marsdiep basin. The new sand dike replaced the traditional dike that did not comply with coastal protection standards. Furthermore, it also partly replaces the erosive shoal in front of the old dike, the Schanserwaard. The sandy dike solution was constructed as a natural and sustainable alternative to strengthening the current dike.

B.0.1. Marsdiep basin

The Marsdiep basin is the largest and westernmost basin of the Wadden Sea, reaching from the Texel inlet in the west to the Eierland and Vlie basin to the east. The bathymetry of the basin is characterized by large variations in water depth on a small spatial scale: from deep meandering channels to numerous shallow inter-tidal flats. Similar to the rest of the Wadden Sea, the Marsdiep basin is a mixed-energy environment with a mean tidal range of 1.4m, mean significant wave height of 1.3m and extreme wave height of over 6m (Elias et al., 2012). Nevertheless, the wave heights will vary through the basin due to the bathymetry and geometry of the basin.

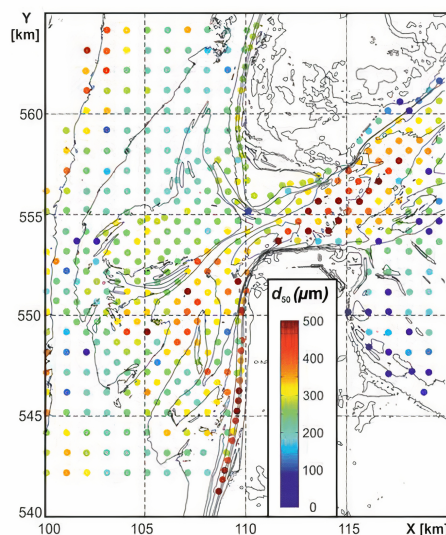


Figure B.1.: Observations of the D_{50} of the sediment for the Texel inlet and western side of the Marsdiep basin (Elias & van der Spek, 2017).

The construction of the closure dam the Afsluitdijk (closing of the Zuiderzee) had a major influence

on the hydrodynamics and geometry of the basin (Buijsman & Ridderinkhof, 2007). As a result, the sediment budget of the Marsdiep basin has not reached an equilibrium since and pronounced morphodynamic changes occurred after the construction (Dastgheib, 2012). For instance, the Marsdiep and Vlie basin used to be connected through the Zuiderzee (Elias et al., 2012), but are now only connected through channels on both sides of the watershed dividing the two basins (Buijsman & Ridderinkhof, 2007). Therefore, the western Wadden Sea can be classified as multiple tidal inlet systems, and thus, the tides, wind and freshwater discharge can result in a residual flow through the system (Buijsman & Ridderinkhof, 2007). In the western Wadden Sea, the wind-driven residual current drives a transport from the Texel to the Vlie inlet while the tidal-driven residual transport is in the opposite direction (Duran-Matute et al., 2016). Nevertheless, the wind effect is dominant despite the episodic nature of wind events (Duran-Matute et al., 2016). The sediment composition is variable through the domain: from medium to coarse sand in the deeper tidal channels to mud and fine sands on the shallower inter-tidal flats (Figure B.1).

B.0.2. Schanserwaard inter-tidal flat

The Schanserwaard inter-tidal flat is the former erosive inter-tidal flat located in the area of the study site. As a result, of the landward movement of the Texelstroom channel, the inter-tidal flat eroded 0.5m on average during the period from 1991 to 2009 (Witteveen + Bos, 2011). In order to reduce this effect, erosional protection on the northwest side of the channel was placed and updated by the Dutch government. The inter-tidal flat itself consisted of relatively fine sediment with small patches of coarse material (figure B.2). In contrast with the observations of the D_{50} of the Texel inlet and Marsdiep basin (Figure B.1), there does not seem to be a clear correlation between water depth and grain size. However, there is a clear difference between the finer southwestern and the coarser northeastern region of the intertidal flat.

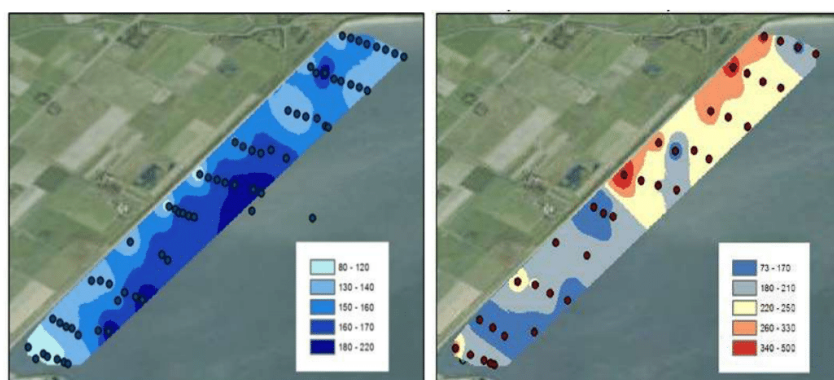


Figure B.2.: Observations of the D_{50} of the sediment for the Schanserwaard inter-tidal flat (Brand, 2016)

B.0.3. Prins Hendrikzanddijk

The Prins Hendrikzanddijk is a sand nourishment/dune that is constructed to strengthen the existing dike located behind the Schanserwaard inter-tidal flat. In addition, a spit is created in front of the sand dune, in order to provide an inter-tidal area for the enhancement of the local ecosystem. The PHZD itself consists of a safety dune consisting of relatively fine sand ($D_{50} \approx 300\mu\text{m}$) and an erosional wear layer of coarse sediment ($D_{50} > 600\mu\text{m}$; Figure B.3). Furthermore, the dune consists of a beach area sheltered by the NIOZ harbour and a spit area located on the northwestern side of the dune. In addition to the erosional wear layer, a shell layer was placed on top of the spit in order to reduce wind-related erosion. Finally, the beach face of the PHZD is steep, increasing in slope from the sheltered beach (average slope $L5 = 1/15.4$) towards the spit (average slope $L2 = 1/12.4$; figure 1.1).

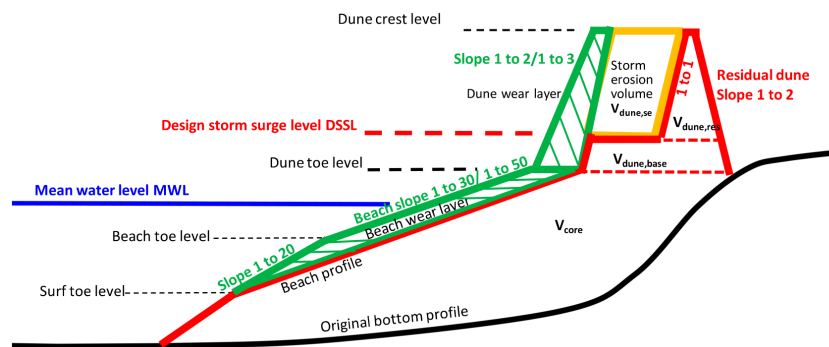


Figure B.3.: Schematic overview of the design of the PHZD where the colours indicate the safety dune (orange and red), the erosional wear layer (green) and the mean water level (blue). The figure and further information about the design of the PHZD are given by Perk et al. (2019).

C. Calibration details

C.1. Calibration details

Table C.1.: Table showing the simulations performed to calibrate the water levels and velocity in the Delft3D model

Simulation	Description
Manning low	$n = 0.023$
Manning high	$n = 0.026$
Coleman-Whitebrook low	$u, v = 0.015 \text{ m}$
Coleman-Whitebrook high	$u, v = 0.03 \text{ m}$
Chezy low	$C = 53$
Chezy high	$C = 56$
Chezy dd grid	Varies per grid
Chezy dd cell	Varies per cell

Table C.2.: Table showing the performed model simulation for the calibration of the Delft3D-FLOW module

Parameter	Base	Variation
Bottom friction	0.038	0.067
Triad-triad	Off	On
Whitecapping	Komen et al. (1984)	van der Westhuysen et al. (2007)
Stress formulation	Fredsøe (1984)	Van Rijn et al. (2004)
Swell/Wind	Wind	Swell

C.2. Model calibration and sensitivity analysis

C.2.1. Flow calibration results

The results of the FLOW calibration show that the water level is simulated well with each roughness formulation. The left panel of figure C.1 shows the scattered measures and modelled water levels while the right panel shows the fitted line for each of the different roughness formulations. First of all, all formulations reproduce the water reasonably well as the spread around the 1:1 line is small and the correlation is close to perfect (Figure C.1 ;Table C.3). However, the fitted lines of the right panel of figure C.1 show that the Chezy formulations are closest to a perfect model score. The smallest RMSE is achieved with the grid varying Chezy formulation (Table C.3).

The long and cross-shore components of the velocity are less well reproduced by the model. The

C.2. MODEL CALIBRATION AND SENSITIVITY ANALYSIS

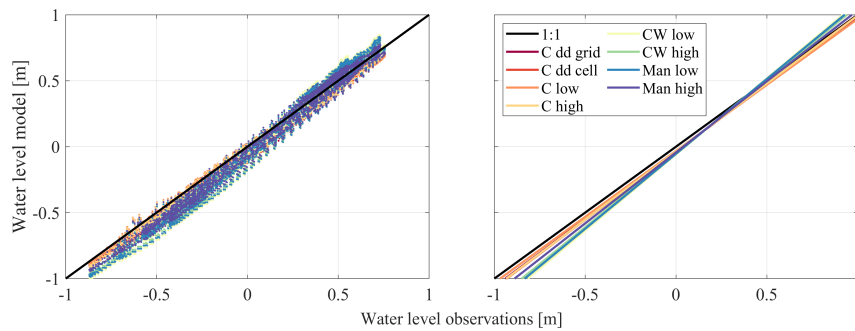


Figure C.1.: The figure shows the fitted lines between the model and the observed water level. The different colours of the lines indicate the parameterization of that simulation.

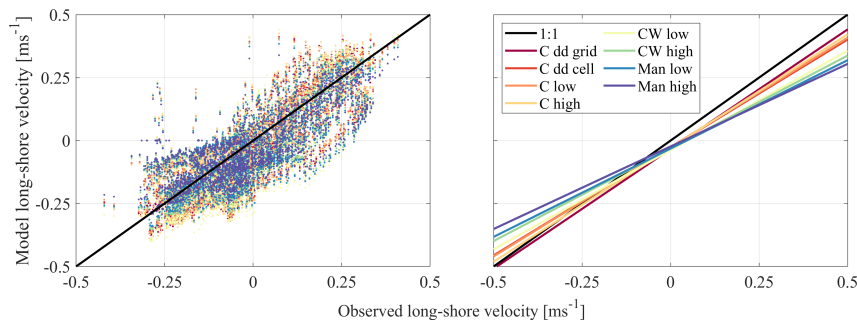


Figure C.2.: The figure shows the fitted lines between the model and observed long-shore velocity. The different colours of the lines indicate the parameterization of that simulation.

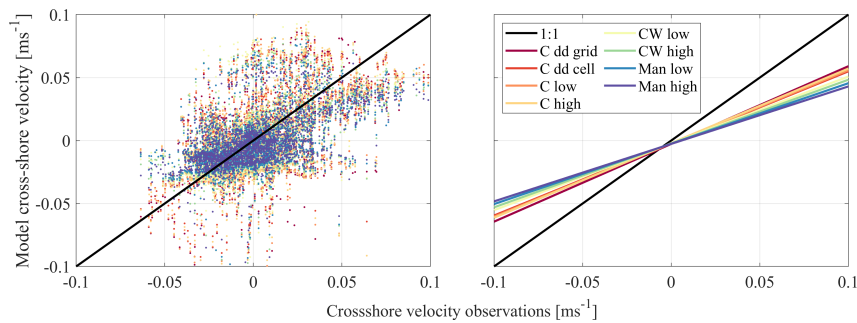


Figure C.3.: The figure shows the fitted lines between the model and observed cross-shore velocity. The different colours of the lines indicate the parameterization of that simulation.

left panels of figure C.2 and C.3 show significantly more scatter compared to the water level (figure C.1). Especially the cross-shore velocity displays a large spread around the 1:1 line. As a result, the fitted lines deviate significantly from the 1:1 line, indicating a structural underestimation of the velocity. In addition, it is noteworthy that there is no significant difference between the different roughness formulations. Furthermore, for each formulation the RMSE is large compared to the magnitude of the cross-shore velocity and the correlation is low (table C.3). The long-shore velocity

C.2. MODEL CALIBRATION AND SENSITIVITY ANALYSIS

also shows a relatively large spread but matches the 1:1 line better than the cross-shore velocity (Figure C.2). As a result, the fitted lines are relatively close to the 1:1 line. Especially, the grid varying Chezy formulation matches the 1:1 line well. It is noteworthy that the grid varying Chezy formulation reproduces the negative velocities close to perfect, but underestimated the positive velocities. As a result, the grid varying Chezy formulation receives the lowest RMSE and highest correlation.

Table C.3.: Table showing the performance of the different roughness formulations

Roughness Formulation	Waterlevel			Longshore velocity			Crossshore velocity		
	RMSE [m]	Slope	R	RMSE [ms ⁻¹]	Slope	R	RMSE [ms ⁻¹]	Slope	R
Man low	0.10	1.132	0.98	0.11	0.682	0.76	0.022	0.335	0.57
Man low	0.08	1.073	0.98	0.10	0.638	0.79	0.022	0.304	0.57
CW low	0.11	1.15	0.98	0.11	0.766	0.76	0.022	0.367	0.55
CW high	0.09	1.113	0.98	0.10	0.716	0.78	0.022	0.345	0.57
C low	0.06	0.997	0.98	0.095	0.846	0.83	0.024	0.346	0.47
C high	0.07	1.027	0.98	0.10	0.879	0.82	0.025	0.361	0.48
C dd grid	0.05	1.027	0.98	0.089	0.925	0.86	0.024	0.358	0.48
C dd cell	0.07	1.01	0.98	0.096	0.835	0.82	0.024	0.349	0.49

The presented results of the FLOW calibration indicate that a grid-dependent Chezy formulation performs best. Furthermore, Brakenhoff et al. (2020) suggested that the largest errors in sediment transport occur by removing the effect of flow on ripple roughness as this directly affects suspended sediment transport. In the formulation with a constant Chezy value, the ripple-related roughness is still used for the calculation of the concentration. Therefore, the grid varying Chezy value is chosen as roughness formulation in this study. To conclude, the water level and long-shore velocity are well simulated by the model while the cross-shore velocity is poorly reproduced (Figure C.4). However, the magnitude of the cross-shore velocity is of the right order and the direction is correct for the majority of the time (C.4)

C.2.2. Wave calibration results

The wave calibration results show that the model set up with only locally generated waves reproduces the measured wave heights and orbital velocity well (all simulations except Swell in figure C.5 & C.6). On the contrary, the simulation with only swell waves imposed on the outer boundary does not reproduce the measured wave heights. As a result, the fitted line of the swell simulation deviates substantially from the 1:1 line and thus the simulation has a high RMSE and low correlation (Table C.4). Furthermore, the differences between the other simulations are small both for the

C.2. MODEL CALIBRATION AND SENSITIVITY ANALYSIS

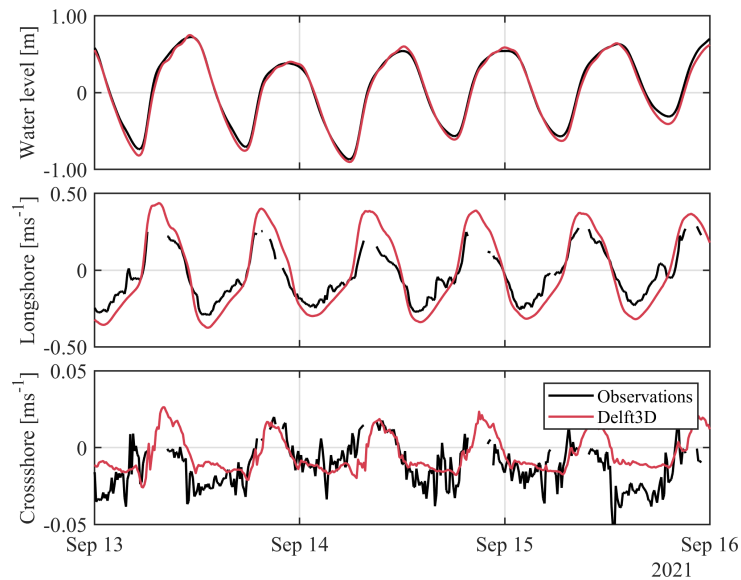


Figure C.4.: The figure shows the fitted lines between the model and observed cross shore velocity. The different colours of the lines indicate the parameterization of that dataset.

wave height and orbital velocity (Figure C.5 & C.6; Table C.4). Therefore, the default parameters of Delft3D will be used in this study in combination with only locally wind-generated waves.

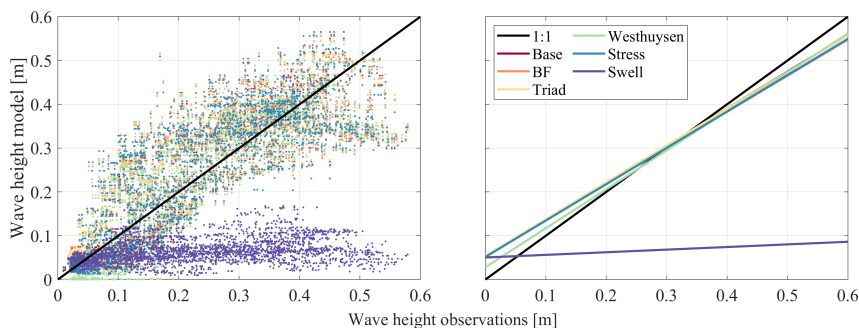


Figure C.5.: The figure shows the fitted lines between the model and observed wave height. The different colours of the lines indicate the parameterization of that simulation.

First of all, the time step is varied between δt is 0.1 s and 0.05 s, where the first δt is the maximum allowed by the Courant-Friedrichs-Lewy condition. In addition, the online coupling time between Delft3D-FLOW and Delft3D-WAVE is varied between 10, 30 and 60 minutes. The difference in wave height and orbital velocity is minimal for the three coupling times used (Table C.5). Furthermore, the simulation with half the time step shows nearly identical results compared to the original simulation. This is not only the case for the wave height and orbital velocity, but cross- and long-shore velocity show a RMSE of 0.003 ms^{-1} .

C.2. MODEL CALIBRATION AND SENSITIVITY ANALYSIS

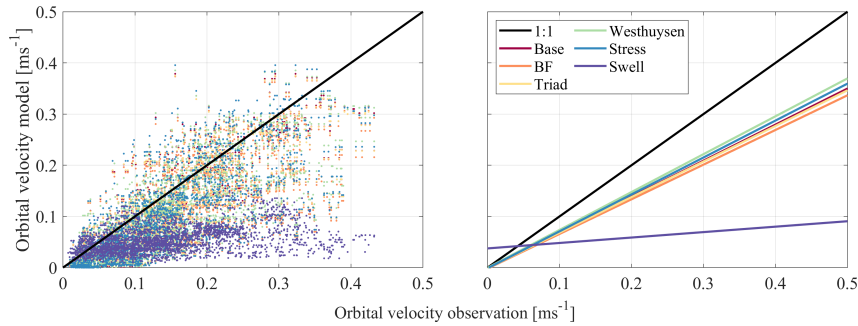


Figure C.6.: The figure shows the fitted lines between the model and observed orbital velocity. The different colours of the lines indicate the parameterization of that simulation.

Table C.4.: Table showing the performance of the Delft3D-WAVE calibration

Simulation	Wave height			Orbital velocity		
	RMSE [m]	Slope	R	RMSE [ms^{-1}]	Slope	R
Base	0.081	0.845	0.841	0.075	0.704	0.763
Bottom friction (0.067)	0.080	0.824	0.837	0.077	0.677	0.763
Triad triad (0n)	0.081	0.839	0.839	0.075	0.695	0.763
Westhuysen white capping	0.079	0.889	0.848	0.069	0.740	0.786
van Rijn stress formulation	0.083	0.830	0.827	0.074	0.722	0.754
Swell waves	0.219	0.060	0.312	0.124	0.106	0.386

Table C.5.: The RMSE of the wave height for the different coupling times and time steps between Delft3D-FLOW and Delft3d-WAVE

Simulations	10 min	30 min	60 min with $\Delta t = 0.1s$	60 min with $\Delta t = 0.05s$
RMSE [cm]	8.28	8.33	8.48	8.57

References

- Ashida, K., & Michiue, M. (1972). Study on hydraulic resistance and bed-load transport rate in alluvial streams. *Japan Society of Civil Engineers*, 206(4), 59–69. https://doi.org/10.2208/jscej1969.1972.206_59
- Bagnold, R. A. (1966). *An approach to the sediment transport problem from general physics*. US government printing office.
- Bird, E. C. (1996). Coastal erosion and rising sea-level. *Sea-level rise and coastal subsidence* (pp. 87–103). Springer.
- Bitan, M., & Zviely, D. (2020). Sand beach nourishment: Experience from the mediterranean coast of israel. *Journal of Marine Science and Engineering*, 8(4), 273.
- Blott, S. J., & Pye, K. (2012). Particle size scales and classification of sediment types based on particle size distributions: Review and recommended procedures. *Sedimentology*, 59(7), 2071–2096.
- Booij, N., Ris, R. C., & Holthuijsen, L. H. (1999). A third-generation wave model for coastal regions: 1. model description and validation. *Journal of geophysical research: Oceans*, 104(C4), 7649–7666.
- Bosboom, J., & Stive, M. J. (2021). Coastal dynamics.
- Brakenhoff, L., Schrijvershof, R., van der Werf, J., Grasmeyer, B., Ruessink, G., & van der Vegt, M. (2020). From ripples to large-scale sand transport: The effects of bedform-related roughness on hydrodynamics and sediment transport patterns in delft3d. *Journal of Marine Science and Engineering*, 8(11). <https://doi.org/10.3390/jmse8110892>
- Brand, E. (2016). *Erosion and transport of sediment and channel-shoal sediment exchange at a shoal in the western dutch wadden sea* (Master's thesis). Utrecht University. Utrecht, Netherlands.
- Brand, E., Ramaekers, G., & Lodder, Q. (2022). Dutch experience with sand nourishments for dynamic coastline conservation—an operational overview. *Ocean & Coastal Management*, 217, 106008.
- Buijsman, M. C., & Ridderinkhof, H. (2007). Water transport at subtidal frequencies in the marsdiep inlet. *Journal of Sea Research*, 58(4), 255–268.
- Carniello, L., D'Alpaos, A., & Defina, A. (2011). Modeling wind waves and tidal flows in shallow micro-tidal basins. *Estuarine, Coastal and Shelf Science*, 92(2), 263–276.
- Carniello, L., Defina, A., & D'Alpaos, L. (2012). Modeling sand-mud transport induced by tidal currents and wind waves in shallow microtidal basins: Application to the venice lagoon (italy). *Estuarine, Coastal and Shelf Science*, 102, 105–115.

-
- Cooke, B. C., Jones, A. R., Goodwin, I. D., & Bishop, M. J. (2012). Nourishment practices on australian sandy beaches: A review. *Journal of environmental management*, *113*, 319–327.
- Cooley, S., Schoeman, D., Bopp, L., Boyd, P., Donner, S., Ghebrehiwet, D., Ito, S.-I., Kiessling, W., Martinette, P., Ojea, E., Racault, M.-F., Rost, B., & Skern-Mauritzen, M. (2022). Ocean and coastal ecosystems and their services. in: Climate change 2022: Impacts, adaptation, and vulnerability. contribution of working group ii to the sixth assessment report of the inter-governmental panel on climate change [h.-o. pörtner, d.c. roberts, m. tignor, e.s. poloczanska, k. mintenbeck, a. alegría, m. craig, s. langsdorf, s. löschke, v. möller, a. okem, b. rama (eds.)] *Cambridge University Press. In Press*. <https://www.ipcc.ch/report/ar6/wg2/>
- Dastgheib, A. (2012). Long-term process-based morphological modeling of large tidal basins.
- Davis Jr, R. A., & Hayes, M. O. (1984). What is a wave-dominated coast? *Developments in sedimentology* (pp. 313–329). Elsevier.
- De Meijer, R., Bosboom, J., Cloin, B., Katopodi, I., Kitou, N., Koomans, R., & Manso, F. (2002). Gradation effects in sediment transport. *Coastal Engineering*, *47*(2), 179–210.
- De Swart, H., & Zimmerman, J. (2009). Morphodynamics of tidal inlet systems. *Annual review of fluid mechanics*, *41*, 203–229.
- Deltares. (2014). 3d/2d modeling suite for integral water solutions: Delft3d hydro-morphodynamics user manual.
- Dey, S. (2014). *Fluvial hydrodynamics* (Vol. 818). Springer.
- Duran-Matute, M., Gerkema, T., & Sassi, M. G. (2016). Quantifying the residual volume transport through a multiple-inlet system in response to wind forcing: The case of the western dutch wadden sea. *Journal of geophysical research: Oceans*, *121*(12), 8888–8903.
- Egiazaroff, I. V. (1965). Effects of wave orbital velocity parameterization on nearshore sediment transport and decadal morphodynamics. *Journal of the Hydraulics Division*, *91*(4), 225–247. <https://doi.org/10.1061/JYCEAJ.0001277>
- Einstein, H. A. (1950). *The bed-load function for sediment transportation in open channel flows*. US Department of Agriculture.
- Elias, E. P., Van der Spek, A. J., Wang, Z. B., & De Ronde, J. (2012). Morphodynamic development and sediment budget of the dutch wadden sea over the last century. *Netherlands Journal of Geosciences*, *91*(3), 293–310.
- Elias, E. P., & van der Spek, A. J. (2017). Dynamic preservation of texel inlet, the netherlands: Understanding the interaction of an ebb-tidal delta with its adjacent coast. *Netherlands Journal of Geosciences*, *96*(4), 293–317.
- Fagherazzi, S., & Wiberg, P. (2009). Importance of wind conditions, fetch, and water levels on wave-generated shear stresses in shallow intertidal basins. *Journal of Geophysical Research: Earth Surface*, *114*(F3).
-

-
- Franz, G., Delpy, M. T., Brito, D., Pinto, L., Leitão, P., & Neves, R. (2017). Modelling of sediment transport and morphological evolution under the combined action of waves and currents. *Ocean Science*, *13*(5), 673–690.
- Fredsøe, J. (1984). Turbulent boundary layer in wave-current motion. *Journal of Hydraulic Engineering*, *110*(8), 1103–1120. [https://doi.org/10.1061/\(ASCE\)0733-9429\(1984\)110:8\(1103](https://doi.org/10.1061/(ASCE)0733-9429(1984)110:8(1103)
- Fredsoe, J., & Deigaard, R. (1992). *Mechanics of coastal sediment transport* (Vol. 3). World scientific publishing company.
- Friedrichs, C. T., & Aubrey, D. G. (1988). Non-linear tidal distortion in shallow well-mixed estuaries: A synthesis. *Estuarine, Coastal and Shelf Science*, *27*(5), 521–545.
- Garvine, R. W. (1985). A simple model of estuarine subtidal fluctuations forced by local and remote wind stress. *Journal of Geophysical Research: Oceans*, *90*(C6), 11945–11948.
- Gittman, R. K., Popowich, A. M., Bruno, J. F., & Peterson, C. H. (2014). Marshes with and without sills protect estuarine shorelines from erosion better than bulkheads during a category 1 hurricane. *Ocean & Coastal Management*, *102*, 94–102.
- Grant, W. D., & Madsen, O. S. (1979). Combined wave and current interaction with a rough bottom. *Journal of Geophysical Research: Oceans*, *84*(C4), 1797–1808.
- Groen, P. (1967). On the residual transport of suspended matter by an alternating tidal current. *Netherlands Journal of Sea Research*, *3*(4), 564–574.
- Hanson, H., Brampton, A., Capobianco, M., Dette, H. H., Hamm, L., Laustrup, C., Lechuga, A., & Spanhoff, R. (2002). Beach nourishment projects, practices, and objectives—a european overview. *Coastal engineering*, *47*(2), 81–111.
- Herrling, G., & Winter, C. (2014). Morphological and sedimentological response of a mixed-energy barrier island tidal inlet to storm and fair-weather conditions. *Earth Surface Dynamics*, *2*(1), 363–382.
- Hoefel, F., & Elgar, S. (2003). Wave-induced sediment transport and sandbar migration. *Science*, *299*(5614), 1885–1887.
- Holland, K., & Elmore, P. (2008). A review of heterogeneous sediments in coastal environments. *Earth-Science Reviews*, *89*(3-4), 116–134.
- Holthuijsen, L. H. (2010). *Waves in oceanic and coastal waters*. Cambridge university press.
- Hottovy, J. D., & Sylvester, N. D. (1979). Drag coefficients for irregularly shaped particles. *Industrial & Engineering Chemistry Process Design and Development*, *18*(3), 433–436.
- Huisman, B. J. A., Ruessink, B. G., De Schipper, M. A., Luijendijk, A. P., & Stive, M. J. F. (2018). Modelling of bed sediment composition changes at the lower shoreface of the sand motor. *Coastal Engineering*, *132*, 33–49. <https://doi.org/10.1016/j.coastaleng.2017.11.007>
-

-
- Huisman, B., De Schipper, M., & Ruessink, B. (2016). Sediment sorting at the sand motor at storm and annual time scales. *Marine Geology*, *381*, 209–226.
- Iglesias, I., Avilez-Valente, P., Bio, A., & Bastos, L. (2019). Modelling the main hydrodynamic patterns in shallow water estuaries: The minho case study. *Water*, *11*(5), 1040.
- Inman, D. L. (1949). Sorting of sediments in the light of fluid mechanics. *Journal of Sedimentary Research*, *19*(2), 51–70.
- Jain, R., Tschisgale, S., & Froehlich, J. (2020). Effect of particle shape on bedload sediment transport in case of small particle loading. *Meccanica*, *55*(2), 299–315.
- Kleinhans, M. G., & van Rijn, L. C. (2002). Stochastic prediction of sediment transport in sand-gravel bed rivers. *Journal of hydraulic engineering*, *128*(4), 412–425.
- klein Obbink, M. (2022). *Multi-fraction sediment sorting and entrainment at the prins hendrikzand-dijk* (Master's thesis). Utrecht University. Utrecht, Netherlands.
- Komar, P. D. (1987). Selective grain entrainment by a current from a bed of mixed sizes; a reanalysis. *Journal of Sedimentary Research*, *57*(2), 203–211.
- Komen, G. J., Hasselmann, S., & Hasselmann, K. (1984). On the existence of a fully developed wind-sea spectrum. *Journal of physical oceanography*, *14*(8), 1271–1285. [https://doi.org/10.1175/1520-0485\(1984\)014<1271:OTEOAF>2.0.CO;2](https://doi.org/10.1175/1520-0485(1984)014<1271:OTEOAF>2.0.CO;2)
- Lenstra, K. J., Pluis, S. R., Ridderinkhof, W., Ruessink, G., & van der Vegt, M. (2019). Cyclic channel-shoal dynamics at the ameland inlet: The impact on waves, tides, and sediment transport. *Ocean Dynamics*, *69*(4), 409–425.
- Lesser, G. R., Roelvink, J. A., van Kester, J. A. T. M., & Stelling, G. S. (2004). Development and validation of a three-dimensional morphological model. *Coastal Engineering*, *51*(8-9), 883–915. <https://doi.org/10.1016/j.coastaleng.2004.07.014>
- Longuet-Higgins, M. S., & Stewart, R. (1964). Radiation stresses in water waves; a physical discussion, with applications. *Deep sea research and oceanographic abstracts*, *11*(4), 529–562.
- Morris, R. L., Konlechner, T. M., Ghisalberti, M., & Swearer, S. E. (2018). From grey to green: Efficacy of eco-engineering solutions for nature-based coastal defence. *Global Change Biology*, *24*(5), 1827–1842. <https://doi.org/https://doi.org/10.1111/gcb.14063>
- Mulder, H. P., & Udink, C. (1991). Modelling of cohesive sediment transport. a case study: The western scheldt estuary. *Coastal engineering 1990* (pp. 3012–3023).
- Parker, G., Klingeman, P. C., & McLean, D. G. (1982). Bedload and size distribution in paved gravel-bed streams. *Journal of hydraulics Division*, *108*(4), 544–571. <https://doi.org/10.1061/JYCEAJ.0005854>
-

-
- Pawlowicz, R., Beardsley, B., & Lentz, S. (2002). Classical tidal harmonic analysis including error estimates in matlab using *t_{tide}*. *Computers & Geosciences*, 28(8), 929–937. [https://doi.org/10.1016/S0098-3004\(02\)00013-4](https://doi.org/10.1016/S0098-3004(02)00013-4)
- Perk, L., van Rijn, L. C., Koudstaal, K., & Fordeyn, J. (2019). A rational method for the design of sand dike/dune systems at sheltered sites; wadden sea coast of texel, the netherlands. *Journal of Marine Science and Engineering*, 7(9), 324.
- Ribberink, J. S. (1987). *Mathematical modelling of one-dimensional morphological changes in rivers with non-uniform sediment* (Doctoral dissertation). Delft University.
- Ribberink, J. S., & Al-Salem, A. A. (1994). Sediment transport in oscillatory boundary layers in cases of rippled beds and sheet flow. *Journal of Geophysical Research: Oceans*, 99(C6), 12707–12727.
- Ridderinkhof, H. (1988). Tidal and residual flows in the western dutch wadden sea i: Numerical model results. *Netherlands Journal of Sea Research*, 22(1), 1–21.
- Rouse, H. (1950). *Engineering hydraulics; proceedings of the fourth hydraulic conference. iowa institute of hydraulic research, jun 12-15, 1949* (tech. rep.).
- Ruessink, B., Ramaekers, G., & Van Rijn, L. (2012). On the parameterization of the free-stream non-linear wave orbital motion in nearshore morphodynamic models. *Coastal engineering*, 65, 56–63.
- RWS-WVL, & Deltares. (2017). *Modelbeschrijving dutch continental shelf model (dcsmv6) & dutch continental shelf - zuidelijk noordzee model (dcsmv6-zunov4)*. Retrieved April 19, 2022, from https://www.helpdeskwater.nl/publish/pages/132741/factsheet-dcsm_zunogeneratie_5_v2017_01.pdf
- Santoro, P., Fossati, M., Tassi, P., Huybrechts, N., Van Bang, D. P., & Piedra-Cueva, J. I. (2017). A coupled wave–current–sediment transport model for an estuarine system: Application to the rio de la plata and montevideo bay. *Applied Mathematical Modelling*, 52, 107–130.
- Shields, A. (1936). Application of similarity principles and turbulence research to bed-load movement.
- Sloff, K., & Mosselman, E. (2012). Bifurcation modelling in a meandering gravel–sand bed river. *Earth Surface Processes and Landforms*, 37(14), 1556–1566. <https://doi.org/10.1002/esp.3305>
- Sorourian, S., Huang, H., Li, C., Justic, D., & Payandeh, A. R. (2020). Wave dynamics near barataria bay tidal inlets during spring–summer time. *Ocean Modelling*, 147, 101553.
- Soulsby, R. L., Hamm, L., Klopman, G., Myrhaug, D., Simons, R., & Thomas, G. (1993). Wave-current interaction within and outside the bottom boundary layer. *Coastal engineering*, 21(1-3), 41–69.
-

-
- Stanev, E. V., Wolff, J.-O., Burchard, H., Bolding, K., & Flöser, G. (2003). On the circulation in the east frisian wadden sea: Numerical modeling and data analysis. *Ocean Dynamics*, 53(1), 27–51.
- Steetzel, H., van der Goot, F., Fiselier, J., de Lange, M., Penning, E., van Santen, R., & Vuik, V. (2017). Building with nature pilot sandy foreshore houtribdijk design and behaviour of a sandy dike defence in a lake system. *Coastal Dynamics: Port of Spain, Trinidad and Tobago*.
- Stive, M. J., De Schipper, M. A., Lujendijk, A. P., Aarninkhof, S. G., van Gelder-Maas, C., Van Thiel de Vries, J. S., De Vries, S., Henriquez, M., Marx, S., & Ranasinghe, R. (2013). A new alternative to saving our beaches from sea-level rise: The sand engine. *Journal of Coastal Research*, 29(5), 1001–1008.
- Swart, D. H. (1974). Offshore sediment transport and equilibrium beach profiles.
- Travers, A., Eliot, M., Eliot, I., & Jendzejczak, M. (2010). Sheltered sandy beaches of southwestern australia. *Geological Society, London, Special Publications*, 346(1), 23–42.
- Van de Kreeke, J., & Robaczewska, K. (1993). Tide-induced residual transport of coarse sediment; application to the ems estuary. *Netherlands Journal of Sea Research*, 31(3), 209–220.
- van der Westhuysen, A. J., Zijlema, M., & Battjes, J. A. (2007). Nonlinear saturation-based whitecapping dissipation in swan for deep and shallow water. *Coastal Engineering*, 54(2), 151–170. <https://doi.org/10.1016/j.coastaleng.2006.08.006>
- van der Wegen, M., Dastgheib, A., Jaffe, B., & Roelvink, D. (2011). Bed composition generation for morphodynamic modeling: Case study of san pablo bay in california, usa. *Ocean Dynamics*, 61, 173–186. <https://doi.org/10.1007/s10236-010-0314-2>
- Van Rijn, L. C. (1997). *Cross-shore modelling of graded sediments*. (tech. rep. Z2181). WL | Delft Hydraulics.
- Van Rijn, L. C. (2007a). Unified view of sediment transport by currents and waves. i: Initiation of motion, bed roughness, and bed-load transport. *Journal of Hydraulic engineering*, 133(6), 649–667. [https://doi.org/10.1061/\(ASCE\)0733-9429\(2007\)133:6\(649\)](https://doi.org/10.1061/(ASCE)0733-9429(2007)133:6(649))
- Van Rijn, L. C. (2007b). Unified view of sediment transport by currents and waves. iii: Graded beds. *Journal of Hydraulic engineering*, 133(6), 761–775. [https://doi.org/10.1061/\(ASCE\)0733-9429\(2007\)133:7\(761\)](https://doi.org/10.1061/(ASCE)0733-9429(2007)133:7(761))
- Van Rijn, L., Walstra, D., & Ormondt, M. v. (2004). Description of transpor2004 and implementation in delft3d-online. Z3748.
- Van Rijn, L. C. et al. (1993). *Principles of sediment transport in rivers, estuaries and coastal seas* (Vol. 1006). Aqua publications Amsterdam.
- Wiberg, P. L., Drake, D. E., & Cacchione, D. A. (1994). Sediment resuspension and bed armor-ing during high bottom stress events on the northern california inner continental shelf: Measurements and predictions. *Continental Shelf Research*, 14(10-11), 1191–1219.
-

-
- Winkelmolen, A. M. (1971). Rollability, a functional shape property of sand grains. *Journal of Sedimentary Research*, 41(3), 703–714.
- Witteveen+Bos. (2011). *Planstudie dijkversterking waddenzeedijk texel zandige oplossing prins hendrikpolder* (tech. rep.).
- Woerdman, J. B. (2022). *Alongshore variability in hydrodynamics and its implications for sand transport in front of the prins hendrik sanddike* (Master's thesis). Utrecht University. Utrecht, Netherlands.
- Wu, J. (1982). Wind-stress coefficients over sea surface from breeze to hurricane. *Journal of Geophysical Research: Oceans*, 87(c12), 9704–9706. <https://doi.org/10.1029/JC087iC12p09704>
- Zhu, Q., Yang, S., & Ma, Y. (2014). Intra-tidal sedimentary processes associated with combined wave–current action on an exposed, erosional mudflat, southeastern yangtze river delta, china. *Marine Geology*, 347, 95–106.
- Zijlema, M., Van Vledder, G. P., & Holthuijsen, L. H. (2012). Bottom friction and wind drag for wave models. *Coastal Engineering*, 65, 19–26. <https://doi.org/10.1016/j.coastaleng.2012.03.002>
- Zijlema, M. (2009). Multiscale simulations using unstructured mesh swan model for wave hind-casting in the dutch wadden sea. *Proceedings of coastal dynamics 2009: Impacts of human activities on dynamic coastal processes (with cd-rom)* (pp. 1–12). World Scientific.
- Zimmerman, J. T. F. (1976). Mixing and flushing of tidal embayments in the western dutch wadden sea part i: Distribution of salinity and calculation of mixing time scales. *Netherlands Journal of Sea Research*, 10(2), 149–191.